Alma Mater Studiorum
Università degli Studi di Bologna

Facoltá di Scienze Matematiche, Fisiche e Naturali

Dipartimento di Astronomia

DOTTORATO DI RICERCA IN ASTRONOMIA

Ciclo XXIII

TOWARDS AN ALL-SKY CONTINUUM SURVEY WITH A NEW K-BAND MULTI-FEED RECEIVER

System Characterization, Calibration, Software Development & Pilot Survey

Dottoranda:

RASHMI VERMA

Coordinatore:
Prof. Lauro Moscardini

Relatore:
Prof. Loretta Gregorini

Co-relatori:
Dr. **Isabella Prandoni**
Ing. **Alessandro Orfei**

Settore Scientifico Disciplinare: Area 02 - Scienze Fisiche

FIS/05 Astronomia e Astrofisica

Esame Finale Anno 2011

Abstract

This thesis has been carried out in the framework of the EU FP6 Marie Curie Early Stage Training programme 'ESTRELA'.

In this thesis, the design and the commissioning of the K-band 7-horn multi-feed receiver (MF) on the Medicina 32-m telescope is described. The MF receiver currently undergoing commissioning on Medicina telescope, has been designed and built for the upcoming Sardinia Radio Telescope. The MF receiver, based on the heterodyne receiver technology, is a 7-horn focal plane array arranged in a hexagonal geometry with a central feed and operates in the frequency band 18-26.5 GHz with an instantaneous bandwidth of 2 GHz. A total power analogue backend (2 GHz bandwidth, 7×2 channels) was designed and built for continuum observations with the MF.

This thesis presents several sets of measurements performed as part of the MF receiver commissioning to test the receiver performance on the Medicina antenna. The optical alignment of the MF receiver attached to the Medicina antenna was optimized to gain the maximum power in the main lobe of the antenna beam, at the same time minimizing the sidelobes. The system temperature together with other antenna parameters were measured and found to be in agreement with the expected values.

In parallel I calculated precise values for the MF T_{cal} as a function of frequency in the entire 18-26.5 GHz operational range. A mathematical approach was developed to achieve this goal using T_{cal} laboratory measurements as reference values.

A dedicated calibration campaign was carried out to assess the pointing precision

of the MF receiver coupled with the total power analogue backend on the Medicina antenna and to obtain a list of suitable pointing and flux calibrators for 21 GHz observations. The pointing of the MF receiver was found to be within the pointing accuracy of the Medicina telescope (1/10 of the antenna beamsize) and is not affected by antenna speed. The pointing of the receiver was found to be stable for weak sources as well ($\approx$ 1 Jy). A method was developed to calibrate the MF receiver in absence of a noise source. A list of pointing and flux calibrators was obtained both for Medicina and SRT telescopes.

A pilot survey at 21 GHz was conducted as part of the commissioning and in the framework of an international collaboration aimed to map the entire Northern sky in K-band. An area of 1000 square degrees covering the Northern polar cap was mapped using the On The Fly fast scanning observing strategy. A list of 151 source candidates was obtained from the pilot survey maps.

Follow-up observations of a subsample of 104 'reliable' sources candidates extracted from the candidate list were performed at 30 GHz in the framework of the 'ESTRELA' collaboration at the Toruń telescope. 57 sources were confirmed and the flux densities of these sources are presented in Chapter 5.

Follow-up observations at 5, 8 and 21 GHz have been carried out at Medicina. Preliminary results indicate 70 sources are confirmed as real at 21 and 5 GHz, and 66 of them were also detected at 8 GHz. All the sources detected at 30 GHz were also detected at 21 GHz. The results presented in this thesis prove the MF receiver scientific capabilities and address its high sensitivity.

This thesis was submitted by Rashmi Verma, to the University of Bologna, Italy for the degree of Doctoral of Philosophy in Dipartimento di Astronomia on 15^{th} March 2011.

This thesis work was carried out at INAF - Istituto di Radioastronomia (Bologna, Italy) by extensively using the Medicina 32-m dish.

Acknowledgments

This research was supported by the EU Framework 6 Marie Curie Early Stage Training programme under contract number MEST-CT-2005-19669 'ESTRELA'. I would like to thank Jodrell Bank Centre for Astrophysics, University of Manchester UK, for hosting me for three months 2010. My sincere thanks to INAF-Istituto di Radioastronomia, Bologna for offering me 'Assegno di Ricerca' immediately after my 'ESTRELA' fellowship came to an end.

It brings me great pleasure to thank many people who have made this thesis possible. This thesis would not have been possible without the kind support and encouragement of my Ph.D supervisors Isabella Prandoni and Loretta Gregorini. I am grateful to both for their continuous support, their enthusiastic involvement in the project and their detailed and constructive comments.

I owe my deepest gratitude to Dr. D. Anish Roshi my mentor, who gave me an opportunity to work with him at Raman Research Institute, Bangalore, India and introduced me to the field of radio astronomy.

At Istituto di Radioastronomia, I am grateful to Alessandro Orfei for our long discussions on radio antenna and receiver technology and also to Hans de Ruiter and Paola Parma to help me dealing with Italian bureaucracy. I would like to thank Franco Mantovani for his support and discussion on single dish calibration techniques. My warm thanks to Roberto Ricci and Giulia Macario for fruitful discussions and continuous moral support.

I extend my thanks to all the engineers, technicians and all other members at Medicina, especially Marco Schiaffino, Giovanni Naldi, Andrea Maccaferri, Giuseppe Maccaferri, Sergio Mariotti, Andrea Orlati and Emma Salerno, who have been very supportive and encouraging during my frequent visits to Medicina.

I would also like to acknowledge all the members of OCRA collaboration at the University of Manchester and the Toruń Radio Astronomy Observatory.

I am deeply indebted to my beloved family, my parents Sushil Kumar Verma and Nirmala Verma to whom I dedicate this thesis, my brothers Pankaj Kumar Verma and Amit Kumar Verma for their unconditional love, support and moral guidance at all the times. I extend my warm thanks to all my friends all over the world. Last but not the least I would like to convey my sincere thanks to all those who supported me in any respect during the completion of the project.

Thesis Outline

This thesis is organized in six chapters listed as follows:

- The first chapter provides a brief overview of the traditional single-feed receivers and of focal plane arrays with a discussion of the two possible architectures of focal plane arrays (multi-feeds and phased arrays).
- Chapter 2 gives a description of the new K-band multi-feed receiver designed for the Sardinia Radio Telescope, of the total power analogue backend attached to it and of the Medicina 32-m dish. It illustrates the tests performed to obtain the best optical alignment for the MF receiver. Then it summarizes the several sets of measurements carried out in 2008 during the first commissioning phase of the MF receiver, using the VLBI backend (Mark 4).
- Chapter 3 describes the method developed to obtain precise values of T_{cal} as a function of frequency in the 18-26.5 GHz bandwidth of the MF receiver.
- Chapter 4 describes the dedicated calibration campaign carried out in 2009 at 21 GHz with the MF receiver coupled with the total power analogue backend to check the pointing accuracy of the receiver and to develop a flux calibration methodology to calibrate MF data in absence of a noise source implemented in the Medicina acquisition software.
- Chapter 5 describes the pilot survey performed at 21 GHz as part of the commissioning, to check the scientific capabilities of the MF receiver. It describes the pilot survey observing strategy, pointing and flux calibration, map-making and source extraction. Preliminary results of the pilot survey and of the follow-up multifrequency observations are reported.
- Chapter 6 concludes the thesis with a summary of the results and a brief overview of ongoing and future work.

- A series of Appendices (A to F) report the many plots resulting from the work described in the thesis chapters.

Contents

List of Tables

Conventions

- AX_0 , AY_0, $AZ1_0$, $AZ2_0$, and $AZ3_0$ - The position of X, Y, Z1, Z2 and Z3 actuators in mm at an elevation of 45° where the subreflector is aligned with the primary reflector.
- AX , AY, AZ1, AZ2, and AZ3 - The amount of displacement with respect to the primary reflector to get the final position parameters of the subreflector x, y , z , θ_x and θ_y.
- Ag - Geometric area.
- Count - The radio signal in an arbitrary backend unit.
- d_{sky} - Sky distance between the horns of multi-feed.
- dn - Number of measurements in each bin.
- Dec - Declination.
- Delta Dec - Difference between the actual declination of the source (taken from the literature) and the one obtained after the gaussian fitting to the scans.
- Delta RA - Difference between the actual right ascension of the source (taken from the literature) and the one obtained after the gaussian fitting to the scans in right ascension.
- El - Elevation.
- f - Focal length of cassegrain focus.
- FWHM - Full width at half maximum.
- FWHM (RA) - Full width at half maximum of antenna beam in right ascension direction.

- FWHM (Dec) - Full width at half maximum of antenna beam in declination direction.
- LCP - Left circular polarization.
- RA - Right ascension.
- RCP - Right circular polarization.
- SNR - Signal to noise ratio.
- τ - Atmospheric opacity.
- θ_x and θ_y - Angle of tilt about X-axis and Y-axis respectively.
- x - y - Azimuth and elevation axis respectively.
- UT - Universal time.
- z - focus axis of the telescope.
- ZA - Zenith angle.

Chapter 1

Introduction

A new era started in astronomy in 1930, when Karl Jansky detected the radio emission from the Galaxy and opened a new window to study the Universe. Until then our knowledge was limited to the optical regime of the electromagnetic spectrum. Another milestone was reached when Grote Reber designed and built the first radio telescope dedicated to radio astronomical observations and conducted a systematic survey at 160 MHz (Reber, 1944). He not only confirmed the discovery made by Karl Jansky but also discovered discrete sources of radio emission in our galaxy, Cygnus, and Cassiopeia. Since then many radio surveys have been conducted and advanced our knowledge of the radio sky.

1.1 Radio Astronomy

Radio astronomy provides a uniquely broad window in the electromagnetic spectrum. It spans roughly 5 decades of frequency with a lower cutoff at 10 MHz due to the ionosphere, and an upper end at 1 THz, due to the absorption of radio waves by H_2O and O_2 molecules present in the troposphere. The radio signals are generally very weak and require a large amount of collecting area and highly sensitive receivers to be detected. The quest for higher resolution and higher sensitivity pushed the radio astronomical community to built larger telescopes and wider bandwidth receivers.

1.1.1 The radio antenna

A variety of radio antennas exists all over the world to satisfy the special requirements of radio astronomy: from parabolic antennas (like eg. the Medicina,

the Green Bank and the Efflesberg telescopes), to cylindrical antennas (like the Northern Cross); from dipole antennas to helical antennas, etc. Among these, parabolic antennas are extensively used for astronomical observations. A parabolic antenna consists of a parabolic reflector which collects and concentrates incoming parallel radio waves at the focus where the antenna feed is placed. The field of view (or antenna beam) of a parabolic antenna depends on the physical extent of the primary reflector (mirror). For a uniform illumination it can be given by:

$$\theta_{ant} = 1.22\frac{\lambda}{D} \tag{1.1}$$

where D is the diameter of the primary reflector and λ is the wavelength of the incident radiation. This also corresponds to the angular resolution of the antenna.

1.1.2 Receivers

Radio Telescopes are equipped with a large variety of feeds and receivers optimized for various scientific purposes. At centimeter wavelengths coherent detection (heterodyne receivers) techniques are mostly used. Figure 1.1 shows a simplified block diagram of the basic heterodyne receiver, where a radio signal is amplified, down-converted and filtered prior to detection. In such a system the signal power is first amplified in a radio-frequency (RF) amplifier. In the next step this weak signal is mixed with a strong local-oscillator signal bringing it to an intermediate frequency (IF), then it is again amplified using an amplifier of larger gain (60 to 90 dB). The IF amplifier is followed by a detector (mostly a square law detector) and by the post detection electronics.

The minimum detectable temperature ΔT for a coherent system can be calculated using the radiometer equation:

$$\Delta T = \frac{kT_{sys}}{\sqrt{Bt}} \tag{1.2}$$

where k is a sensitivity constant, which depends on the type of receiver. T_{sys} is the total system temperature of the receiver, B and t are the bandwidth and integration time respectively.

Currently the speed at which an astronomical source larger than the angular size of the antenna beam can be mapped, is limited by the traditional single pixel receiver technology. The time required to map a large area in the sky can be substantially

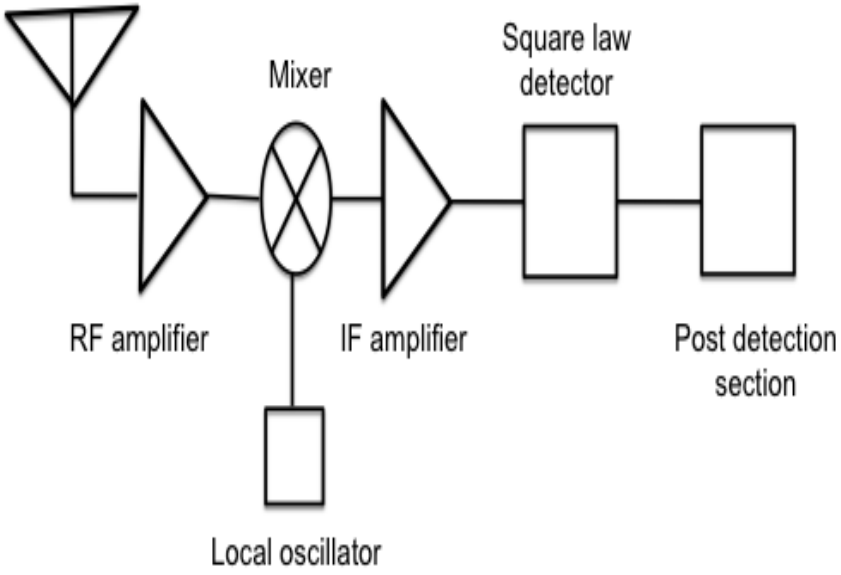

Figure 1.1: A block diagram of the basic heterodyne receiver. The first component is the RF amplifier which amplifies the signal with a gain of 10-30 dB. The signal is then combined with the local oscillator frequency (ν_0) and then amplified by IF amplifier with a gain of 60-90 dB. The signal is finally detected by a square law detector and sent to the post detection section (integrator and data recording)

reduced by using multiple detectors in the focal plane of the telescope, each with a distinct beam on the sky.

1.2 Need for Focal Plane Arrays

The development of radio-receiver technology and the use of large antennas enables us to carry out high sensitivity surveys. But as the observing frequency increases, the time required for carrying out a large-scale high sensitivity survey increases significantly due to smaller antenna beam size. This typically results in smaller and/or lower sensitivity surveys going from lower to higher observing frequencies, as clearly shown in Table 1.1.

A potential solution to increase the surveying speed consists in creating a radio camera at the focal plane of the telescope that allows to increase the field of view of

Table 1.1: A list of the major large-area continuum radio surveys carried out at frequencies $\geq$ 1.4 GHz.

Survey	Frequency (GHz)	Resolution	Coverage/Area	Flux density limit (mJy)	Reference
FIRST	1.4	$5''$	9,900 deg^2 of Northern Galactic cap	1	Becker et al. 1995
NVSS	1.4	$45''$	$Dec > -40°$	2.5	Condon et.al. (1998)
PKS	2.7	$8'$	$Dec < 27°$	50	Bolton et al. (1979)
GB6	5.0	$3'$	$0° < Dec < 75°$	18	Gregory et al. (1996)
PMN	5.0	$5'$	$-87.5° < Dec < 10°$	35	Griffith et al. (1993)
AT20G	20.0	$2.3'$	$-90° < Dec < 0°$	50	Hancock et al. (2011)
WMAP	23, 33, 41, 61, 94	0.88°, 0.66°, 0.51°, 0.35°, 0.22°	All sky	1000	Jarosik et al. (2011)
Planck	30, 44, 70	$32'$, $27'$,$13'$	All sky	500-600	(*)

(*)Explanatory Supplement to the Planck Early Release Compact Source Catalogue, 2011

the antenna. Some of the main scientific drivers to explore and develop focal plane arrays are: high-frequency continuum mapping of extended sources, interpretation of high sensitivity and high resolution CMB maps, spectroscopic molecular studies of large star forming regions and galaxies.

Furthermore blind surveys of large areas of sky at high frequency are the way to study the composition and the properties of the high frequency radio population: for instance flat-spectrum radio sources, like Flat-Spectrum Radio Quasars, BLLacs or High-Frequency Peakers, which are hidden among standard steep spectrum sources at lower frequencies. The latter are of particular interest as they are supposed to mark the earliest phase of radio galaxy evolution.

1.3 Focal Plane Arrays

There are two possible feed architectures for focal plane arrays. One is the cluster of conventional horns (multi-feeds) and the second one is phased arrays.

1.3.1 Multi-feeds

This type of focal plane array is achieved by placing an array of conventional feeds in the focal plane of the telescope forming a radio camera. Each feed in

this system receives the radiation from a particular direction with respect to the antenna bore-sight. This receiver technology is well understood and optimized to provide excellent performance; but due to the physical separation between the horns, the corresponding focal points are separated by certain projected distance in the sky. As a result the overall field of view of the multi-feed is typically undersampled. An example of focal plane array with cluster of horns is shown in Figure 1.2a. This system is the K-band multi-feed receiver (MF) with 7 elements in an hexagonal geometry designed for the new Sardinia Radio Telescope (SRT) and currently mounted at Medicina telescope (see Chapter 2). A list of various focal plane arrays based on cluster of horns currently existing (or undergoing commissioning) all around the world is provided in Table 1.2. It is worth mentioning that the MF receiver shares its uniqueness with the newly built GBT 7-horn multi-feed receiver which is coming online. The GBT multi-feed receiver is optimized for spectroscopic studies while the SRT multi-feed receiver is a multi-purpose receiver. Currently it is equipped with a total power backend but a spectrometer is under construction.

1.3.2 Phased arrays

Phased arrays sample the field near the focal plane with an array of densely-packed wide-band antennas (such as Vivaldi antennas) and add the outputs of several receivers together with complex weights to synthesize beams on the sky. The focal-plane arrays based on phased-array techniques are currently under development (an example is shown in Figure 1.2b). The major advantage of this approach is that the field of view is completely sampled. On the other hand a disadvantage could be that the receiver may be too bulky to be cooled, resulting in a high system temperature.

(a) A photograph of the K-band multi-feed receiver (cluster of horns) designed for the new Sardinia Radio Telescope. The receiver spans a frequency range of 18-26.5 GHz. Photograph courtesy, Istituto di Radioastronomia-INAF, Italy.

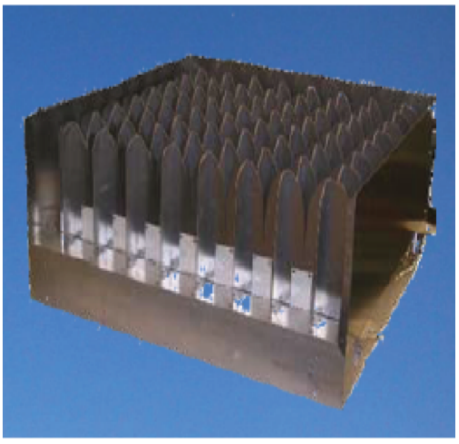

(b) A photograph of the focal plane phased array, Apertif. The receiver stretches a frequency band from 1.0 to 1.7 GHz. Photograph courtesy, ASTRON, Netherlands.

Figure 1.2: Focal plane arrays.

Table 1.2: A comparision of the characteristic parameters of the various focal plane arrays (coherent receivers only); col.(1) gives the name and diameter of the antenna in units of meter; col.(2) gives the central operational frequency of the receiver; col.(3) and col.(4) give the number of elements in the multi-feed and the geometry they are arranged; col.(5) and col.(6) give the beam separation projected in the sky (arcsec) and the FHWM beamsize (arcsec) for each feed.

Antenna	Frequency (GHz)	Elements	Geometry	Distance″	FWHM″
Parkes 64 m	1.5	13	2 concentric hexagons + central	28×60	14.0×60
Efflesberg 100 m	1.5	7	Hexagon + central	15×60	9.6×60
Arecibo 305 m	1.5	7	Hexagon + central	26 cm	198
Medicina 32 m *	22	7	Hexagon + central	212	96
GBT 100 m *	22	7	Hexagon + central	92	32
Toruń 32 m *	30	8	4×4	180	72
Efflesberg 100 m *	32	7	Hexagon + central		24
Nobeyama 45 m	43	6	2×3	80	40
Nobeyama 45 m	100	25	5×5	40	17
Pico Veleta 30 m	230	9	3×3	24	9

* The system is currently in the process of commissioning.

Chapter 2

K-band MF Receiver: System Characterization at Medicina 32-m dish

In this chapter I will give an overview of the MF receiver and will describe the system characterization of the MF receiver on the Medicina 32-m dish. In Section 2.1 and Section 2.2 I will describe the design of the MF receiver and the total power analogue backend respectively. Section 2.3 will give a brief overview of the Medicina telescope. The antenna parameters and the laboratory measurements will be discussed in Section 2.4 and Section 2.5 respectively. Section 2.6 will focus on the pointing calibration of the receiver and the results of the system characterization will be discussed in Section 2.7.

2.1 K-band MF Receiver

The Istituto di Radioastronomia (INAF, Bologna) in collaboration with the Osservatorio Astrofisico di Arcetri (INAF, Firenze) has recently built a 7-horn K-band multi-feed (MF) receiver for the upcoming Sardinia Radio Telescope (SRT). It was designed and constructed as part of the EC-funded "Focal plane Array for Radio Astronomy Design Access & Yield" (FARADAY) project within the RadioNet consortium. The design of the receiver (see Figure 2.1) is based on the traditional heterodyne receiver technology.

The main scientific interests behind this project are the study of the high frequency radio populations like flat-spectrum QSO, GPS (Gigahertz Peaked

Spectrum sources) and HFP (High Frequency Peakers), the characterization of foreground sources for a better interpretation of the Cosmic Microwave Background (CMB) maps, etc.

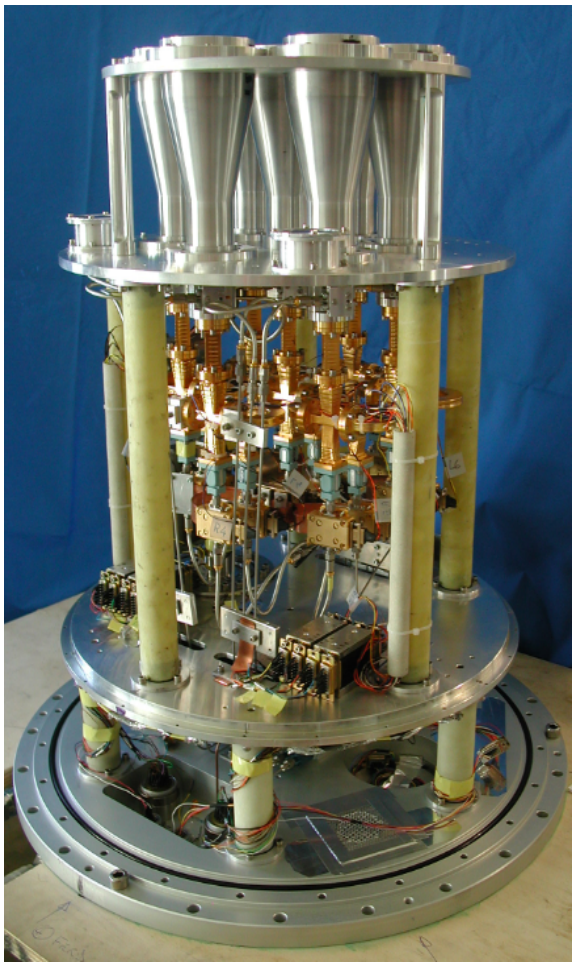

Figure 2.1: K-band MF receiver in the laboratory for test measurements.

The new K-band MF receiver is a 7-horn heterodyne focal plane array arranged in a hexagonal geometry with a central feed. It consists of 7-corrugated feeds working in the frequency band 18-26.5 GHz. It provides 14 output channels (7 LCP & 7 RCP) with an instantaneous bandwidth of 2 GHz for each channel. For commissioning purposes the MF receiver was mounted on the Medicina 32-m dish. The top view of the K-band MF receiver mounted in the central bay of the cassegrain focus of the Medicina 32-m dish (along with other two receivers) is shown in Figure 2.2a. Figure 2.2b shows the position of the seven feeds placed in the focal plane of the Medicina dish. While mounting the MF receiver on Medicina dish the axis of the alignment of the MF receiver was offset by an amount of 5°, but this offset is taken

into account automatically when commanding or recording the de-rotator position. The characteristic parameters of the MF receiver are listed in Table 2.1.

Table 2.1: Characteristic parameters of the K-band MF receiver

Inner Diameter of the feed	68.8 (mm)
Outer Diameter of the feed	98.0 (mm)
Distance between two adjacent feeds	100.0 (mm)
Output channels	14 (7 LCP + 7 RCP with 2 GHz-wide IF bands)

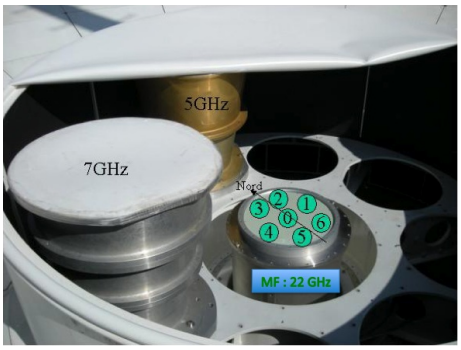

(a) Top view of MF receiver (feeds numbered) installed in the central bay of the cassegrain focus of Medicina 32-m dish.

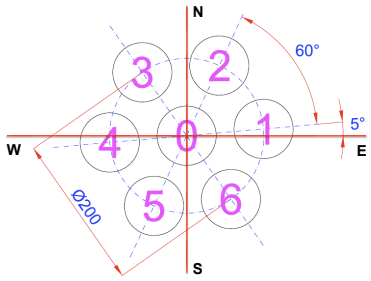

(b) Feed positions on the focal plane of Medicina 32-m dish by looking at the top of the receiver.

Figure 2.2: Top view of the MF receiver.

The feeds are installed inside a dewar which is kept at a temperature of 20 K using liquid nitrogen. The cryogenic and non-cryogenic parts of the receiver are shown in Figure 2.3. As both Medicina telescope and SRT are alt-azimuth mount telescopes, the dewar is also equipped with a mechanical de-rotator in order to compensate for the rotation of the field of view for prolonged measurements. The de-rotator parameters for both Medicina and SRT telescopes are listed in Table 2.2. The final installation of the MF receiver in the cassegrain focus of Medicina 32-m dish with the de-rotator is shown in Figure 2.4.

Table 2.2: De-rotator parameters for Medicina and SRT telescopes

Parameter	Medicina (32-m dish)	SRT (64-m dish)
Rotation range [°]	±130	± 120
Maximun rotation speed [°/sec]	4.37	4.37
Position accuracy (arcsec, on the sky)	0.055	0.036
Position resolution (arcsec, on the sky)	0.020	0.013

Figure 2.3: The cryogenic part (left) and the non cryogenic part (right) of the receiver.

Figure 2.4: Final installation of the MF receiver at the cassegrain focus of Medicina 32-m dish.

2.2 Total Power Backend

A total power analogue backend was designed for continuum observations with the MF receiver. The backend consists of 14 Printed Circuit Boards (PCBs), with a digital part for board control and set-up, and a voltage-to-frequency converter for each channel to digitize the detected signals. The digitized signal packets are sent to the acquisition system through LAN (Local Area Network).

Since the backend is designed for the SRT, each board has three input ports that can be connected to any receiver located at the three foci of the antenna. The backend can provide two backend outputs for each input prior to the signal detection. This facility allows the system to send the receiver output to any of the backends available - for example to a FPGA (Field Programable Gate Array) backend (VLBI / spectroscopy observations) or to a remote backend. The backend is integrated with an equalizer to compensate for different attenuations of the coaxial cable coming from the antenna foci, a variable attenuator to adjust the signal levels in the linear regime of the receiver and a filter bank to reduce the bandwidth in case of necessity. With all these characteristics, the backend works both as acquisition system and signal distributor.

The control management of the acquisition system is done using a computer with an embedded FPGA board which also allows the control system to remotely set up the equalizer, attenuation, filter bandwidth and sampling rate of the acquisition. It is also possible to control the switching on and off of a noise source with known temperature. The signal is injected through the receiver chains and can be used to track and overcome the electronic gain variation of the receiver.

The key parameters of the total power analogue backend are summarized as:

- 14 x 3 IF inputs in the range of 0.1 to 2.1 GHz
- Two IF outputs in the range 0.1 to 2.1 GHz
- Bandwidths: 230, 725, 1200 and 2000 MHz
- Cable equalization up to 12 dB
- 0 to 15 dB variable attenuators, 1 dB step
- Sample rate of 0.001 to 1 sec

- Up to 21 bit resolution
- Automatic cancellation of output offset
- Noise-source chopping frequency of 0.5 to 500 Hz

2.3 The Medicina 32-m Radio Telescope

As already mentioned the MF receiver was mounted on the Medicina 32-m dish located at 35 km south-east of Bologna (Italy) in 2008, to test the scientific capabilities of the receiver while waiting for the SRT to be completed. The Medicina 32-m Radio Telescope constructed in 1983, is a dual reflector system (see Figure 2.5). The primary reflector is a paraboloid and the secondary reflector is hyperbolic in geometry. The specifications of the telescope are summarized in Table 2.3.

Figure 2.5: The Medicina 32-m Radio Telescope (courtesy Istituto di Radioastronomia, Bologna).

Table 2.3: Specification of the Medicina 32-m Telescope

Diameter of primary reflector	32 m
Diameter of secondary reflector	3.2 m
Focal length	97.36 m
Rms pointing accuracy	0.002°
Total surface accuracy	0.6 mm (at 60° of elevation)
Antenna efficiency	38% at 22 GHz

2.4 Antenna Parameters

In this section, the definitions of the key antenna parameters are described. These parameters characterizing the capabilities of the receiver should be known in advance to plan astronomical observations.

2.4.1 System temperature

The system temperature of an antenna can be defined as a measure of total noise contribution in the system when observing a blank sky. Since the noise coming from the sub-systems forming the telescopes is uncorrelated, the different noise contributions add up linearly. Therefore the system temperature T_{sys} can be given as:

$$T_{sys} = T_{receiver} + T_{cover} + T_{sky} + T_{spill} + T_{CMB} \tag{2.1}$$

where $T_{receiver}$ is the noise temperature of the receiver; T_{cover} is the temperature of the cover placed on the MF receiver; T_{sky} is the sky contribution; T_{spill} is the spillover temperature and T_{CMB} is the background sky brightness. The sky contribution T_{sky} can be given as:

$$T_{sky} = T_{atm} * [1 - e^{-(\tau X_{air})}] \tag{2.2}$$

$$X_{air} = \sec(ZA)$$

$$X_{air} = \frac{1}{\cos(90^\circ - El^\circ)} \tag{2.3}$$

where T_{atm}, X_{air} and ZA are atmospheric temperature, airmass and zenith angle respectively.

2.4.2 Spillover temperature

The feed is supposed to collect radiation focused by the reflector but often it also picks up stray radiation beyond the edge of the reflector. This contribution is known as spillover temperature. Spillover temperature in a dual (primary and secondary) reflector antenna has two components described below and shown in Figure 2.6:

(i) the feed spillover beyond the rim of the

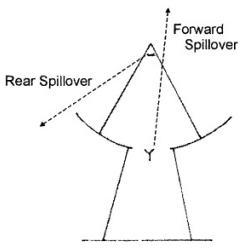

Figure 2.6: Pictorial view of the spillover temperature of the antenna in dual mirror system.

subreflector known as forward spillover.
(ii) the scattered radiation past the rim of the main reflector known as rear spillover.

2.4.3 Antenna temperature

The Antenna temperature T_a is a measure of the signal strength in radio astronomy. It is defined as the temperature of a black-body enclosure which, if completely surrounding a radio telescope, would produce the same signal power as the source under observation. The mathematical expression can be given by:

$$P = k_B T_a \tag{2.4}$$

where k_B is the Boltzmann constant and T_a is the temperature of black body enclosure.

2.4.4 Antenna gain

The gain of the antenna expressed in $\frac{K}{Jy}$ depends on the collecting area of the telescope and on the efficiency of the surface in focusing the incident radiation. Theoretically the antenna gain is directly proportional to the effective collecting area and can be given as :

$$G = 10^{-26} \frac{m \eta_A A_g}{k_B} [\frac{K}{Jy}] \tag{2.5}$$

where η_A, k_B and A_g are the antenna efficiency, the Boltzmann constant and the geometric area respectively.
For Medicina antenna, the constant

$$10^{-26} \frac{m A_g}{k_B} \approx 0.292 \tag{2.6}$$

There are many factors which can degrade the antenna efficiency and influence the gain of an antenna severely. A brief description of these parameters is discussed in the following.

Blockage efficiency (η_{bloc}): The incident radiation on and reflected from the parabolic reflector encounters shadowing from both the feed/subreflector central blockage and from the subreflector support struts. This blockage (i) reduces the total area available for incident radiation; (ii) reduces the total amount of energy available for collimation in the main lobe of antenna beam; (iii) increases the sidelobes due to

discontinuous aperture distribution and scattering of energy incident on the blockage area.

Cross-polarization (η_x): An antenna receives the maximum signal when the polarization ellipse of the incident electric field has the same axial ratio, the same tile angle and the same sense of polarization as that of receiving antenna in a given direction. When the polarization of the incident wave does not match with that of the receiving antenna, a polarization loss occurs due to mismatch. This is taken into account by the cross-polarization efficiency.

Phase efficiency (η_{ph}): The phase efficiency results from the loss due to feed phase characteristics: (i) non coincidence between the feed phase center and the focal point; (ii) any deviation of phase in the aperture plane from its ideal value.

Spillover efficiency (η_{spill}): To most effectively utilize the large area of a reflector antenna, the energy radiated from the feed must be distributed over the aperture with a reasonable degree of uniformity. For most feeds a significant amount of energy radiates in angular regions outside the subtended angle of the reflector. The spillover efficiency is defined as the percentage of the total energy radiated from the feed that is intercepted by the reflector. Spillover efficiency is one of the most significant factor in the antenna efficiency and is very difficult to evaluate due to the edge discontinuities.

Diffraction loss efficiency (η_{diffr}): It originates from diffraction due to edge effects for both primary and secondary reflectors.

Taper efficiency (η_{taper}): It is a measure of the nonuniformity of the field across the aperture caused by the tapered radiation pattern. Essentially because the illumination is less towards the edges, the effective area being used is less than the geometric area of the reflector.

Surface efficiency (η_{surf}): The surface efficiency accounts for the surface errors arising from fabrication errors or panel adjustment inaccuracies. This situation is modeled statistically by Ruze by carrying out an analysis of the effect of the random errors on the telescope's aperture efficiency (Ruze, 1952). The surface efficiency of a telescope using the Ruze formula (Ruze, 1952) can be given as:

$$\eta_{surf} = e^{-(4\pi\frac{\sigma}{\lambda})^2} \tag{2.7}$$

where σ is the rms surface error given as:

$$\sigma \approx \sqrt{\sigma_P^2 + \sigma_{Sec}^2 + \sigma_{Gravity}^2 + \sigma_{Align}^2}$$

where $\sigma_{Gravity}$ is the rms error on the surface accuracy due to gravity deformation and it varies with elevation; σ_P and σ_{Sec} represent the rms error on the surface accuracy due to primary and secondary mirror panels respectively; σ_{Align} is the rms error in the alignment of mirror panels.

Feed insertion loss efficiency (η_{floss}): When the electromagnetic energy passes through the feed, the waveguide attenuates the incident signal. Therefore the power illuminating the aperture is slightly less than the supplied one, causing insertion losses. Generally insertion losses are very low.

VSWR efficiency (η_{vswr}): VSWR efficiency is derived from the reflection at the feed port due to impedance mismatch.

Surface loss efficiency (η_{sloss}): The reflector surface sometime conducts small electric currents. Therefore ohmic losses arise due to material resistivity, and are taken into account as surface loss efficiency.

In conclusion the overall antenna efficiency can be calculated as:

$$\eta_A = \eta_{bloc} * \eta_x * \eta_{ph} * \eta_{spill} * \eta_{diffr} * \eta_{taper} * \eta_{surf} * \eta_{floss} * \eta_{vswr} * \eta_{sloss} \tag{2.8}$$

2.5 Laboratory Measurements and Simulations

This section presents the expected values of antenna parameters for the MF receiver at the Medicina antenna (system temperature, spillover temperature, antenna gain, FWHM of the antenna beam, sky distance between adjacent beams) as obtained either from laboratory measurements or simulations.

2.5.1 System temperature

The temperature of the MF receiver has been measured in the laboratory using the conventional hot and cold load method. The following assumptions are made for the factors contributing to the system temperature (see Eq. 2.1):
T_{cover} = 5K, **Measured** (The receiver is covered to protect it from the outside ambient).
T_{spill} = 5-7 K, **Estimated**

$T_{atm} = 278$ K, **Estimated**

$\tau = 0.1$ **Estimated** (Average opacity during the year)

With these assumptions the system temperature T_{sys} at 22 GHz was estimated $\approx$ 75 K for the central feed at an elevation of 45°.

2.5.2 Antenna gain

The antenna gain for the central and lateral feeds was estimated through simulations. The factors contributing to the antenna efficiency (see Eq. 2.8) are listed in Table 2.4 and the surface efficiency of the telescope is described by the Ruze formula (Ruze, 1952) (see Eq. 2.7).

Table 2.4: Antenna efficiency parameters at 22 GHz

Efficiency	**In axis**[a] **(%)**	**Off-axis**[b] **(%)**
η_{taper}	95.7	95.6
η_{ph}	99.3	99.3
η_{spill}[c]	70.4	70.3
$\eta_{blocSec}$	97.3	97.2
$\eta_{blocSrut}$	94.0	94.0
$\eta_x * \eta_{diffr} * \eta_{sloss}$	98.0	98.0
η_{floss}	92.0	92.0
η_{vsrw}	99.0	99.0
η_{surf}	see below	see below

[a]Central feed
[b]lateral feeds
[c]It consist of two contributions: Spillover efficiency of primary reflector and Spillover efficiency of secondary reflector.

The main components to be borne in mind while estimating the surface efficiency are the panel adjustment inaccuracies, gravity and fabrication errors. As the surface efficiency is Gaussian in nature, a small error in estimating the surface efficiency can severely affect the overall efficiency of the antenna and can degrade the antenna gain. The main factors contributing to the rms surface error σ for the Medicina dish are given below:

$\sigma_P = 0.40$ mm

$\sigma_{Sec} = 0.35$ mm

$\sigma_{Align} = 0.2$ mm

$\sigma_{Gravity} = \sqrt{\sigma_{90}^2 + \sigma_{60}^2 + \sigma_{45}^2 + \sigma_{30}^2 + \sigma_{20}^2} = 0.70$ mm

where the factors contributing to $\sigma_{Gravity}$ are listed in Table 2.5.

Table 2.5: Rms surface error due to gravity deformation as a function of elevation

Elevation (°)	**rms error due to gravity deformation**[a] (mm)
90	0.58
60	0.19
45[b]	0.00
30	0.25
20	0.40

[a]For our calculation we have considered a 20% increase in each measurement to keep into consideration the degradation due to the aging of the telescope structure.
[b]The panel alignment is done at this elevation.

Using Eq. 2.7 the value for the surface efficiency was obtained to be 73.3%. From Eq. 2.8 the antenna gain value obtained is 0.105 $\frac{K}{Jy}$ at an elevation of 45° for both central and lateral feeds.

2.5.3 FWHM of antenna beam

The full width at half maximum (FWHM) size of the feed is calculated as:

$$FWHM(radians) = [1.02 - 0.0135 * T(dB)] * \lambda/D \tag{2.9}$$

where T is the illumination taper, λ is the incident wavelength and D is the diameter of the primary reflector.

The FWHM of the feed at 18 GHz, 22 GHz and 26 GHz (two edge and one central frequency of the MF receiver) are listed in Table 2.6.

Table 2.6: Beam size of each horn on Medicina antenna at different frequencies

Frequency (GHz)	Taper[a](dB)	FWHM (arcsec)
18	-3.2	115
22	-5.3	96
26	-7.7	84

[a]Tapering at 9.4° subreflector edge of the Medicina antenna.

2.5.4 Sky distance between two adjacent feeds

The sky distance between two adjacent feeds is given by:

$$d_{sky} = d/f = 212'' \tag{2.10}$$

where d is the physical spacing between the feeds and f is the focal length of the secondary focus of Medicina telescope ($d = 100$ mm and $f = 97.36$ m).

The expected values of antenna parameters obtained from laboratory measurements and simulations describing the MF receiver performance at 22 GHz on Medicina antenna are summarized in the Table 2.7.

Table 2.7: Antenna performance parameters at 22 GHz

System temperature (El $= 45^{\circ}$, $\tau = 0.1$)	75 K (central feed)
Antenna gain (central & lateral feeds)	0.105 K/Jy ($\sigma = 0.70$)
FWHM	$96''$
Sky distance between the feeds	$212''$

2.6 Pointing Calibration: Test measurements

This section presents the test measurements obtained by observing an astronomical source in order to retrieve a pointing model for the multi-feed receiver and to better characterize the receiver performance at Medicina. There are many parameters, for example surface accuracy, thermal deformation, gravity, pointing errors and focusing, that can limit the high frequency performance of the antenna. Pointing accuracy becomes very important at high frequency, since the maximum errors allowed in the sky coordinates (α, δ) should always satisfy the condition $[(\sigma_\alpha \cos\delta)^2 + (\sigma_\delta)^2]^{\frac{1}{2}} \leq \frac{FWHM}{10}$; and the higher the frequency the smaller the full width at half maximum (FWHM) of the antenna beam. Typically a telescope beam pattern is considered to be Gaussian. Therefore a significant relative offset between the telescope pointing direction and the actual source position can result in a significant reduction of the telescope gain, as shown in Figure 2.7 (a). This can severely affect the signal to noise ratio (SNR) and the calibration of the observations. In addition, in presence of poor focus of the telescope, the source gets diffused and is not concentrated at the center of the antenna beam where the telescope gain is maximum (Figure 2.7 (b)). This can also degrade the object's SNR.

Figure 2.7: Effect of pointing error (Figure (a)) and of poor focus of the telescope (Figure (b)).

2.6.1 Pointing model

Generally the instrumental coordinates of a target are read into the antenna control computer directly from the encoders attached with the two mount axes of the telescope. The instrumental coordinate system may have many imperfections: for example axis misalignment or instrument coordinate system that may be rotated with respect to the true azimuth and elevation. These imperfections are usually taken into account using a pointing model which is a routine practice for telescopes devoted to astronomy. The basic model used at most radio telescopes is a variant of the model described by Ulich (1981) (for parallel work on pointing models for optical telescopes, see Wallace, 1975). The general philosophy at the heart of these models is that the model should reflect real effects, such as axis misalignments, flexures, etc. These imperfections, as well as gravity or any remaining systematic errors should be removed using empirical functions. Recent developments in pointing algorithms advocate the use of empirical functions such as spherical harmonics to describe the pointing model.

2.6.1.1 Pointing equations

The physical model used for the telescope pointing can be described as follows. Let assume that A and E are the true azimuth and elevation of a source. The encoder readings (instrumental coordinates) can be given by:

$$A_{encoder} = A + \Delta A \tag{2.11a}$$

$$E_{encoder} = E + \Delta E \tag{2.11b}$$

where ΔA and ΔE are the total azimuth and elevation encoder pointing corrections respectively, given as:

$$\Delta A = IA + CA\sec(E) + NPAE\tan(E) + AN\tan(E)\sin(A) - AW\tan(E)\cos(A) \quad (2.12a)$$

$$\Delta E = IE + ECEC\cos(E) + AN\cos(A) + AW\sin(A) + R(P_s, T_s, RH, E) \quad (2.12b)$$

A brief description of the terms used in the pointing model is given in Table 2.8.

Table 2.8: Basic telescope pointing model terms; col.(1) gives the notation of the term; col.(2) gives the physical meaning of each term.

Term[a]	Physical meaning
IA	Azimuth encoder zero-point offset
CA	Collimation error of the electromagnetic axis
NPAE	Non-perpendicularity between the mount azimuth and elevation axes
AN	Azimuth axis offset/misalignment north-south
AW	Azimuth axis offset/misalignment east-west
IE	Elevation encoder zero-point offset
ECEC	Gravitational flexure correction at the horizon
R(P_s,T_s,RH,E)	Atmospheric refraction correction, which is a function of ambient pressure (P_s), temperature T_s, relative humidity (RH) and the elevation of the source

[a]These notations are used in the TPOINT pointing analysis program.

2.6.1.2 Additional terms

There are other additional physical deformations of the telescope structure which can be introduced in the pointing model:

(1) For radio telescopes with a wheel-and-track azimuth mount, it is often necessary to correct for irregularities in the azimuth tracks as a function of azimuth.

(2) If elevation drive/encoder is mis-centered an additional gravity flexure term ($\sin(E)$) should also be included in the pointing model for the overall gravity correction.

2.6.1.3 Determining coefficients and rms pointing error

The coefficients mentioned in Eq. 2.12 are derived from a least-square fit to a collection of 50 or more pointing measurements. These measurements should be

performed in such a way that represent the telescope pointing behavior over the entire azimuth and elevation ranges. Once all these coefficients are obtained, a simultaneous linear least-square fit of the coefficients in Eq. 2.12 is carried out to minimize the mean-squared pointing error. Then these coefficients are inserted into the mount control software to be used to calculate the necessary pointing corrections. It is worth mentioning that these coefficients are measured frequently to keep the pointing model of the telescope updated.

2.6.2 Pointing: Optical alignment of MF receiver with the mirrors

When the MF receiver was mounted on Medicina 32-m dish, the optical alignment of the MF receiver was investigated to quantify the telescope's pointing accuracy for the MF receiver. Since the total power analogue backend was still under construction, the MF receiver was coupled with the VLBI acquisition system (Mark 4) that has a 400 MHz bandwidth. The optical alignement of the receiver was checked by performing cross-scans across a point like source W3OH[1] with the mechanically determined optical alignment[2]. The plot in Figure 2.8 shows the cross-scan on source W3OH. The green line in the plot shows the elevation scan on W3OH while the red one shows the azimuth scan at an elevation of 33°. It can be clearly noticed from the figure that the antenna beam is asymmetric in azimuth and elevation axes with an offset and FWHM larger than expected. Also a significant amount of power is lost in the sidelobes in both the axes. The beam asymmetry in azimuth and elevation axes implies that the telescope optics (primary mirror, secondary mirror and feed) is not properly aligned.

2.6.3 Strategy adopted to optimize the optical alignment for MF receiver

As the MF receiver is mounted on the cassegrain focus of Medicina 32-m dish, the optics of the receiver can be aligned by using the subreflector geometry. The subreflector is equipped with five actuators providing five degrees of freedom for the movement; three degrees for translation [east-west (X-axis), north-south (Y-axis) and Z-axis] and two degrees of freedom for tilting. Figure 2.9a shows the subreflector geometry. The movements in X & Y directions are done using X & Y actuators

[1] W3OH is a circumpolar, bright source at 22 GHz.

[2] The mechanically determined optical alignment is the alignment obtained using an optical collimator when mounting the receiver on the telescope.

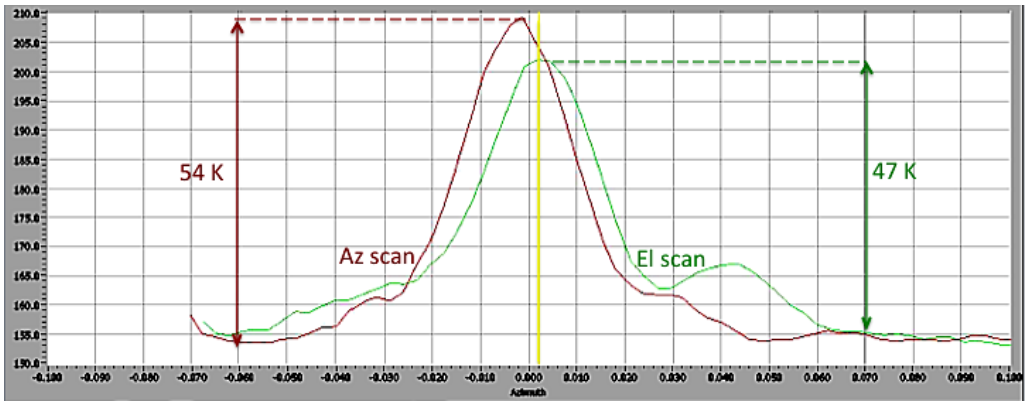

Figure 2.8: Cross-scans across the source W3OH. Green line shows the elevation scan and red line shows the azimuth scan (at an elevation of 33°) with the mechanically determined optical alignment. The X-axis represents the offset (in degrees) between the telescope pointing direction and the source position, Y-axis denotes the temperature of the source. The antenna beam is asymmetric in elevation and azimuth axes with an offset relative to each other. The FWHM is larger than expected and a significant sidelobe can also be noticed in the elevation scan.

while tilting and focusing is done by moving Z1, Z2, and Z3 actuators situated at the vertices of an isosceles triangle. A zoomed view of the Z-axis actuators positions is shown in Figure 2.9b where again Z1, Z2, Z3 are the positions of the actuators; O is the centre of the isosceles triangle; L and r are the base and height of the triangle respectively; h is the height of the centre of triangle. The equation of motion for the subreflector can be given by:

$$x(mm) = AX - AX_0 \tag{2.13}$$

$$y(mm) = 0.9903(AY - AY_0) \tag{2.14}$$

$$z(mm) = 0.1392(AY - AY_0) + 0.3333(AZ1 - AZ1_0) + 0.3333(AZ2 - AZ2_0) + 0.3333(AZ3 - AZ3_0) \tag{2.15}$$

$$\theta_x(radian) = \frac{(AZ1 - AZ1_0)}{1791} - \frac{(AZ2 - AZ2_0)}{3582} - \frac{(AZ3 - AZ3_0)}{3582} \tag{2.16}$$

$$\theta_y(radian) = \frac{(AZ2 - AZ2_0)}{2068} - \frac{(AZ3 - AZ3_0)}{2068} \tag{2.17}$$

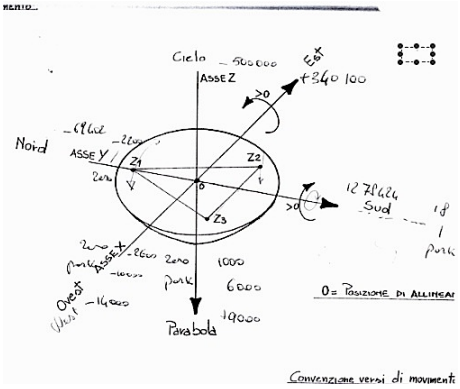

(a) Subreflector geometry. Z1, Z2, Z3 show the position of three actuators used to tilt & focus the subreflector.

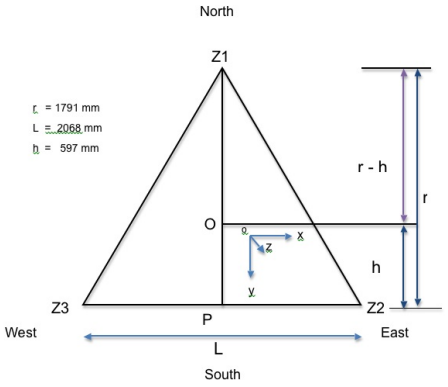

(b) Positions of the three actuators situated at the vertices of an isosceles triangle. O is the center of the triangle coinciding with the rotation axis of the subreflector.

Figure 2.9: Subreflector geometry at Medicina 32-m dish

2.6.4 New optical alignment for MF receiver

A number of cross-scans with different subreflector positions were performed across source W3OH to maximize the peak amplitude of the source in the main lobe of the antenna beam. Measurements were done by moving the subreflector in X, Y, Z axes and tilting it about the X and Y axes to get the best optical alignment and focus for the MF receiver.

Figure 2.10 shows the cross-scan on W3OH with optimized optical alignment. Red and green lines show the azimuth and elevation scans (at an elevation of 66°)respectively. Figure 2.10 shows that with the new alignment the antenna beam is symmetric in elevation and azimuth axes with lower and symmetrical sidelobes. The FWHM of the antenna beam matches with the theoretical value. Also the peak amplitude in both beams are similar now with a maximum increment of $\approx 50\%$.

Many test observations were carried out to get the optimized subreflector position parameters as a function of elevation. The subreflector position polynomials as a function of elevation with mechanically determined and optimized optical alignment are shown in Figures 2.11 and 2.12 and are listed in Table 2.9. It is important to mention that, in order to obtain the new optimized alignment, the subreflector was tilted strongly in one direction by adjusting the Z3, actuator and as a result the Z3 actuator is at the limit of its movement.

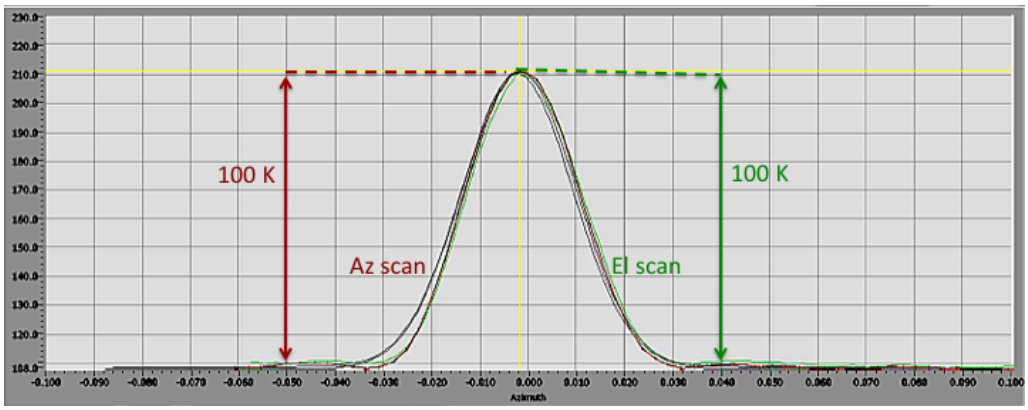

Figure 2.10: Cross-scans across the source W3OH with optimized optical alignment. Red line shows the azimuth scan at an elevation of 66° while green line shows the elevation scan. It is remarkable that with the new alignment ≈ 50% increment in the power in the main lobe was achieved with a reduction of sidelobes.

Table 2.9: Subreflector position polynomials for mechanical and optimized optical alignment.

Subreflector position polynomials	
Mechanical optical alignment	Optimized optical alignment
$X^a = 0.000000x^{4b} - 0.000099x^3 + 0.007027x^2 - 0.190960x + 1.613651$	$X = 15$
$Y^c = 0.00140x^2 + 0.06065x - 5.52643$	$Y = -0.000x^2 + 0.502x - 34.73$
$Z1^d = 0.0007x^2 - 0.0008x - 1.4474$	$Z1 = -0.0026x^2 + 0.2194x - 13.809$
$Z2^e = (9e-6)x^2 - 0.0064x + 0.2489$	$Z2 = 0.0097x^2 - 0.976x - 37.203$
$Z3^f = (2e-7)x^2 - (2e-5)x - (5e-5)$	$Z3 = -0.0035x^2 + 0.0563x + 63.439$

[a] X represents 'AX'
[b] x axis is the elevation axis.
[c] Y represents 'AY'
[d] Z1 represents 'AZ1'
[e] Z2 represents 'AZ2'
[f] Z3 represents 'AZ3'

2.6.4.1 Pointing model and expected rms pointing error for MF receiver at Medicina telescope

After the new subreflector position polynomials were implemented into the Subreflector Control Unit (SCU), a new pointing model was evaluated by observing many sources. In section 2.6.1 the pointing model was discussed in detail and all the terms which can be used in pointing algorithms are listed in Table 2.8. An additional ad hoc correction term is used at Medicina due to the presence of a systematic offset. The rms pointing error for MF receiver in both azimuth and elevation direction is approximately 6-8 arcsec in normal weather conditions. The pointing model for the MF receiver is being regularly updated. The description of the pointing model

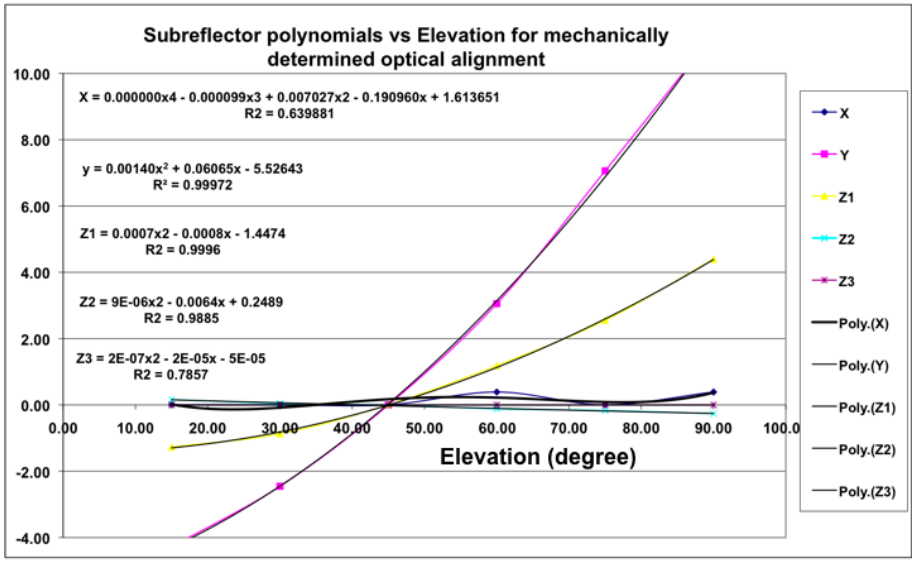

Figure 2.11: Subreflector position parameter polynomial as a function of elevation for mechanically determined optical alignment. Symbols represent the data observed to measure X, Y, Z1, Z2, Z3 parameters as a function of elevation while lines are the polynomials fitted to the data.

currently in use is given as: pointing model number - 00011, model generation time - 17/Jan/2009.

2.7 MF System Characterization at Medicina 32-m dish

Once the pointing model is retrieved for the MF receiver, the system characterization is done by observing an astronomical source to measure the antenna parameters. In order to perform fruitful astronomical observation, it is important to know the system temperature, spillover temperature and gain of the receiver for the observed frequency and elevation. Precise measurements of these parameters are very important to correctly calibrate the MF receiver data. All the antenna parameters are measured as a function of elevation and frequency for all the seven feeds[3].

2.7.1 System temperature and skydip procedure

Since the atmosphere has a significant opacity at centimeter wavelength, it is also necessary to apply a correction factor to compensate for atmospheric absorption.

[3]All the measurements for lateral feeds reported in the following refer to RCP only.

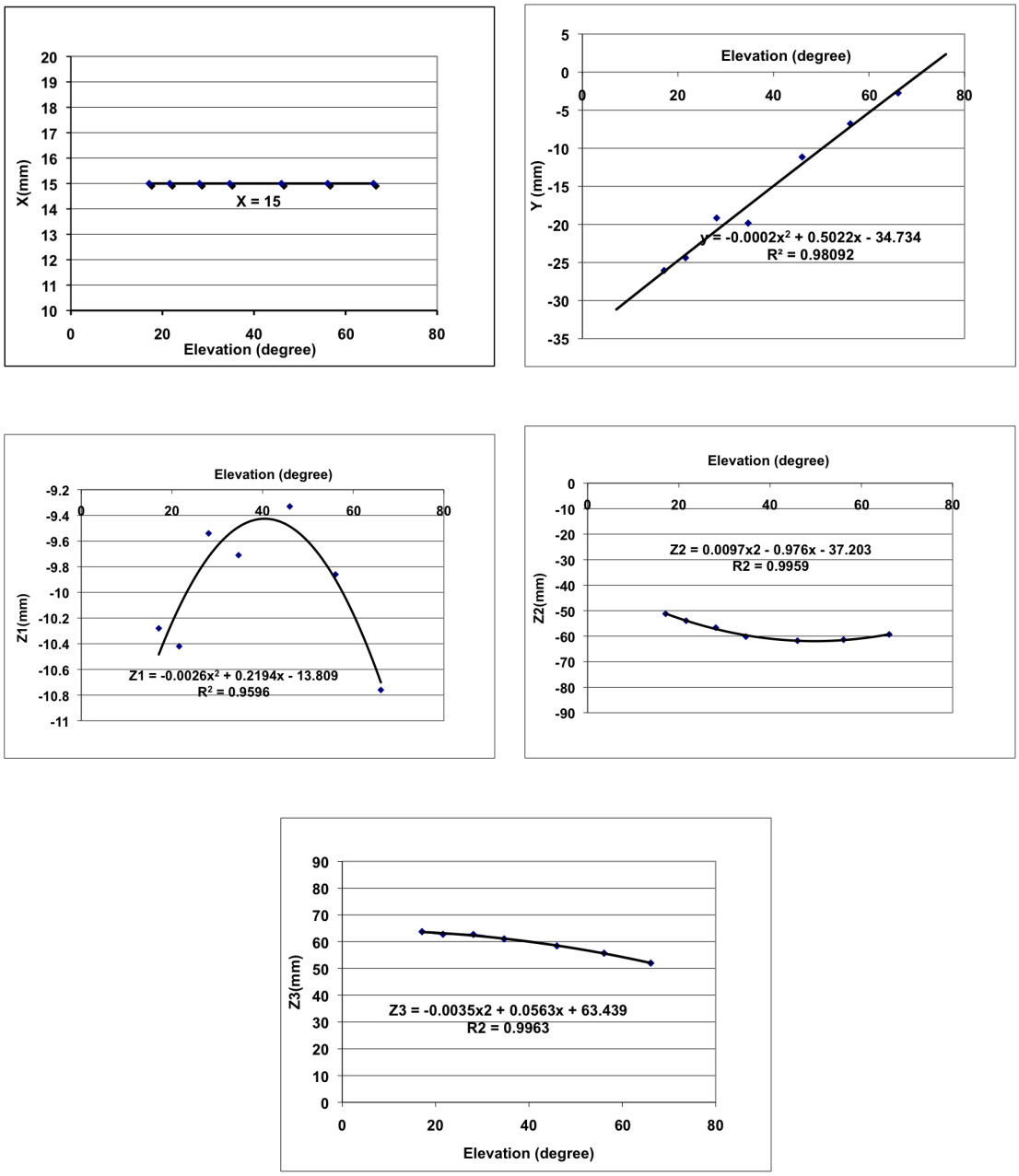

Figure 2.12: Subreflector position parameter polynomial as a function of elevation for optimized optical alignment. Diamonds are the data obtained for X, Y, Z1, Z2 and Z3 parameters vs elevation. Lines represent the polynomial fitted to the data.

The observed flux density of a source as a function of zenith angle can be given as:

$$S(ZA) = S_0 e^{-\tau \sec(ZA)} \tag{2.18}$$

where ZA is the zenith angle and S_0 is the true flux density of the source. The atmospheric opacity is measured using the standard *skydip procedure* where the system temperature is measured at different airmasses, i.e. at different elevations. This allows the noise temperature contribution of the atmosphere to be quantified. The T_{sys} from equation 2.1 can be rewritten as:

$$T_{sys} = T_0 + T_{atm} * [1 - e^{-\tau X_{air}}] \tag{2.19}$$

$$X_{air} = \frac{1}{\cos(90° - El°)}$$

where T_0 is the extrapolated noise temperature for $X_{air} = 0$ (sum of the $T_{receiver}$, T_{cover}, T_{spill}, T_{CMB}).

System temperature as a function of elevation was measured looking at the blank sky with the central feed of the MF receiver by moving the antenna continuously from 90° to 30° of elevation or vice versa. The system temperature measured (for both LCP and RCP) as a function of elevation at three different frequencies of the receiver, 18, 22 and 26 GHz is shown in Figures 2.13 (18 GHz), 2.14 (22 GHz) and 2.15 (26 GHz) respectively.

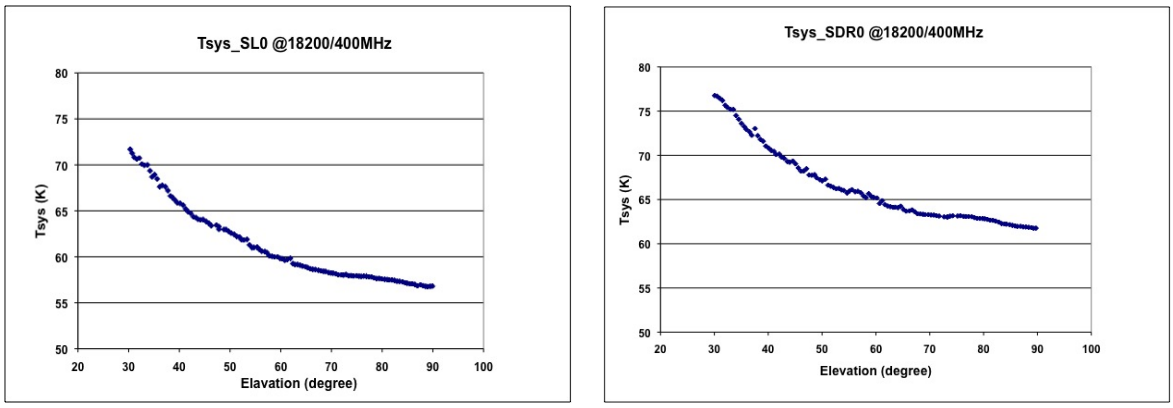

Figure 2.13: System temperature of the central horn of the MF receiver as a function of elevation at 18 GHz. LCP (left), RCP (right).

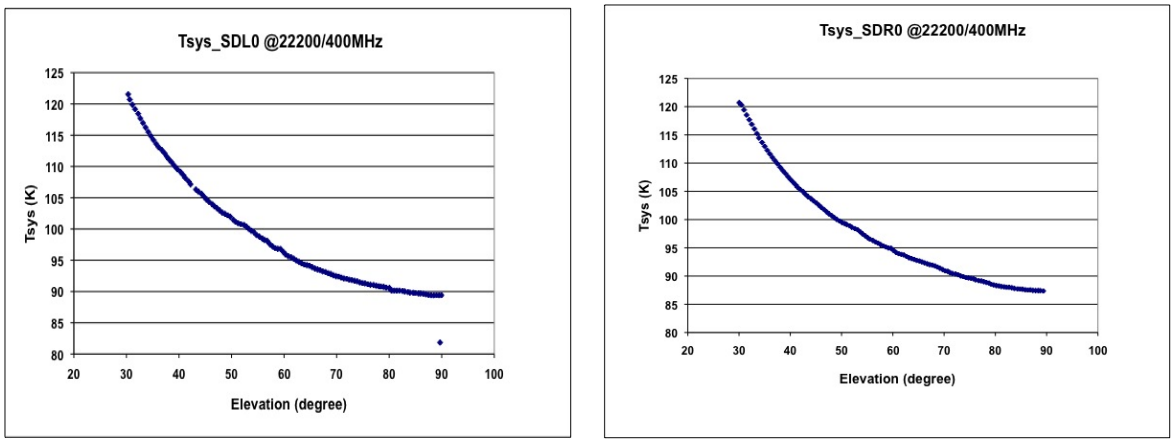

Figure 2.14: System temperature of the central horn of the MF receiver as a function of elevation at 22 GHz. LCP (left), RCP (right).

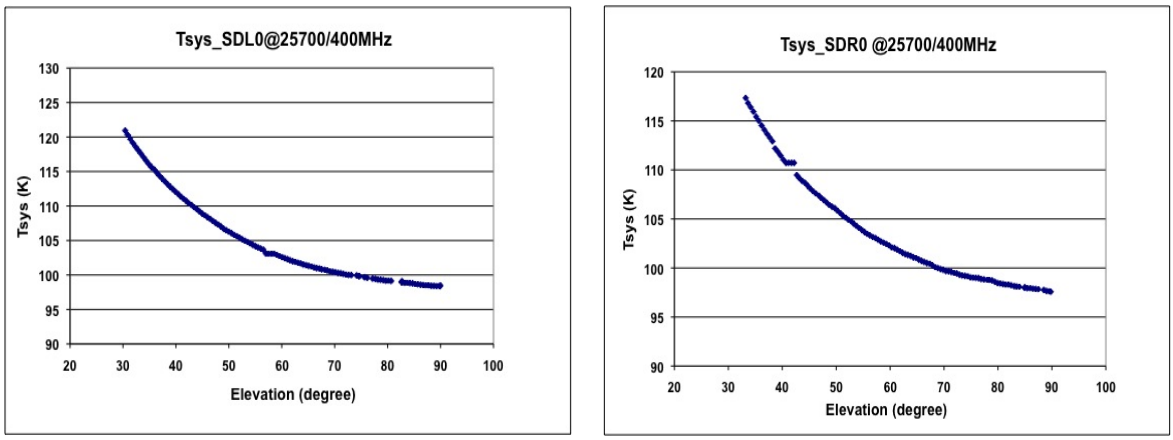

Figure 2.15: System temperature of the central horn of the MF receiver as a function of elevation at 26 GHz. LCP (left), RCP (right).

The airmass in the direction of the measurements can be calculated using Eq. 2.3. Figures 2.16, 2.17 and 2.18 show the system temperature as a function of airmass for left and right hand circular polarization of central feed. The symbols represent data, and lines represent fitting curves to the data, used to extrapolate T_0 for airmass = 0. Knowing T_0 and using Eq. 2.19 for the measurements of T_{sys} vs elevation and airmass, zenith opacity τ and T_{atm} can be calculated.

The atmospheric temperature T_{atm} at the three different frequencies is found to be 276 K. Opacities and system temperatures at the zenith for the different frequencies are listed in Table 2.10.

Once the system temperature was measured for the three different frequencies of the MF receiver (two edge and one central frequency) using the central feed,

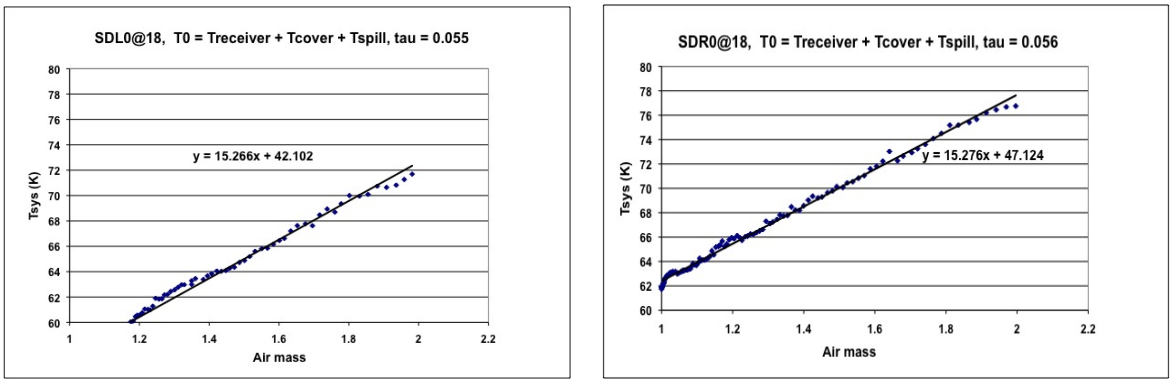

Figure 2.16: System temperature of central feed of the MF receiver as a function of airmass at 18 GHz. LCP (left), RCP (right). Symbols represent the data; lines represent the straight line fitted to the data.

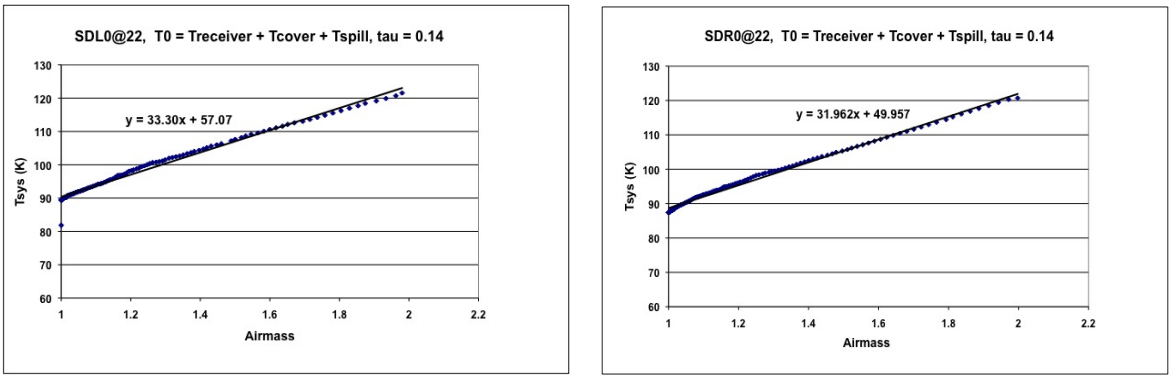

Figure 2.17: System temperature of central feed of the MF receiver as a function of airmass at 22 GHz. LCP (left), RCP (right). Symbols represent the data; lines represent the straight line fitted to the data.

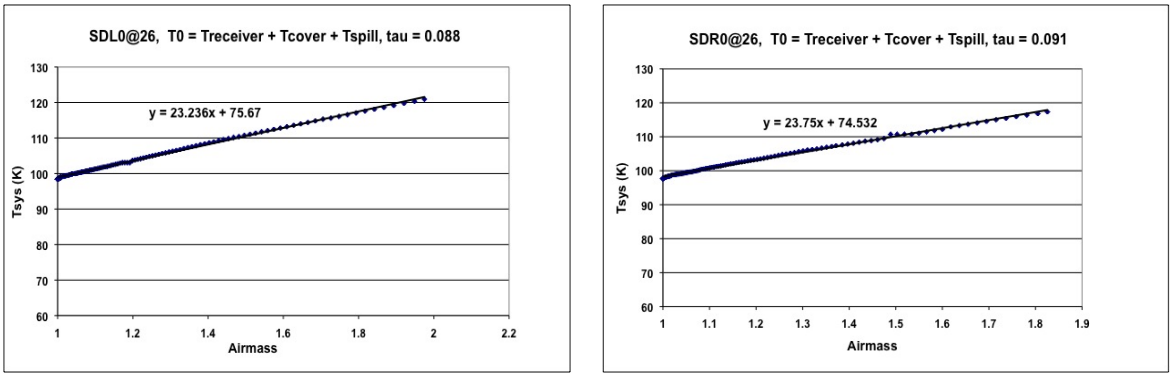

Figure 2.18: System temperature of central feed of the MF receiver as a function of airmass at 26 GHz. LCP (left), RCP (right). Symbols represent the data; lines represent the straight line fitted to the data.

a similar procedure was repeated to measure the system temperature at different elevation for the lateral feeds at 22 GHz only. The zenith opacity was measured

Table 2.10: Zenith opacity (τ) and system temperature (T_{sys}) measured at different frequencies

Frequency	18(GHz)		22(GHz)		26 (GHz)	
Parameter	LCP	RCP	LCP	RCP	LCP	RCP
Zenith opacity τ	0.055	0.056	0.140	0.140	0.088	0.091
T_{sys} at zenith	56	61	89	87	98	97

to be 0.07 for this set of measurements as they were performed in better weather conditions. Figure 2.19 shows the elevation dependence of the system temperature for the six feeds[4] of the MF receiver at 22 GHz (RCP only).

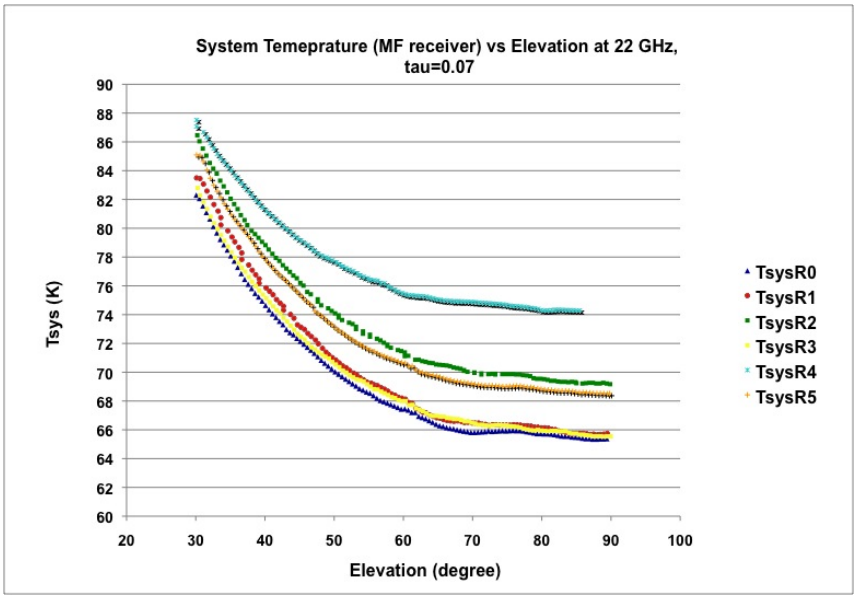

Figure 2.19: System temperature as a function of elevation for six feeds of MF receiver at 22 GHz (RCP only & $\tau = 0.07$). Feed 6 (channel RCP) was not working at the time of measurements.

2.7.2 Spillover temperature

After subtracting sky contribution, receiver temperature, cover and CMB from the system temperature (T_{sys}), the spillover temperature can be estimated. The spillover temperature as a function of elevation for the central feed at frequencies 18, 22 and 26 GHz is shown in Figures 2.20, 2.21 and 2.22 respectively. The spillover temperature estimated from the system temperature measurement sets at 18 and 22 GHz is a factor of 2-3 higher than the expected value (5-7 K). On the other hand 26 GHz spillover measurements are in agreement with the expectations. The spillover

[4]During the MF receiver mounting on Medicina telescope channels 6 RCP and 4 LCP went out of order.

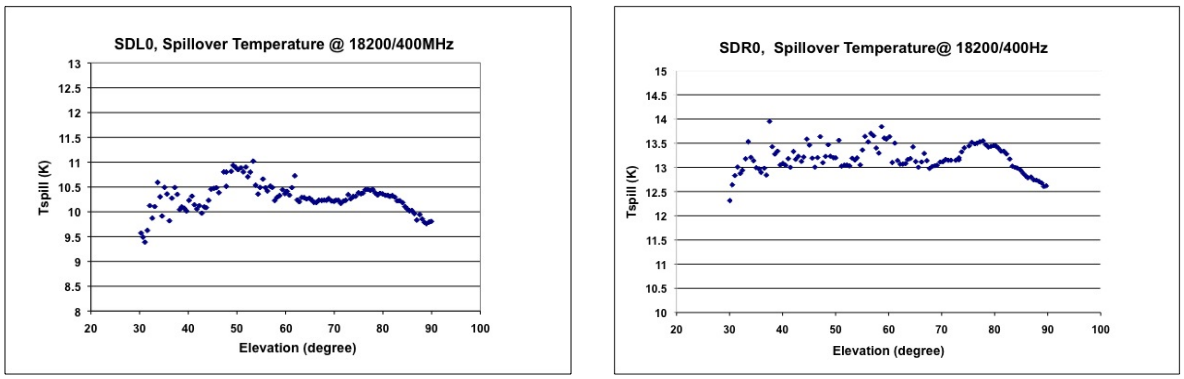

Figure 2.20: Spillover temperature of the central horn of the MF receiver as a function of elevation at 18 GHz. LCP (left), RCP (right).

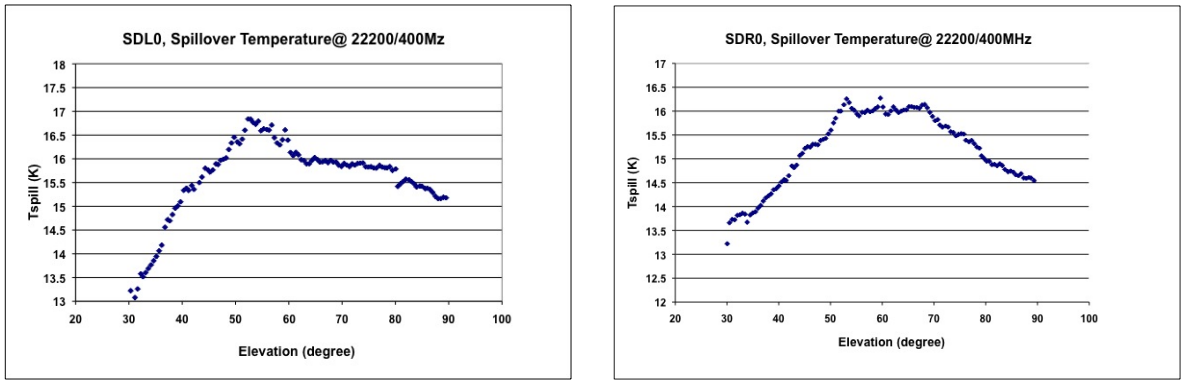

Figure 2.21: Spillover temperature of the central horn of the MF receiver as a function of elevation at 22 GHz. LCP (left), RCP (right).

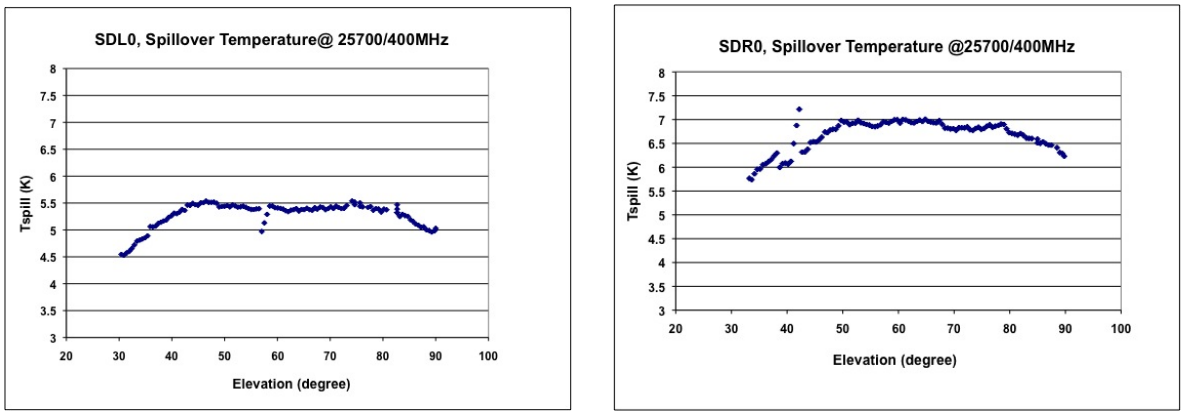

Figure 2.22: Spillover temperature of the central horn of the MF receiver as a function of elevation at 26 GHz. LCP (left), RCP (right).

temperature for the lateral feeds is also estimated following the same procedure as used for the central feed. The spillover temperature as a function of elevation for

both lateral and central feeds at frequency 22 GHz is shown in Figure 2.23[5]. Also in these cases spillover temperature tend to be a factor 2-3 higher than expected. This may be due to the fact that the optimized alignment for the MF has been obtained by tilting the subreflector in one direction (Z3) to the limit of its movement (see Section 2.6.4).

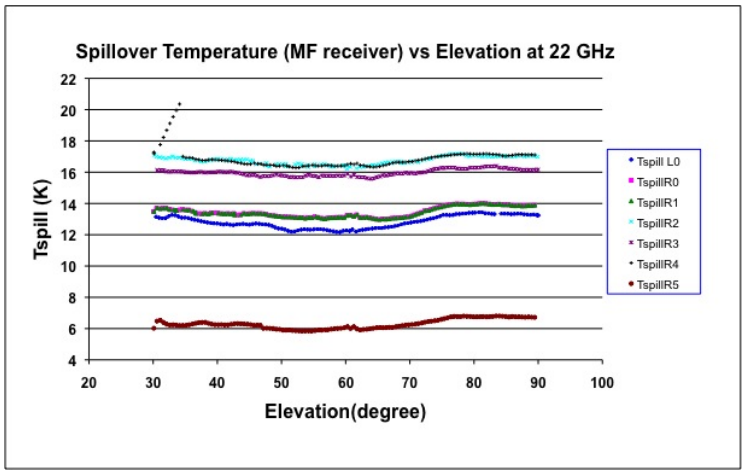

Figure 2.23: Spillover temperature as a function of elevation for six feeds of MF receiver at 22 GHz (RCP only). For central feed spillover temperature for both LCP and RCP is plotted. Feed 6 RCP was not working at the time of measurements.

2.7.3 Antenna gain

An evenly illuminated telescope has a gain curve that varies with telescope's zenith angle (elevation) in a predictable manner. It is always recommended to provide the telescope gain curve to the observer a priori. The telescope gain curve at different elevations is obtained by observing radio sources of known flux density. In order to retrieve the telescope gain curve we observed source DR21 with the MF receiver. Source DR21 is a bright source used as a primary calibrator at high frequency.

2.7.3.1 Central feed gain

Figure 2.24 shows the elevation dependence of the antenna gain measured at 22 GHz observing source DR21 using the central feed of the MF receiver. The antenna gain measured on source DR21 is lower than the value estimated through laboratory measurements and simulations (see Table 2.7). There are many factors responsible

[5] The odd feature present for horn 4 RCP is a measurement error. It does not have any physical significance.

for this discrepancy. One of the factors affecting the antenna gain is the distortion due to gravity which is solely a function of elevation.

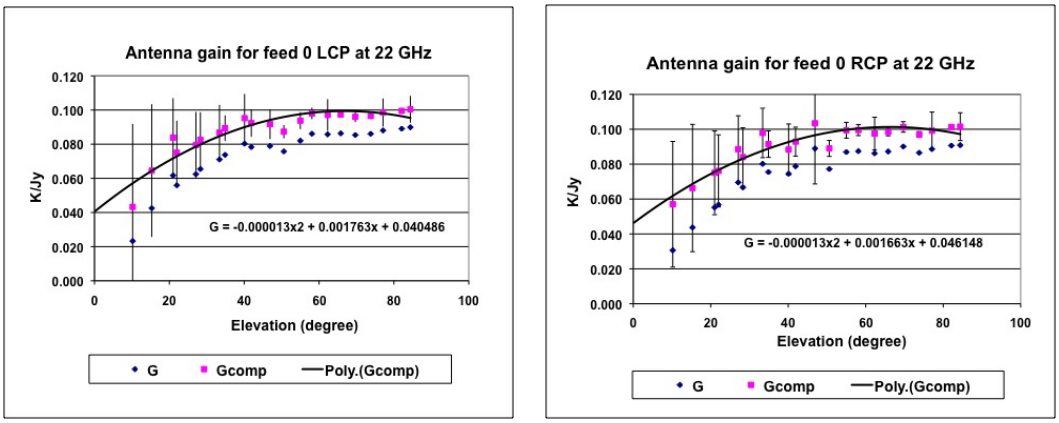

Figure 2.24: Antenna gain of the central feed of the MF receiver at 22 GHz, as measured by observing source DR21 at different elevations. Blue diamonds represent the data, pink squares show the data corrected for opacity and the line represents the polynomial curve fitted to the data corrected for opacity. LCP (left), RCP (right). 'x' character in the gain polynomials refers to the elevation (in degrees).

2.7.3.2 Lateral feed gains

The same procedure was repeated to measure the gain of lateral feeds. The antenna gain of lateral feeds relative to the central one are presented in Tables 2.11, 2.12 and 2.13, together with other relevant parameters. The antenna gain of lateral feeds are presented in three separate tables because they have been obtained in three different measurement sets, performed in different weather conditions. The antenna gain relative to the central feed is summarized in Table 2.14.

Table 2.11: Antenna gain of feeds 1 and 4 relative to central feed 0 (RCP only)

Feed	T_{sys} K	$T_{receiver}$ K	T_{diff}[a] K	T_{diff} ratio[b]	T_a K	Gain[c]
0	75.0	26.0	49.0	1.00	1.50	1.00
1	75.5	22.0	53.5	1.09	1.46	0.97
4	85	30.8	54.2	1.11	1.43	0.95

[a] $T_{sys} - T_{receiver}$
[b] T_{diff}(lateral feed) / T_{diff}(central feed)
[c] Gain relative to central feed

Table 2.12: Antenna gain of feeds 2 and 5 relative to central feed 0 (RCP only)

Feed	$T_{sys}K$	$T_{receiver}$ K	T_{diff} K	T_{diff} ratio	T_a K	Gain
0	77.0	26.0	51.0	1.00	1.50	1.00
2	80.5	25.8	54.7	1.07	1.48	0.99
5	80.0	35.4	44.6	0.87	1.45	0.97

Table 2.13: Antenna gain of feed 3 relative to central feed 0 (RCP only)

Feed	$T_{sys}K$	$T_{receiver}$ K	T_{diff} K	T_{diff} ratio	T_a K	Gain
0	75.0	26.0	49.0	1.00	1.55	1.00
3	74.0	23.0	51.0	1.04	1.5	0.97
6[a]	na	na	na	na	na	na

[a]Channel 6 RCP was not working at the time of measurement.

Table 2.14: Relative antenna gain for the seven feeds (RCP only)

Feed 0	Feed 1	Feed 2	Feed 3	Feed 4	Feed 5	Feed 6[a]
1	0.97	0.99	0.97	0.95	0.97	-

[a]Channel 6 RCP was not working at the time of measurement

2.7.4 Sky distance between adjacent feeds & FWHM of the antenna beam for each feed

In order to measure the sky separation between adjacent feeds and the FWHM beam size of each feed, cross-scans across the source DR21 were performed at 22 GHz. The axis passing through feeds 4, 0 and 1 was aligned with the azimuth axis of the antenna (Figure 2.25) using the derotator, and then an elevation scan across a bright source was performed with each of the three feeds to check the feed azimuth alignment.

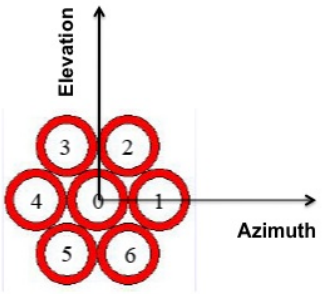

Figure 2.25: Geometry of the MF receiver after aligning the 4-0-1 feed-axis to the azimuth axis of the antenna.

Figure 2.26 shows elevation scans across source DR21. Green and yellow lines represent the elevation scans performed with feed 0[6](RCP), and red and blue lines correspond to the scans with feeds 1 and 4 respectively (RCP only). It can be noticed from Figure 2.26 that elevation offsets among the feeds are zero indicating

[6]The scan sequences with different feeds are 0 - 1 - 4 - 0; therefore for feed 0 (central) we have two scans: one in forward and one in backward direction

that the 4-0-1 axis is well aligned with the azimuth axis of the antenna.

Similarly an azimuth scan was performed across source DR21. Figure 2.27 shows the azimuth scans across source DR21 for feeds 1, 0 and 4 respectively (RCP only). Green, red and blue lines represent feed number 1, 0 and 4 respectively, and the black line shows the Gaussian fitting to the data to measure the FWHM of the antenna beam.

Similar procedures were followed for the feeds 2, 0, 5 and 3, 0, 6 in order to measure the FWHM of the antenna beam for all feed and the sky distance between adjacent feeds. Again FWHM of antenna beam for each feed is obtained using a Gaussian fitting. Table 2.15 summarizes the FWHM of the antenna beam and the sky distance of the the lateral feeds with respect to the central feed in both azimuth and elevation axes. Using the MF receiver geometry, the sky distance between the adjacent feeds can be calculated. For example, the sky distance between the central and feed 1 is 209″. The sky distance between the central and lateral feeds (see column 4 in Table 2.15) are in agreement with the expectation value (212″). Also the FWHM of the antenna beam is consistent with the theoretical value (96″).

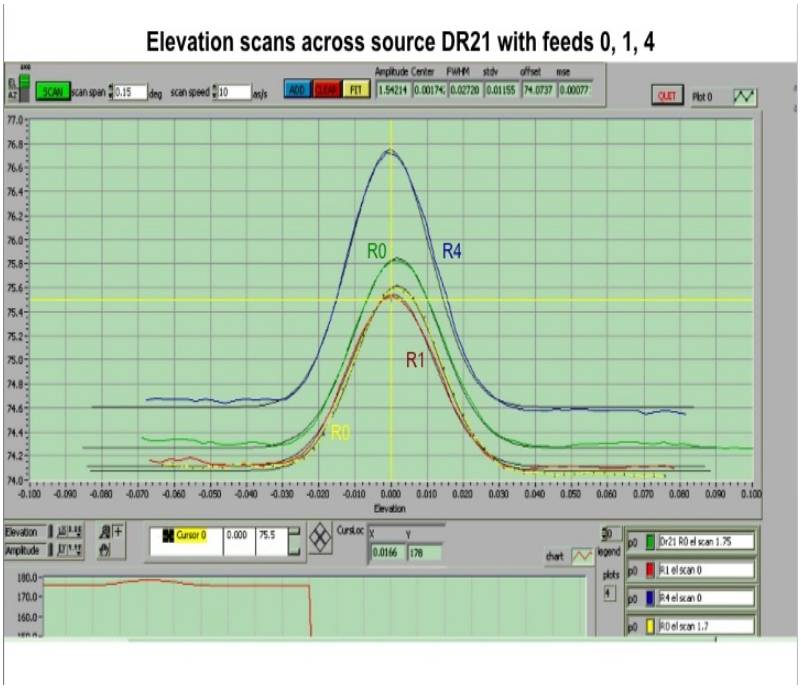

Figure 2.26: Elevation scans at 22 GHz across source DR21 performed with feeds 1, 0 and 4. Green and yellow lines represent scans with feed 0 while red and blue lines represent scans for feeds 1 and 4 respectively (RCP only).

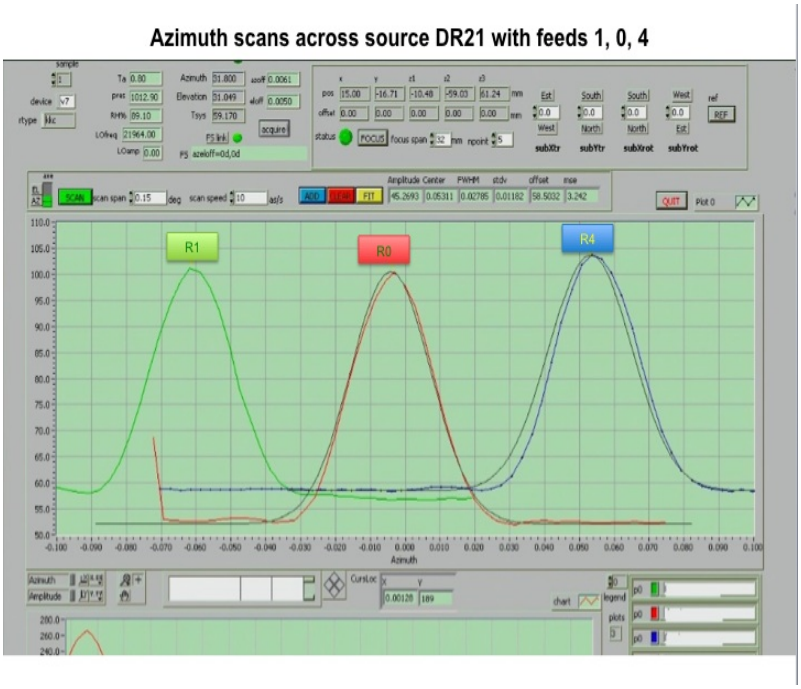

Figure 2.27: Azimuth scans at 22 GHz across source DR21 at an elevation of 31° performed with feeds 1, 0 and 4 (RCP only). Green, red and blue lines represent the azimuth scans across source DR21 at an elevation of 31° performed with feeds 1, 0 and 4 respectively (RCP only).

Table 2.15: FWHM of each feed and sky distance between adjacent feeds with reference to the central feed

Feed	X_{disp} [a] (arcsec)	Y_{disp} [b] (arcsec)	d_{sky} [c] (arcsec)	$FWHM$ (arcsec)
0	0.00	0.00	0	90.0
1	209.0	7.00	209	93.6
2	108.0	- 184.0	213	97.2
3	- 108.0	-180.0	209.4	93.6
4	- 216.0	7.00	216	93.6
5	- 104.0	191.0	217	97.2
6 [d]	na	na	na	na

[a] Azimuth offset relative to central feed (sky distance between adjacent feeds on azimuth axis)
[b] Elevation offset relative to central feed (sky distance between adjacent feeds on elevation axis)
[c] sky distance between the central and lateral feeds.
[d] It was not working at the time of measurements.

2.8 Discussion and Conclusions

In this chapter I presented a brief description of the new K-band multi-feed receiver and of the new total power analogue backend. The optical alignment of the MF receiver was optimized for the Medicina antenna leading to gain more power in the

main lobe of the antenna beam and to reduce the sidelobes. This work is important in view of the commissioning of the MF receiver at the SRT. New subreflector parameters were obtained and a new pointing model was retrieved for the MF receiver.

The system characterization of the MF receiver was done on Medicina 32-m telescope. System temperature and spillover temperature were measured as a function of elevation at three frequencies and the spillover temperature was found to be a factor 2-3 higher than the expected value at 18 and 22 GHz. We have characterized the antenna parameters at the central frequency (22 GHz) for both central and lateral feeds. The FWHM of the antenna beam for each feed matches with the theoretical value as well as the beam separation in the sky. The antenna gain curve was obtained as a function of elevation. The antenna gain is constant for elevation greater than 50°. At lower elevation the antenna efficiency is influenced by gravity.

Chapter 3

T_{cal} Estimation for the MF receiver

In this chapter I will discuss a mathematical approach developed for the precise estimation of the frequency-dependent T_{cal} value for the MF receiver (broad bandwidth receiver). Section 3.1 will describe the Y-factor method. In Section 3.2 a mathematical approach developed to calculate the frequency-dependent T_{cal} values for MF receiver will be discussed. Section 3.3 will briefly summarize the results obtained using the mathematical approach.

3.1 The Y-factor Method

When a radio signal passes through a receiver chain, the signal strength is measured in an arbitrary backend unit (volts or counts) and then converted into the physical unit of temperature by using a noise diode of known temperature (T_{cal}). The temperature of this noise diode and the noise temperature of the receiver is measured in the laboratory using the well known 'Y-factor' method. The precise measurement of these two quantities is very important to determine the system temperature. The noise diode is also important because the electronic gain of the receiver over time is monitored by switching on the noise diode.

The Y-factor method is the most extensively used technique to measure the noise temperature of receiver and T_{cal} values. Two loads (hot and cold load) at known temperatures T_h and T_c are alternately placed at the receiver input (horn mouth) and the total output powers P_h and P_c respectively, are measured. Then another measurement is performed by placing the cold load and switching on the noise generator, and then the output power P_{c+cal} is measured. For our measurements we

have used, a echo absorbing material (ECCOSORB) as hot load. This provides a load at ambient temperature (300K). For the cold load, the same material immersed in liquid Nitrogen was used.

Assuming that the receiver is working in the linear regime, the receiver output power can be plotted as a function of load temperature and a straight line connecting the points (T_h, P_h) and (T_c, P_c) can be obtained as shown in Figure 3.1. The equation of the straight line fitted to the data can be given as:

$$P = mT + C \tag{3.1}$$

where m = $\frac{P_h - P_c}{T_h - T_c}$ and C is the intercept on the power axis.
Using Eq. 3.1 and assuming that, $T_{c+cal} = T_c + T_{cal}$, the T_{cal} value can be calculated as:

$$T_{cal} = \frac{P_{c+cal} - P_c}{m} \tag{3.2}$$

and the noise temperature of the receiver can be given as:

$$T_{rx} = |\frac{C}{m}| \tag{3.3}$$

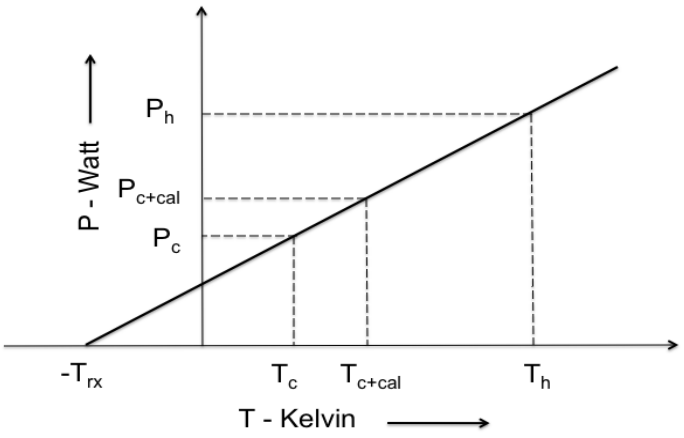

Figure 3.1: A graphical representation of the Y-factor method. The output power is plotted for hot and cold loads and a straight line connects the points (T_h, P_h) and (T_c, P_c).

3.1.1 Frequency dependance of T_{cal}

An instantaneous bandwidth of 2 GHz is available for the MF receiver measurements. The MF receiver response varies with frequency in the 18-26.5 GHz operational range

and also within each 2 GHz band due to the bandshape. As a consequence T_{cal} values varies as a function of frequency and bandwidth. The two major factors responsible for the variation are:

- The directional coupler does not couple the same amount of power generated by the noise generator into the receiver as the frequency changes.
- The bandshape decreases as the frequency increases; and therefore response of the receiver to noise power injected may not be constant as a function of frequency.

3.2 Methodology adopted to manage the T_{cal} values for MF receiver

As mentioned earlier, the T_{cal} depends on frequency and bandwidth. It is therefore necessary to determine this parameter properly to get precise measurements of system temperature when using a wide bandwidth receiver. The laboratory measurements to obtain the T_{cal} for the MF receiver were performed in steps of 400 MHz for each feed and polarization. In total 20×14 measurements were performed[1]. Figure 3.2 shows the T_{cal} measured as a function of frequency for the central feed of the MF receiver. It can be noticed that in order to get a precise value of T_{cal}, the 400 MHz sampling is not sufficient. Therefore a mathematical approach was developed (Orfei et al., 2008) using the laboratory measurements as reference values.

3.2.1 The method

The measured output power (P_h, P_c, P_{c+cal}) can be written as:

$$P_h = \int_{f_1}^{f_2} k_B * T_h * G(f) df \tag{3.4}$$

$$P_c = \int_{f_1}^{f_2} k_B * T_c * G(f) df \tag{3.5}$$

$$P_{c+cal} = \int_{f_1}^{f_2} k_B * (T_c + T_{cal}) * G(f) df \tag{3.6}$$

where k_B is Boltzmann constant and $G(f)$ is the receiver gain.

[1] I have participated in the measurements when the system was dismounted after the pilot survey (see Chapter 5).

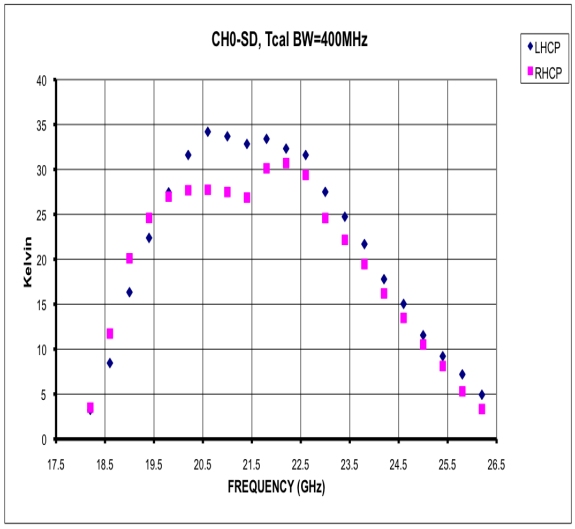

Figure 3.2: T_{cal} as a function of frequency for central feed of the MF receiver. Blue and pink symbols show the T_{cal} values for LCP and RCP respectively. X-axis presents the frequency (GHz). Y-axis represents the T_{cal} value (K).

The T_{cal} value as a function of frequency can be obtained by substituting Eq. 3.4, Eq. 3.5 and 3.6 in Eq. 3.2:

$$T_{cal}(f) = \frac{\int_{f_1}^{f_2}(T_m(f) * G(f)df)}{\int_{f_1}^{f_2}(G(f)df)} \tag{3.7}$$

where $T_m(f)$ is the polynomial fitted to T_{cal} values obtained from the laboratory measurements between frequencies f_1 and f_2. Since the transfer function $G(f)$ for each feed and polarization is not available for the MF receiver, a spectrum analyzer was used to get this information with a high sampling rate (5 MHz). This gives the bandshape for each 2 GHz wide bands. Figure 3.3 shows the bandshape measured in the laboratory over the full 18-26.5 GHz range in windows of 2 GHz for the central feed of the MF receiver.

Since for our method, the bandshape is the important parameter rather than the gain G(f) absolute values, Eq. 3.7 can be rewritten as:

$$T_{cal}(f) = \frac{\int_{f_1}^{f_2}(T_m(f) * g(f)df)}{\int_{f_1}^{f_2}(g(f)df)} \tag{3.8}$$

where $g(f) = \frac{G(f)}{G(100)}$ is the relative gain (or bandshape), normalized to the gain at 100 MHz.

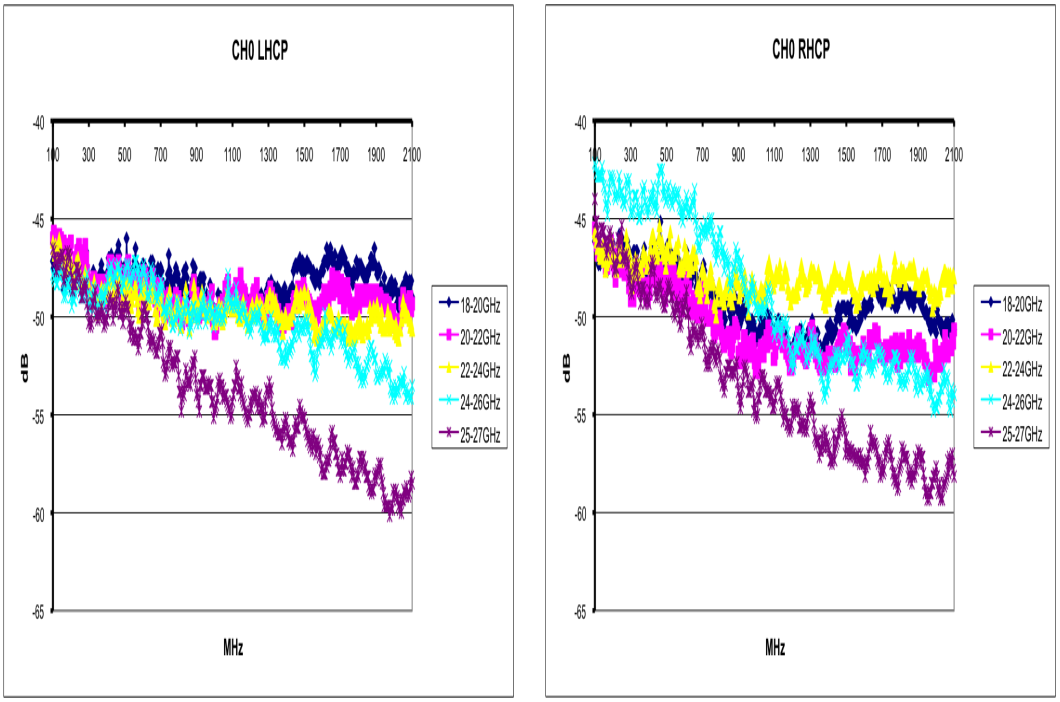

Figure 3.3: Laboratory measurement for the bandshape in steps of 5 MHz for the central feed of the MF receiver. Left: Left Circular Polarization. Right: Right Circular Polarization.

3.3 Results

A best-fit 4^{th} order polynomials were obtained for the bandshape $g(f)$. Figure 3.4 (left plot) shows the polynomial fitted to the bandshape in the frequency band 18 - 20 GHz. In parallel T_{cal} laboratory data (see Figure 3.2) were fitted using a cubic spline within the same 2 GHz bandwidths. The T_{cal} values weighted by the bandshape were obtained as $\mathrm{T}_m(f) * g(f)$ where T_m(f) and $g(f)$ are the values obtained through best fitting. Finally a best-fit polynomial was used to fit the weighted T_{cal} values $[T_m(f) * g(f)]$ shown as in Figure 3.4 (right plot).

Following the same strategy, $g(f)$ and weighted T_{cal} values for the entire 18-26.5 GHz band can be calculated for each 2 GHz band, each feed and polarization. Results for the central feed (LCP only) are shown in Figures 3.4 - 3.8. Figure 3.9 summarizes the weighted T_{cal} values as a function of frequency for the entire 18-26.5 GHz range. It is worth noting that the interpolated values are in very good agreement with the ones measured in the laboratory in 400 MHz steps.

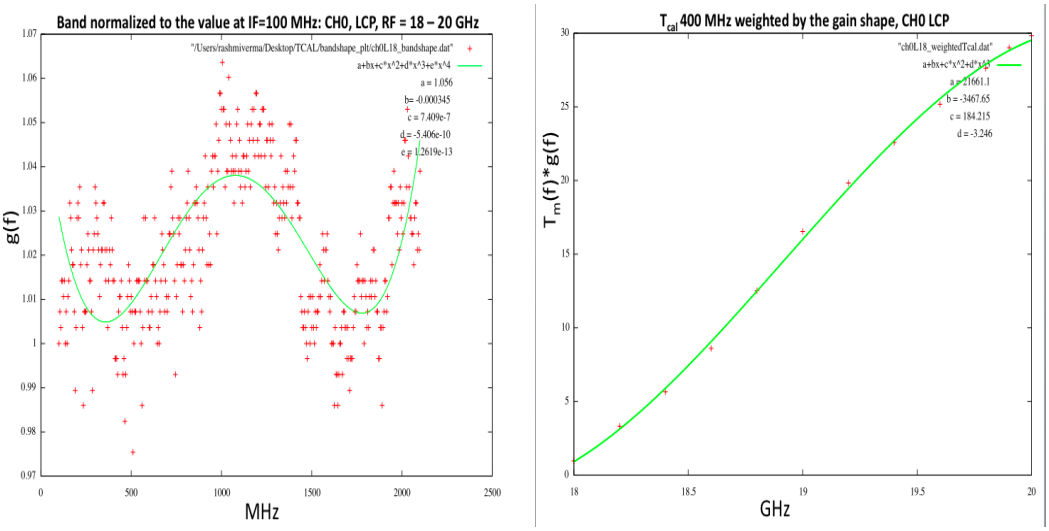

Figure 3.4: Band shape normalized to the value at IF=100 MHz in the band 18 - 20 GHz (left); weighted T_{cal} as a function of frequency (right) for the central feed for Left Circular Polarization.

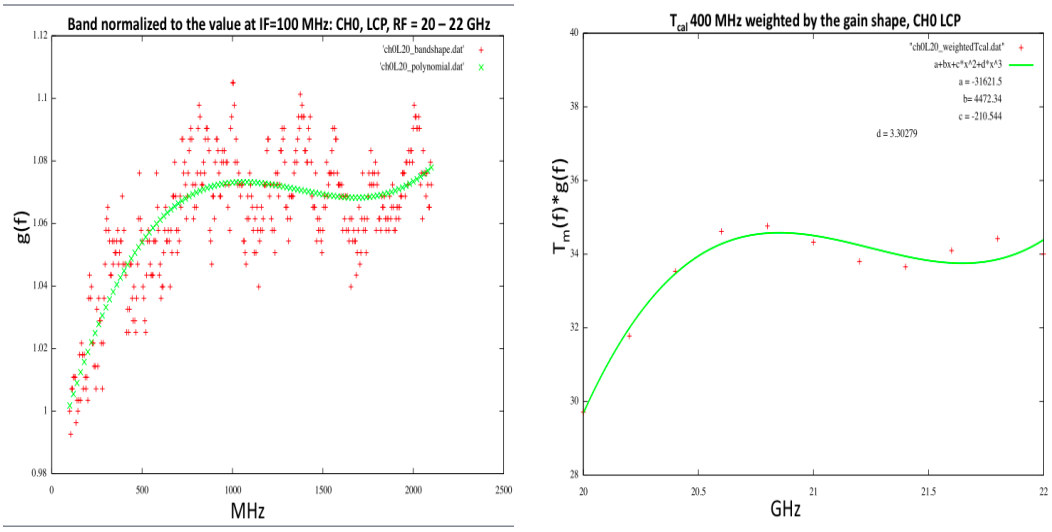

Figure 3.5: Band shape normalized to the value at IF=100 MHz in the band 20 - 22 GHz (left); weighted T_{cal} as a function of frequency (right) for the central feed for Left Circular Polarization.

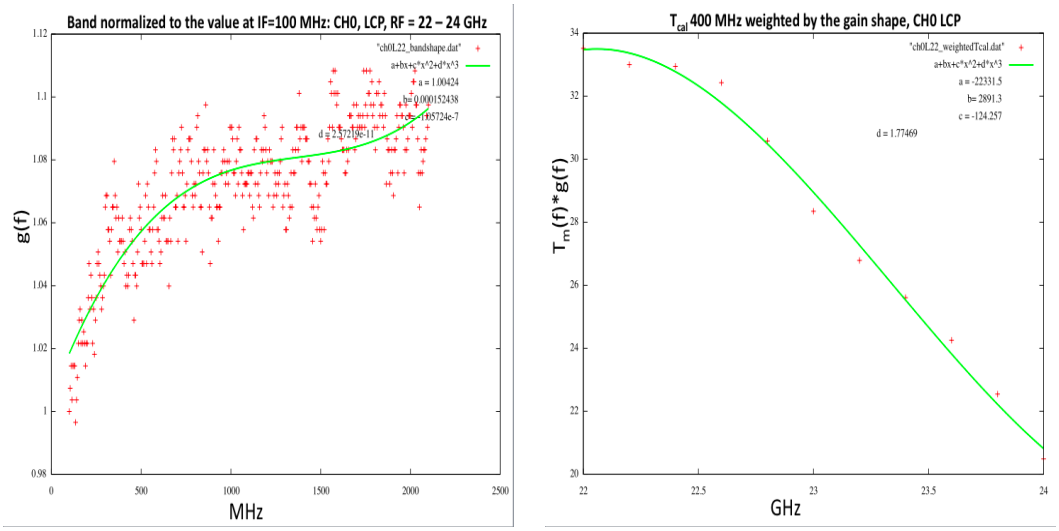

Figure 3.6: Band shape normalized to the value at IF=100 MHz in the band 22 - 24 GHz (left); weighted T_{cal} as a function of frequency (right) for the central feed for Left Circular Polarization.

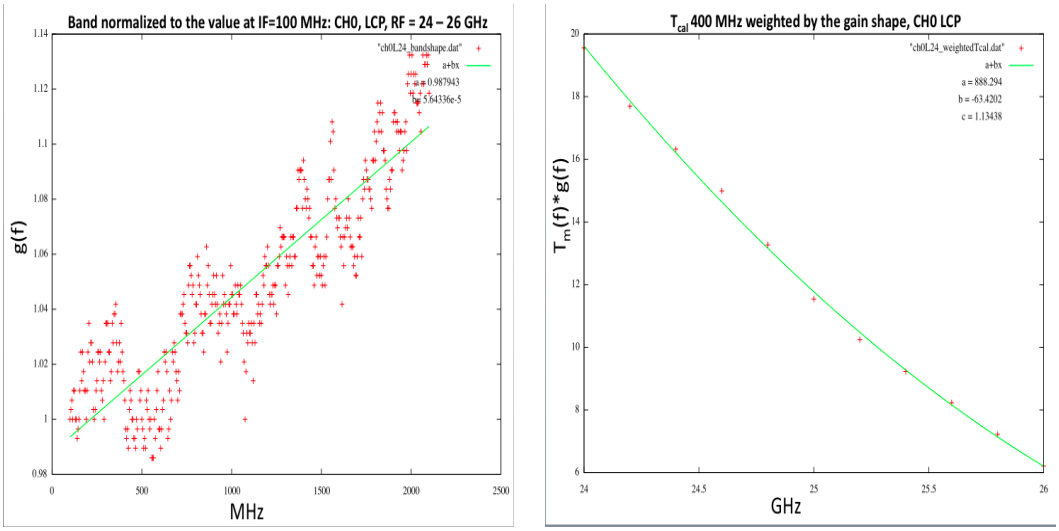

Figure 3.7: Band shape normalized to the value at IF=100 MHz in the band 24 - 26 GHz (Left); weighted T_{cal} as a function of frequency (Right) for the central feed for Left Circular Polarization.

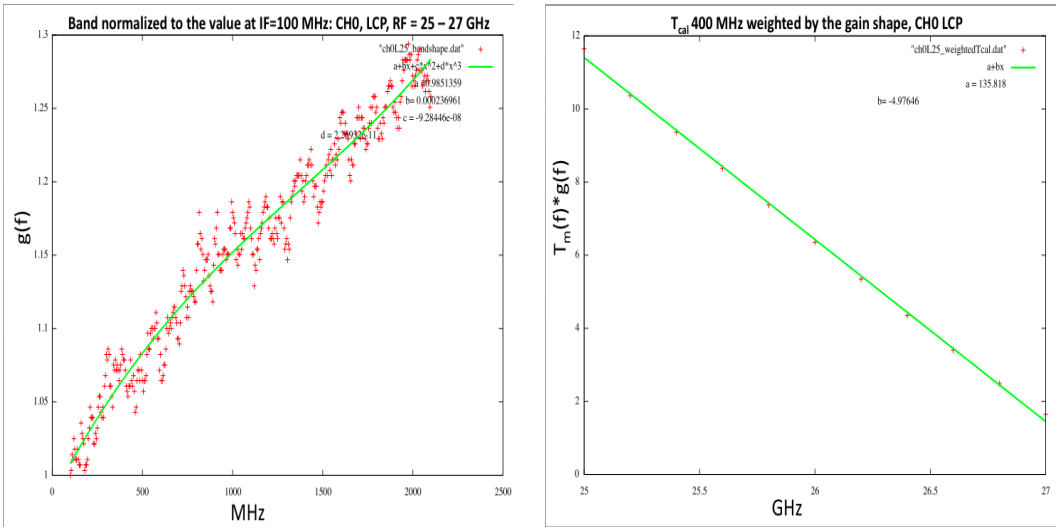

Figure 3.8: Band shape normalized to the value at IF=100 MHz in the band 25 - 27 GHz (Left); weighted T_{cal} as a function of frequency (Right) for the central feed for Left Circular Polarization. In this case the laboratory measurements are available only upto the frequency 26.4 GHz. Therefore the values in the plot for frequencies higher than 26.2 GHz are irrelevant.

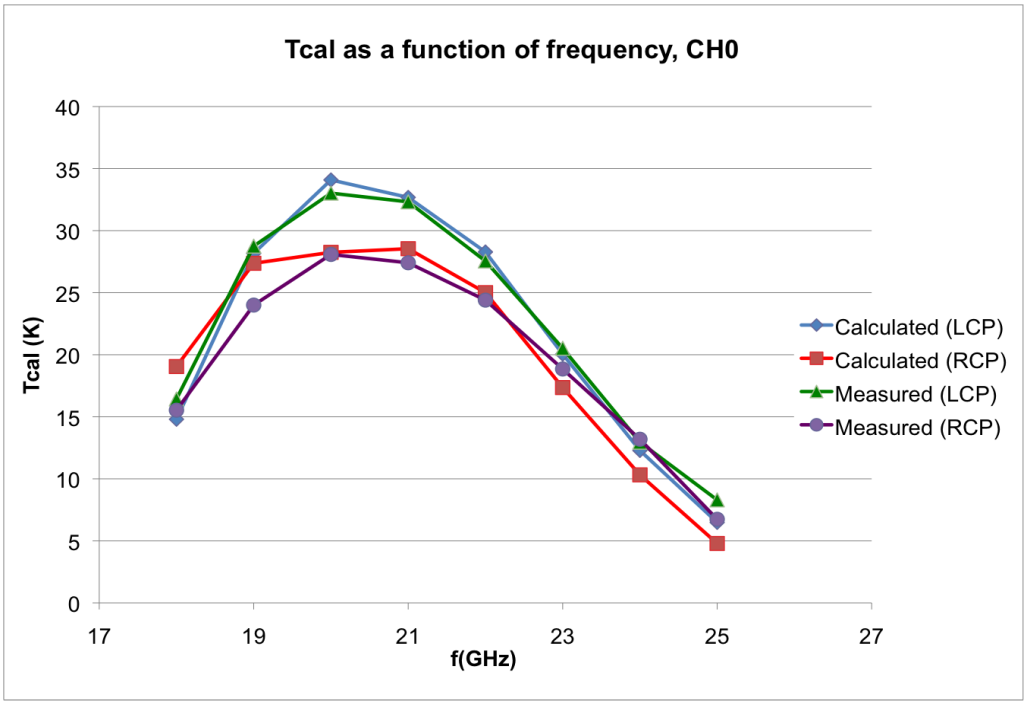

Figure 3.9: T_{cal} as a function of frequency for the central feed of the MF receiver. Green and violet symbols show the laboratory measurements. Blue and red symbols show the T_{cal} values obtained using the mathematical approach. X-axis presents the frequency (GHz). Y-axis represents the T_{cal} value (K).

3.4 Conclusions

This chapter has described the mathematical approach developed to calculate T_{cal} values in any desired 2 GHz observing frequency band (f_1, f_2) taking into account the bandshape. This approach is very useful for large bandwidth and multi-feed receivers as the MF receiver, as getting laboratory measurements at very high frequency sampling is too time consuming. Our interpolation method proved to be successful, being able to reproduce the 400 MHz-step T_{cal} laboratory measurements within 5-10% accuracy. The polynomials describing T_{cal} as a function of frequency for each feed and polarization can be implemented in the antenna acquisition software together with a known noise source to provide accurate T_{cal} estimates to telescope users. At the time of writing, it is not implemented in the new Medicina acquisition software (ESCS).

Chapter 4

Calibration Campaign at 21 GHz with MF Receiver

Chapter 2 discussed the K-band multi-feed receiver and the system characterization as obtained using the VLBI acquisition system with a bandwidth of 400 MHz (Mark 4). This chapter I will describe the calibration campaign carried out at 21 GHz using the MF receiver coupled with the new total power analogue backend at the Medicina 32-m dish. This chapter will cover all the steps required for pointing and amplitude calibration for the MF receiver. The calibration campaign including the criteria used for target selection and a description of the observing system will be discussed in Section 4.1. In Section 4.2 I will describe all the steps performed to quantify the pointing error of the MF receiver. Section 4.3 will present results of flux density variations analysis of the selected calibrators and in Section 4.4 I will explain the strategy adopted to calibrate the MF fluxes.

4.1 Calibration Campaign

The calibration is a well understood process for single dish antennas and it compensates for imperfections and unknowns in the instrument use, including antenna-defects, pointing errors, atmospheric absorption and fluctuations, receiver and backend gain instabilities, etc. In order to understand pointing corrections, electronic gain and antenna parameters (including the antenna beam) as a functions of observing frequency and elevation it is necessary to perform 'ad hoc' calibration observations.

4.1.1 Motivation

The goals of this calibration campaign are many fold:

(1) to quantify pointing offsets for the MF receiver.

(2) to build up a pointing and flux calibrator list for Medicina 32-m telescope to be used for K-band observations and in particular for the commissioning pilot survey at 21 GHz (see Chapter 5).

(3) to develop a methodology to calibrate the MF receiver data since the noise diode is not yet implemented in the new antenna control system (ESCS).

4.1.2 Observing system

The first phase of the commissioning of the MF receiver was carried out at the Medicina 32-m dish using the VLBI acquisition system Mark 4 with 400 MHz of bandwidth in 2008 (see Chapter 2). Since the total power analogue backend and the new antenna control system ESCS (Enhanced Single-dish Control System, see Righini, S., PhD thesis, 2010) were both under development, we coupled them with the Medicina 32-m telescope to test the entire system. A calibration campaign was launched in September 2009 to check the pointing of the receiver and to provide a method for flux calibration. Eight bright radio sources were observed during this campaign.

4.1.3 Target selection

We have selected 8 bright calibrators. Most of these sources belong to the calibrator list of Baars et al.(1977) except sources 3C84, 3C273 and 1611+343. The selected sources have the following characteristics:

(1) flux density greater than 1.0 Jy at 21 GHz.

(2) angular size less than 100 arcsec, the FWHM of the Medicina antenna beam at 21 GHz.

(3) no intraday flux variation.

(4) a power law radio spectrum.

Source 3C84, 3C273, 1611+343 are known variables on long time scales but, as they are very bright at 21 GHz, they have been included for pointing calibration purposes and to measure their flux densities close in time to the planned pilot survey in order to use them for amplitude calibration. Table 4.1 reports the source positions and the flux densities (in Jy) at two frequencies in K-band. The expected flux densities at 21 GHz are calculated using different methods. For sources from Baars et al. (1977) flux densities are calculated using the spectra provided by Baars et al., 1977, where flux density (S) can be represented as a function of frequency (ν) given by:

$$logS[Jy] = a + b * log\nu[MHz] + c * log^2\nu[MHz] \tag{4.1}$$

where a, b, c are the spectral coefficients applicable in a certain frequency range. The flux densities for each source are calculated using the Ott et al. (1994) spectral coefficients.

In case of DR21 spectral coefficients were not available from Ott et al. (1994); therefore we have used the old spectral coefficients from Baars et al. (1977). For sources that do not belong to the Baars et al. (1977) calibrator list, flux densities at 21 GHz are obtained using a linear interpolation between 10 GHz and 23 GHz measurements (Peng et al., 2000). The WMAP (23 GHz) flux densities reported in the table refer to the average values over the seven epochs taken from the WMAP seven-year source catalog (Gold et al. 2011). An analysis of the source variability is performed in Section 4.3 by using the fluxes from each year of the WMAP catalog.

4.1.4 Observations

K-band observations were carried out on September 27^{th} & 28^{th}, 2009 in the frequency band 20-22 GHz (central frequency 21 GHz) using the central feed of the MF receiver (see Chapter 2). Each source was measured using cross-scan observations, where the scan was first performed in right ascension and then in declination. Each source was observed at different elevations through multiple cross scans. In total 178 cross-scans were performed. The data were acquired through the total power analog backend with a sample rate of 40 ms. Since the receiver and the backend, together with the new antenna control system (ESCS) were undergoing commissioning, we have performed the cross-scans moving the antenna at different speeds, in order to check whether the antenna speed can induce different offsets

Table 4.1: Flux density of the selected sources at two frequencies in K-band; col.(1) gives the extensively known name of the source, mostly 3C (Third Cambridge Radio Catalogue) source name; col.(2) and col.(3) give the source position coordinates: right ascension and declination in equatorial coordinate system; col.(4) gives the average flux density of the sources at 23 GHz taken from the WMAP seven-year catalog; col.(5) gives the expected flux density at 21 GHz.

Source Name	RA (hhmmss.s)	Dec (ddmmss)	S_{WMAP}(Jy)	S_{21GHz}(Jy)
3C48[a]	01 37 41.3	+33 09 35	0.9±0.06	1.29
3C84[b]	03 19 48.1	+41 30 42	12.2±0.05	17.56
3C147[a],[d]	05 42 36.1	+49 51 07	1.8±0.05	1.88
3C273[b]	12 29 06.7	+02 03 09	22.7±0.05	34.26
3C286[a]	13 31 08.3	+30 30 33	2.3±0.05	2.56
3C295[a]	14 11 20.6	+52 12 09	1.0±0.04	1.01
1611+343[b]	16 13 41.0	+34 12 48	3.9±0.04	4.32
DR21[c]	20 37 14.0	+42 29 46	-	19.17
NGC 7027[a]	21 07 01.7	+42 14 11	-	5.53

[a] Flux density is calculated using the spectral coefficients from Ott et al.(1994) measurements.
[b] Flux density is calculated using linear interpolation between 10 GHz and 23 GHz measurements (Peng et al., 2000).
[c] Flux density is calculated using the spectral coefficients from Baars et al.(1977) measurements.
[d] This source is listed here as has been used during the pilot survey (for more details, see Chapter 5) but was not part of the calibration campaign.

in the antenna position parameters (both in right ascension and declination). In particular two different antenna speeds, 3°/minute and 1.5°/minute were exploited.

4.1.5 Data flagging

As a preliminary step of the data reduction, scans which were badly affected by the adverse weather conditions were manually removed. As a result of data flagging 12% of the RA scans and 17% of Dec scans were discarded.

4.1.6 Data reduction

The data reduction consists of two main steps to be performed for each scan: baseline subtraction and source fitting. A 1^{st} order polynomial is used for baseline subtraction and a six parameter non-linear least square fit, involving a Gaussian and a 2^{nd} order polynomial background was performed. The function fitted after the baseline removal is:

$$f(x) = A_0 \exp(-\frac{z^2}{2}) + B_1 + B_2 x + B_3 x^2 \tag{4.2}$$

where

$$z = \frac{x - A_1}{A_2} \tag{4.3}$$

Where A_0 is the amplitude of the Gaussian peak, A_1 is the position at which the peak of the Gaussian fit occurs, A_2 represents the width of the Gaussian (standard deviation, σ). B_1, B_2 and B_3 represent the constant, linear and quadratic terms of the 2^{nd} order polynomial respectively.

Figure 4.1 illustrates the reduction procedure for a scan performed in RA direction. In the top diagram the raw data is shown where a prominent non-flat baseline is clearly visible. In the bottom diagram the result of the Gaussian fitting performed with a 2^{nd} order polynomial background, after baseline subtraction is shown.

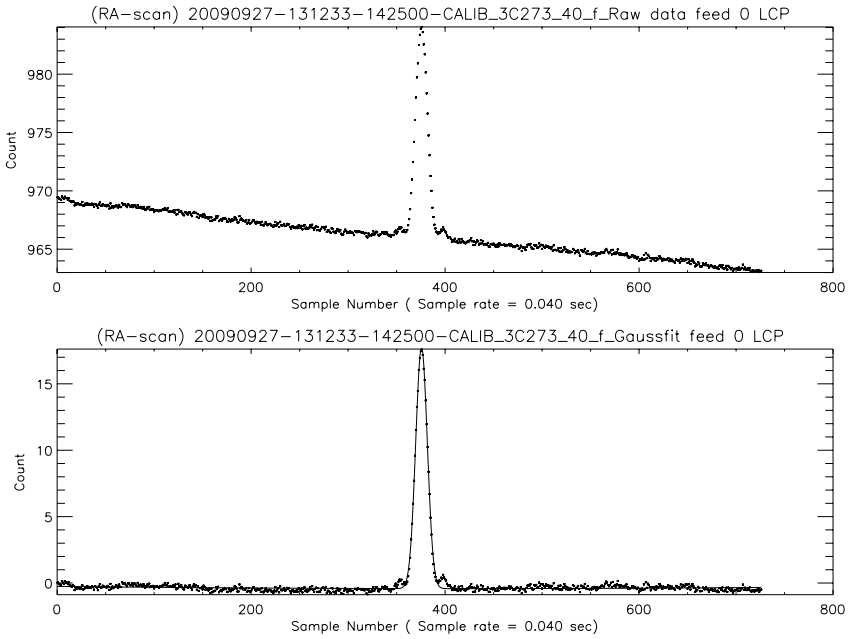

Figure 4.1: Scan across source 3C273 at an elevation of 40° with the central feed for left circular polarization. Top: Raw data, Bottom: Gaussian fit with a 2^{nd} order polynomial background, after baseline subtraction. X-axis represents the sample number (sample rate is 40 ms); Y-axis represents the signal in an arbitrary unit referred to as Count.

4.2 Pointing Calibration

Pointing calibration plays an important role in astronomy. In order to measure precise source flux densities, antenna should properly point at the source. The pointing accuracy of a radio-telescope at any observatory is generally checked by

using standard radio flux density calibrators.

4.2.1 Antenna parameters & pointing offsets measured from Gaussian fitting

In order to check the pointing of the receiver in both right ascension and declination direction, RA and Dec scans were analysed separately. The fitting function given in Eq. 4.2 was applied to each RA and Dec scan. Source positions (RA and Dec) and antenna beam size (FWHM) are measured from the Gaussian fit. The expected FWHM of antenna beam is ≈ 100 arcsec at 21 GHz. The distribution of the measured values of the FWHM of the antenna beam in both RA and Dec directions for all the observed sources is shown in Figures 4.2a and 4.2b. The distribution of the differences between the source RA and Dec (commanded) values used to point the telescope (taken from literature, see Table 4.1) and the ones measured through the source Gaussian fits are shown in Figures 4.3a and 4.3b.

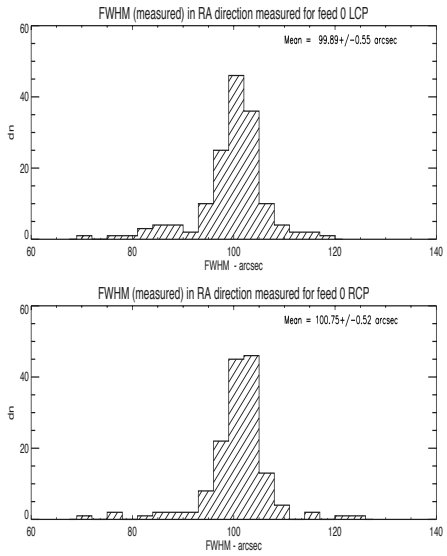

(a) Histogram of the FWHM of the telescope beam (expected ≈ 100 arcsec) measured from the Gaussian fit in right ascension direction. Top: Left circular polarization; Bottom: Right circular polarization.

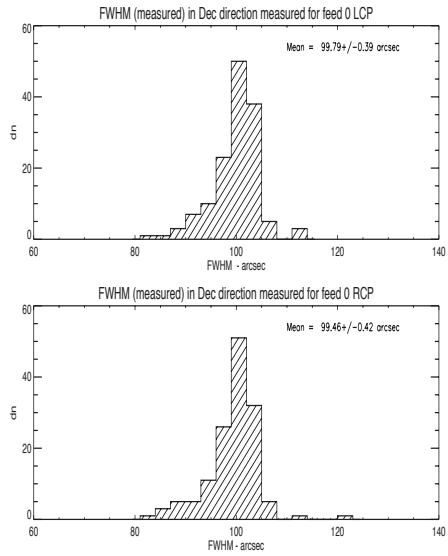

(b) Histogram of the FWHM of the telescope beam (expected ≈ 100 arcsec) measured from the Gaussian fit in declination direction. Top: Left circular polarization; Bottom: Right circular polarization.

Figure 4.2: Histogram of the FWHM of the telescope beam (expected ≈100 arcsec).

The mean FWHM of the antenna beam in both directions and the difference

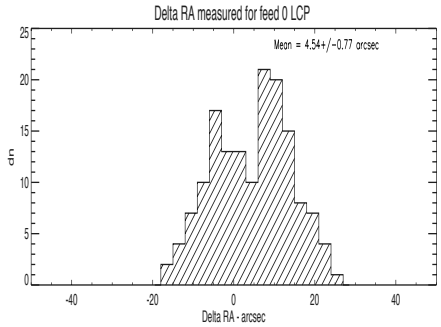

(a) Histogram of the difference between the RA taken from the literature and the one measured from the Gaussian fit in units of arcsec. Top: Left circular polarization; Bottom: Right circular polarization.

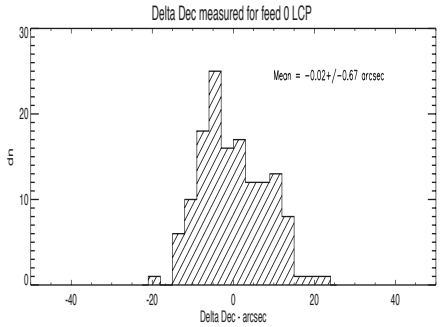

(b) Histogram of the difference between the Dec taken from the literature and the one measured from the Gaussian fit in units of arcsec. Top: Left circular polarization; Bottom: Right circular polarization.

Figure 4.3: Histogram of the difference between the nominal coordinates of the source and the one measured through Gaussian fitting.

between the commanded and the measured values of RA and Dec are listed in Table 4.2. In order to investigate any possible correlation between antenna speed

Table 4.2: Antenna position parameters obtained through Gaussian fitting; col.(1) gives the name of the antenna parameter; col.(2) & col.(3) give the mean values for each parameter for the left circular polarization and right circular polarization.

Parameter	Feed 0 LCP Mean value (arcsec)	Feed 0 RCP Mean value (arcsec)
FWHM (RA)	99.89±0.55	100.75±0.52
FWHM (Dec)	99.79±0.39	99.46±0.42
Delta RA	4.54±0.77	4.62±0.81
Delta Dec	-0.02±0.67	0.45±0.65

and pointing accuracy of the telescope this analysis was repeated after dividing RA and Dec scans in two groups: one with scans performed with an antenna speed of 3.0°/minute and the second one with antenna speed of 1.5°/minute. The number of scans performed in right ascension direction at the speed of 1.5°/minute and 3.0°/minute are 77 and 75 respectively. The number of scans performed in declination direction at the speed of 1.5°/minute and 3.0°/minute are 73 and 68 respectively. The results are plotted in Appendix A and summarized in Table 4.3. No significant trend with antenna speed was found. The mean difference in the antenna position parameters and FWHM of antenna beam at 1.5°/minute and 3°/minute are consistent within the error, with the an exception of Delta RA and Delta Dec for LCP where 3°/minute measurements show a larger offset. However this trend is not confirmed for RCP.

Table 4.3: Antenna position parameters obtained through Gaussian fitting for the scans obtained with different antenna speeds; col.(1) gives the name of the antenna parameter; col.(2) & col.(3) give the mean value for the measured parameter for the left circular polarization for antenna speed of 1.5°/minute & 3.0°/minute respectively; col.(4) & col.(5) give the mean value for the measured parameters for the right circular polarization for antenna speed of 1.5°/minute & 3.0°/minute respectively.

Parameter	LCP mean (arcsec)		RCP mean (arcsec)	
	1.5°/minute	3.0°/minute	1.5°/minute	3.0°/minute
FWHM (RA)	99.89±0.88	99.90±0.64	100.49±0.81	101.03±0.66
FWHM (Dec)	99.26±0.57	100.36±0.52	99.11±0.53	99.84±0.66
Delta RA	3.09±1.02	6.19±1.14	3.53±1.11	5.81±1.15
Delta Dec	-0.47±0.91	5.84±0.52	-0.07±0.94	1.00±0.89

It is also important to check whether pointing is stable with elevation. Measurements were therefore analysed separately for each source. All the scans of the eight sources at each elevation were averaged together and the overall dependence of Delta RA and Delta Dec on elevation is shown in Figures 4.4a and 4.4b respectively. The pointing results to be rather stable for all elevations $\geq 40°$. At low elevations $\leq 30°$ offsets are of the same order of magnitude but measurements seem to be uncorrelated to the ones obtained at higher elevations.

Finally the FWHM of antenna beam and the offsets in RA & Dec were measured for each source separately. The results for two sources, 3C48 and 3C286, are presented here as they were used as calibrators during the planned pilot survey at 21 GHz (see Chapter 5). The total number of scans performed for source 3C48 and

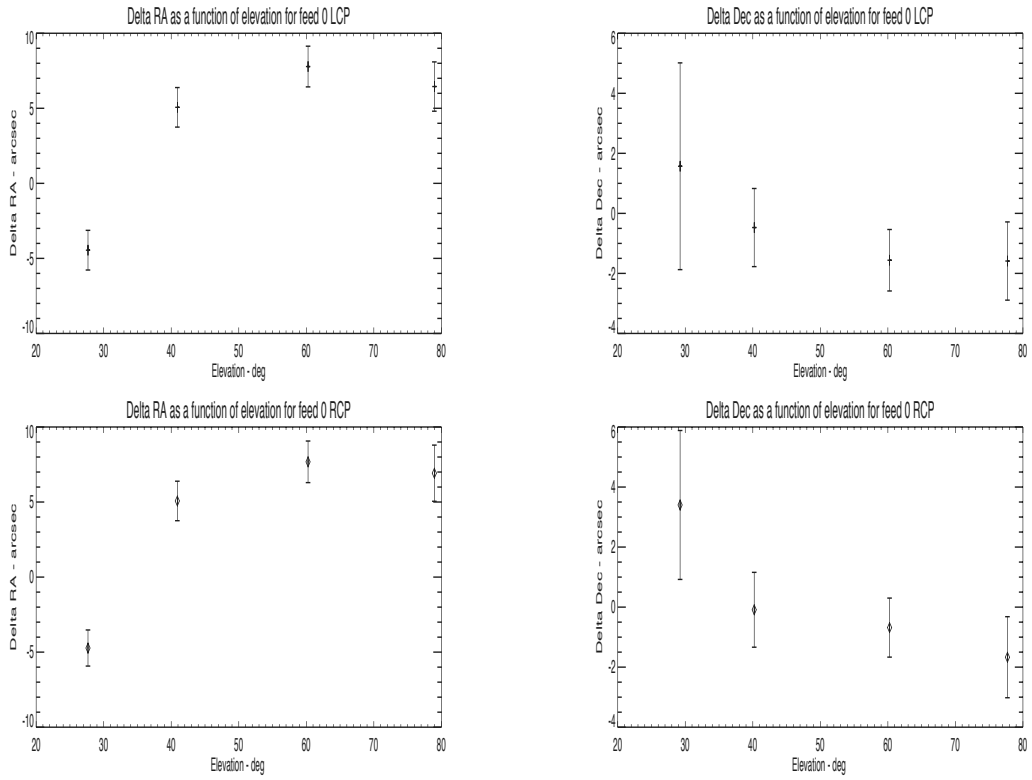

(a) Delta RA (arcsec) versus elevation(degree). Top: Left circular polarization; Bottom: Right circular polarization.

(b) Delta Dec (arcsec) versus elevation (degree). Top: Left circular polarization; Bottom: Right circular polarization.

Figure 4.4: Delta RA and Delta Dec as a function of elevation.

3C286 are 16 and 58 respectively (37% of 3C48 scans and 23% of 3C286 scans were discarded due to the adverse effect of weather). The results are plotted in Appendix B and listed in Table 4.4 (3C48) and Table 4.5 (3C286). It is also important to mention that both sources 3C48 and 3C286 are among the weakest sources in Table 4.1.

Table 4.4: Antenna position parameters obtained through Gaussian fitting for source 3C48; col.(1) gives the name of the antenna parameter; col.(2) & col.(3) give the mean value for each parameter for the left circular polarization and right circular polarization respectively.

Parameter	Feed 0 LCP Mean value (arcsec)	Feed 0 RCP Mean value (arcsec)
FWHM (RA)	93.90±2.06	99.40±1.76
FWHM (Dec)	98.08±1.76	96.22±1.76
Delta RA	7.62±2.37	7.74±2.31
Delta Dec	0.79±1.18	3.32±2.16

Table 4.5: Antenna position parameters obtained through Gaussian fitting for source 3C286; col.(1) gives the name of the antenna parameter; col.(2) & col.(3) give the mean value for each parameter for the left circular polarization and right circular polarization respectively.

Parameter	Feed 0 LCP Mean value (arcsec)	Feed 0 RCP Mean value (arcsec)
FWHM (RA)	101.33±1.64	102.56±1.25
FWHM (Dec)	97.65±1.61	97.48±1.19
Delta RA	6.95±1.54	5.64±1.55
Delta Dec	3.19±1.91	2.33±1.88

In conclusion, the pointing accuracy is of the order of few arcsec independent of source, antenna speed and elevation.

4.3 Flux Variability Analysis

Before discussing the methodology adopted to carry out the source amplitude calibration, an analysis to investigate the flux temporal variability of the selected sources was carried out. The variability analysis is presented for six sources (out of the eight selected sources) which are present in the WMAP seven-year source catalog (Gold et al. 2011). The flux density variation over the seven epochs of the WMAP measurements was invesigated. Multi-epoch flux density measurements for sources 3C286, 3C295, 3C48, 3C84, 3C273 and 1611+343 are shown in Figures 4.5 and 4.6. Symbols refer to the WMAP measurements over the seven epochs while dotted lines represent the expected flux density at 23 GHz calculated using Eq. 4.1 with spectral coefficients from Ott et al. (1994). The same variability analysis was performed for source 3C147 (see Figure 4.7) even if it was not the part of the calibration campaign targets. The source was used as a calibrator for the pilot survey (see Chapter 5).

A Chi-square test was performed on the WMAP seven-year dataset to check for variability, with $\chi^2 = \sum(\frac{S_i - \bar{S}}{\sigma_i^2})^2$ (Fanti et al. 1981, Peng et al. 2000), where S_i and σ_i are the measured flux and estimated error for the i-th epoch and $\bar{S}$ is the mean flux as measured from all the epochs. The χ^2 analysis is a powerful tool to check the variability but it does not quantify the degree of variability. The degree of variability was calculated by measuring the so called modulation index, quoted as $m[\%] = 100 \times (\frac{\sigma_S}{\bar{S}})$ (Peng et al. 2000) only for the sources found to be variable. The results are presented in Table 4.6. Sources 3C48 and 3C286 do not show significant variability with variability probabilities of the order of 25%, while the case of 3C295 is less clear with a probability of being variable of the order of 50%. Although it shows 50% probability of being variable, it is worth mentioning that source 3C295 together with sources 3C48 and 3C286, are considered as reliable calibrators and vastly used as primary calibrators. Sources 3C84, 3C147, 3C273 and 1611+343 are known to be variable on long time scales. The variability of these sources was investigated since they were planned to be used as secondary calibrators (bootstrapping) for the pilot survey (see Chapter 5). The degree of variability for these sources is measured to be of the order of 4-18 %.

Table 4.6: Variability for the sources at 23 GHz; col.(1) gives the source name; col.(2) gives the probability of the source to be variable; col.(3) gives the probability that the source is not variable; col.(4) gives the chi square value; col.(5) gives the % modulation index; col.(6) gives the WMAP identification name.

Source	Probability	1 - Probability	χ^2	m [%]	WMAP Identification
3C48	0.25	0.75	3.46	-	J0137+3315
3C286	0.26	0.74	3.55	-	J1331+3031
3C295	0.50	0.50	5.38	8.68	J1411+5215
3C84	1.00	0.00	129.73	4.3	J0319+4131
3C147[a]	0.97	0.03	13.80	10.01	J0542+4951
3C273	1.00	0.00	5522.42	15.4	J1229+0203
1611+343	1.00	0.00	335.26	17.7	J1613+3412

[a] The source is planned to be used during the pilot survey (for more details, see Chapter 5).

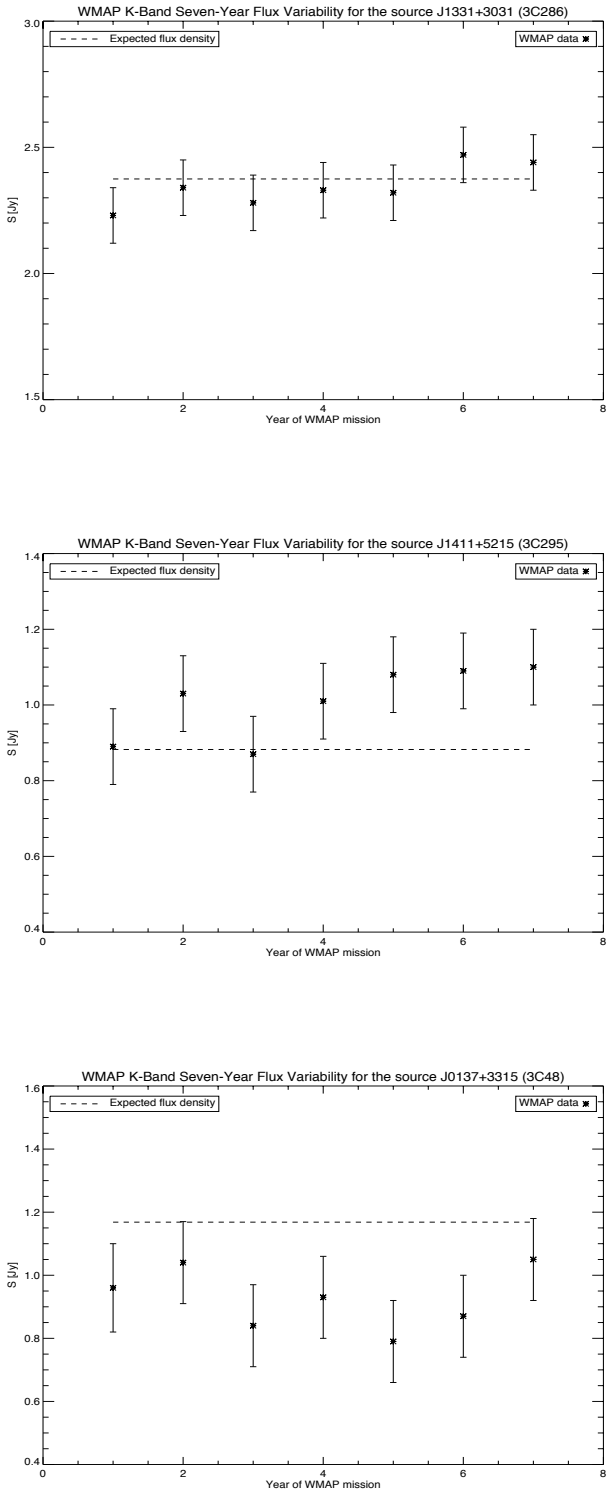

Figure 4.5: Flux density measurements of sources 3C286, 3C295 and 3C48 (top to bottom) at 23 GHz. Data is taken from the WMAP seven-year source catalog (Gold et al. 2011). The dotted line in the figures corresponds to the expected flux densities at 23 GHz calculated using spectral coefficients from Ott et al. (1994).

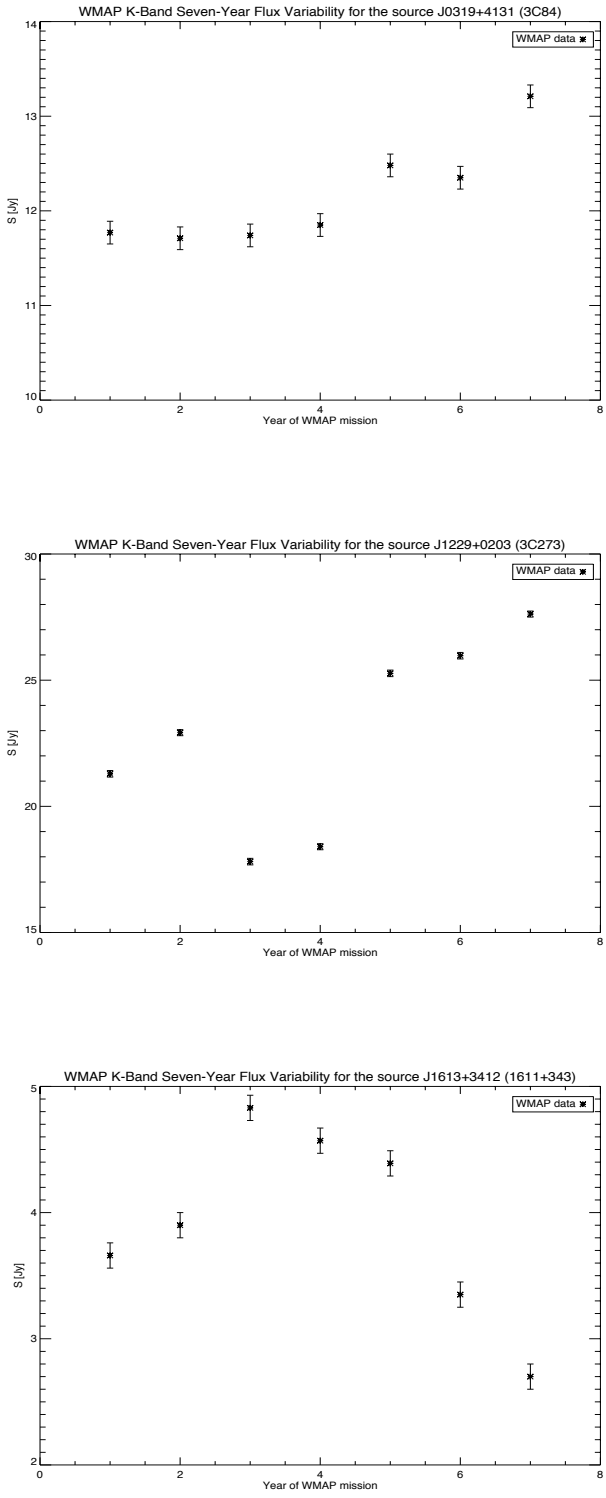

Figure 4.6: Flux density measurements of sources 3C84, 3C273 and 1611+343 (top to bottom) at 23 GHz. Data is taken from the WMAP seven-year source catalog (Gold et al. 2011). These sources are known to be variable therefore no spectral coefficients are available for these sources.

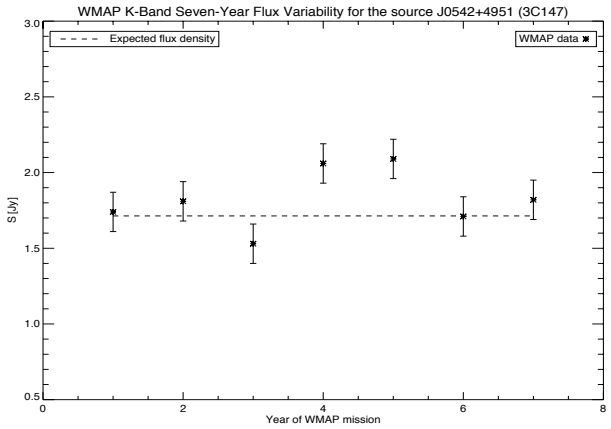

Figure 4.7: Flux density measurements of sources 3C147. The source was used during the pilot survey. Data is taken from the WMAP seven-year source catalog (Gold et al. 2011). The dotted line in the figures corresponds to the expected flux density at 23 GHz calculated using spectral coefficients from Ott et al. (1994).

4.4 Amplitude Calibration

The goal of conventional amplitude calibration is to convert the backend output unit (count or voltage) into a physical quantity (flux density or brightness temperature) by carefully tracking instrumental imperfection and atmosphere effects and to determine accurate conversion factors using 'known' astronomical standards. This becomes very difficult at centimeter wavelengths due to the temporal variability of earth's atmosphere and lack of bright and stable flux density calibrators. Amplitude calibration mainly consists of four steps: (1) accurate total power measurement; (2) calibration of telescope-dependent amplitude scale; (3) calculation of the correction factor to compensate for atmospheric absorption; (4) conversion of telescope, time and position dependent amplitude scale into astronomical standards.

4.4.1 Accurate total power measurement

The flux densities of selected sources in an arbitrary backend unit (counts) were retrieved from the Gaussian fitting given in Eq. 4.2. The fitting procedure is shown in Figure 4.1. As each source was observed at different elevations with multiple cross-scans, flux densities of the sources are obtained after averaging scans at the same elevation. Diagrams of the amplitude as a function of elevation for each source are reported in Appendix C. The plots show amplitude either before or after correcting

for atmospheric absorption (see Subsection 4.4.3).

4.4.2 Calibration of telescope dependent amplitude

The calibration of the telescope-dependent amplitude necessary to check the receiver electronic gain variation with time is achieved through the measurement of a noise source. At centimeter wavelengths it is accomplished using a waveguide oscillator or a noise diode that emits a broadband noise source into the radio receiver and whose value is known in Kelvin. For continuum receivers an appropriate arrangement is to connect the noise source to the antenna terminals through a directional coupler of accurately known coupling. Thus the calibration can be performed without disturbing the receiver. Since the MF receiver and the antenna control software (ESCS) both are under commissioning, the noise source is not yet implemented in the antenna control unit, but the electronic gain variation of the MF receiver over time can be traced by plotting the source amplitude as a function of time. Figure 4.8 shows the variation of amplitude as a function of time for source 3C48. It can be noticed that the amplitude is pretty constant over time either before or after opacity correction. Slight drifts are present that can be considered negligible.

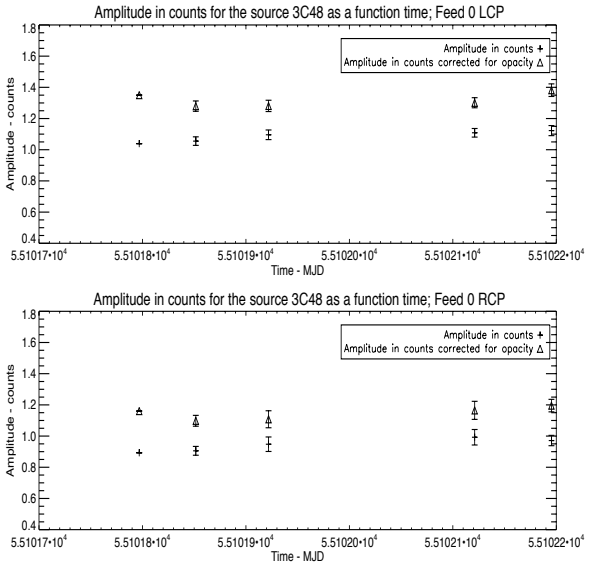

Figure 4.8: Amplitude (in counts) as a function of time (in MJD). Symbols + represent raw amplitude for source 3C48 and Δ represent the amplitude for source 3C48 corrected for opacity.

4.4.3 Atmospheric absorption corrections

Since atmosphere is not transparent at centimeter wavelengths, it is necessary to apply a correction factor to measure the true flux density of the source. During the calibration campaign atmospheric opacity was measured twice a day using the well known skydip procedures (see Subsection 2.7.1). The signal is measured in arbitrary backend unit (counts). In order to estimate the zenith opacity from the T_{sys} measurements undertaken at different elevations, the non-linear polynomial given in Eq. 2.19 is used to fit the skydip data. The following assumptions are made to perform the fitting procedure: (1) $T_0 = 40$ K; (2) an average value of ambient temperature, $T_{atm} = 290$ K; (3) an initial reference conversion factor, [Jy/count] = 1.0 (known to be close to the real value, see section 4.5); (4) telescope gain $\frac{K}{Jy} = 0.1$ (see Chapter 2). Figure 4.9 shows one of the obtained curve describing the system temperature variation as a function of elevation.

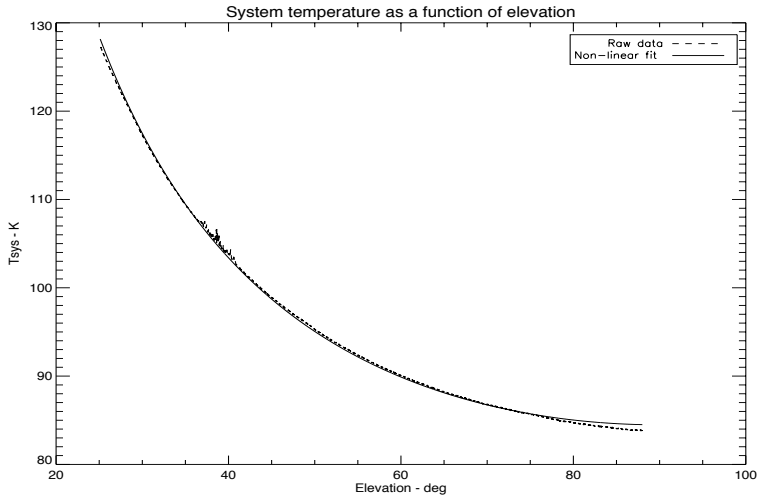

Figure 4.9: System temperature (in Kelvin) as a function of elevation (in degrees). Dashed and solid lines show the raw data and the function used to fit the data respectively.

Zenith opacities obtained after fitting a non-linear polynomial to skydip data are listed in Table 4.7 for each day. A linear interpolation between measurements of each day is used in order to calculate the zenith opacity for each flux measurement. Then zenith opacity corresponding to each measurement was applied to calculate atmosphere attenuation as a function of elevation.

Table 4.7: Zenith opacity obtained from T_{sys} measurement for each day.; col.(1) & col.(2) give Date and UT of the opacity measurements (skydip).; col.(3) gives the zenith opacity obtained from the non-linear fit.

Date	Time (hh:mm)	Zenith opacity
27/09/09	10:00	0.093
27/09/09	23:00	0.140
28/09/09	05:00	0.136
28/09/09	11:00	0.131

4.5 Conversion of Telescope-dependent Amplitude Scale into Astronomical Standards

As mentioned earlier the noise source is not yet implemented in the ESCS; therefore the count to Jansky conversion factor required to calibrate the MF receiver data must be directly obtained by observing standard flux density calibrators. In order to calibrate the MF receiver data an accurate count to Jansky factor [count/Jy] for each source was calculated and a second order polynomial (found to be the best-fit polynomial) was used to fit the data after opacity correction. The [count/Jy] plots for all the sources are shown in Appendix D. The polynomial used to fit the [count/Jy] factors corrected for opacity, versus elevation are listed in Table 4.8. It can be noticed that the [count/Jy] factor obtained for non-variable sources approximately matches with the assumption made in order to fit the skydip data (see Subsection 4.4.3).

In conclusion it is worth to note that:

- The count to Jansky [count/Jy] polynomial retrieved for the non-variable sources 3C48, 3C286 and 3C295 (see Section 4.3) can be used for absolute calibration of the MF receiver data at 21 GHz.
- Source DR21 can be used as a primary calibrator because it is point-like for Medicina telescope at 21 GHz while extended for larger telescopes therefore not suitable for SRT. Also it shows variability at the level of 5-10% (Ott et al., 1994).
- The count to Jansky factor obtained for source NGC7027 can also be used for amplitude calibration at 21 GHz, but the source size and the secular changes of the spectrum should be taken into account (Ott et al., 1994).

Table 4.8: Count to Jansky polynomials as a function of elevation for the sources observed during the calibration campaign.; col.(1) lists the source name.; col.(2) & col.(3) give the [count/Jy] polynomial as a function of elevation for LCP & RCP respectively.; col.(4) & col.(5) give the [count/Jy] factor corrected for opacity at an elevation of 45° for LCP & RCP respectively.

Source	[count/Jy] polynomial corrected for opacity		[count/Jy] factor (El=45°) corrected for opacity	
	LCP	RCP	LCP	RCP
3C48	-0.00014X^2 + 0.01545X +0.59712	-0.00010X^2 + 0.0124X +0.52556	1.00	0.87
3C84	-0.00011X^2 + 0.01372X +0.62579	-0.00008X^2 + 0.01109X +0.58916	1.01	0.92
3C273	0.00041X^2 − 0.03103X +1.24559	0.00031X^2 − 0.02383X +1.04077	0.67	0.59
3C286	-0.00010X^2 + 0.00862X +0.79431	-0.00008X^2 + 0.00734X+ 0.70492	0.97	0.87
3C295	-0.00003X^2 − 0.00036X +1.06041	-0.00013X^2 + 0.01233X +0.60537	0.98	0.89
1611+343	-0.00004X^2 + 0.00313X +0.40073	-0.00003X^2 + 0.00314X +0.32347	0.46	0.40
DR21	-0.00015X^2 + 0.01919X +0.26472	-0.00013X^2 + 0.01620X +0.26464	0.82	0.72
NGC7027	-0.00023X^2 + 0.02906X +0.04701	-0.00020X^2 + 0.02539X +0.05924	0.88	0.79

- Sources 3C84, 3C147, 3C273 and 1611+343 are variable. Therefore their flux densities should be calibrated with respect to the primary calibrators (bootstrapping) before calculating the [count/Jy] factor.

4.5.1 Gain - elevation correction hypothesis for MF receiver data

The gain of a telescope varies with elevation due to many degradation factors (see Subsection 2.4.4). Elevation dependence of the telescope should be taken into account while calculating [count/Jy] factor.

Gain of a telescope 'G' can be given as:

$$G = const. * \eta_A \frac{K}{Jy} \tag{4.4}$$

where $const = 0.292$ (see Eq. 2.6) and the antenna efficiency, η_A accounts for many degrading factors including dish distortion due to gravity at different elevations (see Eq. 2.8) .

For the MF receiver, telescope gain ($\frac{K}{Jy}$) is maximum at an elevation of 60° (see Subsection 2.7.3), therefore a relative gain correction should be applied to account for elevation.

A relative gain correction factor 'G$_{relative}$'can be is given as:

$$G_{relative} = \begin{cases} \frac{G(60^\circ)}{G(El)} & \text{if } El < 60^\circ \\ 1 & \text{if El} \geq 60^\circ \end{cases}$$

where $G(60^\circ)$ and $G(El)$ are calculated from the gain elevation curve evaluated for the MF receiver (see Figure 2.24).
This hypothesis was applied for each source. Figure 4.10 shows the gain correction for source 3C84 where the effect can be noticed prominently.

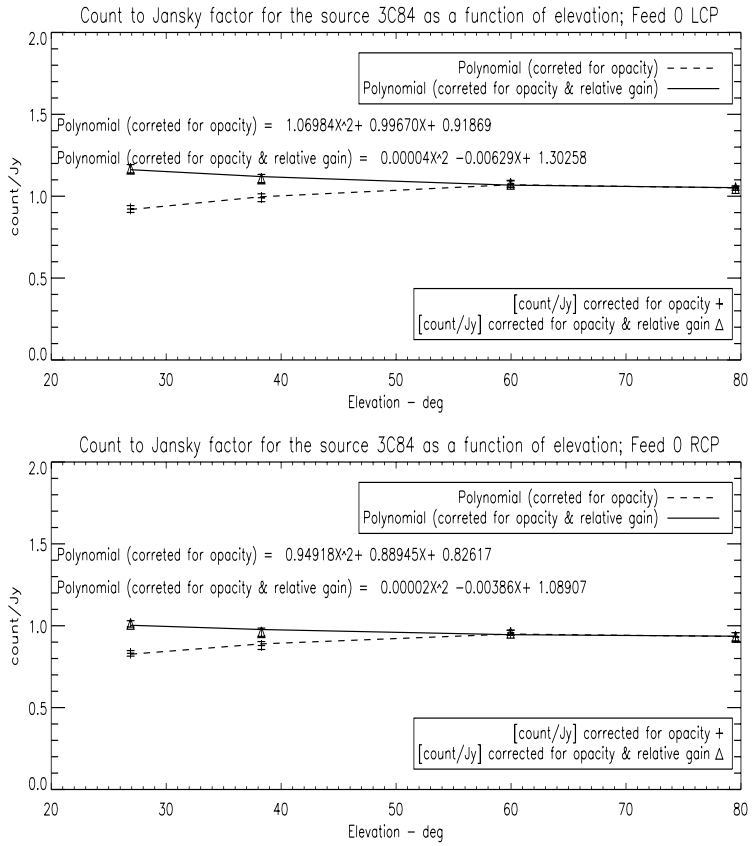

Figure 4.10: Count to Jansky factor obtained for source 3C84 as a function of elevation. Symbol + represents the count to Jansky factor corrected for opacity while symbol Δ represents count to Jansky factor corrected for both opacity & relative gain respectively. Dotted lines in the plots show the polynomial obtained after opacity correction while solid lines give the polynomial fitted to the data after correcting for both opacity and relative gain. Top: Left circular polarization; Bottom: Right circular polarization.

4.6 Conclusions

From the overall analysis presented here the following conclusions can be drawn:

- The measured beam size at 21 GHz agrees with the expected value (100 arcsec) with offsets of the order of 1-4 arcsec in both right ascension and declination directions except the case of the source 3C48, for which the offset in RA direction is approximately 6 arcsec for LCP.
- The measured RA and Dec positions can show very large offsets with respect to the ones used to point the telescope (up to 20-30 arcsec). However the mean offset values are typically of the order of 4-6 arcsec i.e. within the allowed telescope pointing precision ($\approx 1/10$ of the antenna beam; ≈ 100 arcsec). It is worth mentioning that the pointing of the MF receiver at Medicina telescope is very precise even for the weak source (3C295 ≈ 1 Jy)
- There is no significant correlation between RA or Dec offsets and elevation, at least in the elevation range $40° - 80°$, where the mean values are of the same order of magnitude as the ones presented in Table 4.2. At low elevations ($\leq 30°$) the telescope pointing is less stable and the measured offsets seem to be uncorrelated to the one obtained at higher elevations. However they are of the same order of magnitude.
- No significant correlation is found between antenna pointing parameters and antenna speed. The mean values of the offsets lie between 4-6 arcsec for both the speeds tested (1.5°/minute and 3.0°/minute).
- The electronic gain of the MF receiver is stable over time.
- Sources 3C48, 3C286 and 3C295 can be used as primary calibrators for both Medicina and SRT telescopes.
- Source DR21 can be used as a primary calibrator as it is point-like for Medicina telescope at 21 GHz; however it is not suitable for larger telescopes like the SRT. In addition it shows variability at the level of 5-10% (Ott et al., 1994).
- The Count to Jansky [count/Jy] polynomial retrieved for the non-variable sources 3C48, 3C286 and 3C295 (see Section 4.3) can be used for absolute calibration of the MF receiver data at 21 GHz.

- The Count to Jansky factor obtained for source NGC7027 can also be used for amplitude calibration at 21 GHz but source size and secular changes of the spectrum should be taken into account (Ott et al., 1994).
- Sources 3C84, 3C273 and 1611+343 are variable; therefore their flux densities should be calibrated with respect to primary calibrators (bootstrapping) before calculating the [count/Jy] factor. The same is true for source 3C147 which was used as a secondary calibrator for the pilot survey.
- The [count/Jy] factor should also be corrected for the elevation, as the gain of the receiver varies with elevation.

Chapter 5

MF Receiver Scientific Capabilities: Pilot survey at 21 GHz

In the previous chapters I detailed the several phases of the commissioning of the MF receiver at the Medicina telescope. In this chapter I will give an overview of the final phase of the commissioning, with a description of the pilot survey carried out as part of the commissioning. In Section 5.1 I will describe the pilot survey and the preliminary results. Section 5.2 will focus on the follow-up observations of a sub-sample of source candidate list performed at 30 GHz. In Section 5.3 will give an overview of the multi-frequency follow-up of the full source candidate list at 21, 8 and 5 GHz and the preliminary K-band source counts will be presented in Section 5.4.

Large area surveys at high frequency with high sensitivity, are very time consuming due to the fact that the time required to survey the sky increases with the inverse square of the beam size. As a result, there are very few high sensitivity ($<$ 100 mJy) large-scale surveys existing at frequencies greater than 5 GHz (see Chapter 1, Table 1.1). On the other hand high frequency extragalactic surveys are expected to play an important role in the interpretation of temperature and polarization maps of the Cosmic Microwave Background (CMB). CMB experiments provide a major source of information relevant to several cosmological and astrophysical issues, such as testing theories of the early evolution of the universe and the origin of cosmic structure. However CMB experiments are limited by statistical and

systematic errors, such as the contamination from several types of foregrounds. Among these, extragalactic radio sources are expected to play a major role at centimeter wavelengths especially at high latitude and for B-mode polarization related experiments. The radio source population is not well known at frequencies >10 GHz, and many sources are expected to be variable and/or have rising spectral indices (where $S \propto \nu^{\alpha}$). The knowledge of their positions and of their flux densities is crucial to remove their contaminating contribution and estimate the residual error due to the faint and unresolved component in CMB maps.

Existing high sensitivity ground based surveys above 8 GHz in the northern sky consists mainly in the blind radio survey at 15.2 GHz covering an area of 63 deg^2 carried out by Taylor et al. (2001) with the Ryle telescope and detecting 66 sources to a limiting flux density of 20 mJy. Later on the survey area was extended to 520 deg^2 by Waldram et al. (2003), detecting 465 sources to a flux density limit of 25 mJy (the 9C survey). From both of these surveys we learnt that the flux density of sources at 15 GHz cannot be accurately predicted by extrapolation from lower frequency radio surveys such as the NRAO (National Radio Astronomy Observatory) VLA (Very Large Array) Sky Survey (NVSS) at 1.4 GHz (Condon et al. 1998). An important step towards has been made with the survey performed with the Australia Telescope at 20 GHz (AT20G), which has observed the entire Southern sky detecting around 6000 sources down to a flux density limit of 50 mJy (e.g. Ricci et al. 2004; Massardi et al. 2008; Murphy et al. 2010; Hancock et al. 2011). The AT20G has tremendously increased our knowledge of the high frequency radio population in the Southern sky (Hancock et al. 2010; Massardi et al. 2010). This further demonstrates the need for large-scale high-frequency surveys in the Northern sky complementing the AT20G for population characterization and source subtraction in CMB studies.

5.1 KNoWS: Pilot survey

This section presents the pilot survey performed at 21 GHz at Medicina (Italy) as part of the commissioning of the MF receiver, to check its scientific capabilities. The observations were planned to map the North Celestial Polar Cap (declination $> 72.3°$) and were aimed at testing the feasibility of an ambitious project: the K-band NOrthern Wide Survey (KNoWS) aimed at imaging the entire Northern sky

at 21 GHz down to the same limit as the AT20G (50 mJy). This is an international collaboration, involving many astronomers from the Istituto di Radioastronomia (Bologna, Italy). (hereafter KNoWS team). My contribution to the KNoWS pilot survey includes:

- participation to observations
- data quality assessment: data quality of the raw data files was visually inspected and good quality data were provided to produce the final maps.
- pointing and flux calibration
- follow-up observations at 30 GHz

In the following I will give an overall description of the project.

5.1.1 Preliminary observations

During winter 2008-2009 preliminary observations were carried out to test the MF receiver, total power backend and the newly developed antenna control system, (Enhanced Single-dish Control System, ESCS), working together for the first time. ESCS is the recently developed antenna control system at Medicina optimized for single-dish observations. Prior to this antenna control system, the Medicina telescope was equipped only with the antenna control software developed and distributed by the VLBI consortium to carry out observations dedicated to interferometry (FS - Field System). The observations were carried out by S. Righini, a member of the KNoWS team. Many system instabilities were identified during this observing session and removed later on in the laboratory. For example, the second LO of the MF, which showed an inconstant power level causing sudden jumps in the signal, was substituted, and the cross-talk between the backend boards was eliminated. Further tests were performed in August 2009 using the total power backend attached to the 5 GHz receiver to disentangle the frontend/backend contributions to the observed inconsistencies (for more details see Righini, S., PhD thesis 2010).

Among the many instabilities encountered, there was one feature which affected our data so much that we were not able to extract any scientific information from the images. Several tests were carried out to find the origin of this quasi-periodic signal later referred as "JIGGLING". The results of these tests led us to conclude that

jiggling was independent of time, antenna position, scanning strategy and weather conditions. The random spiky features in Figure 5.1 shows the sudden appearance of the jiggling in a On The Fly (OTF) scan. When the jiggling phenomenon turns on, it could affect a scan partially as well as entirely. Therefore it was very evident that, in presence of jiggling, no useful information can be extracted from the images.

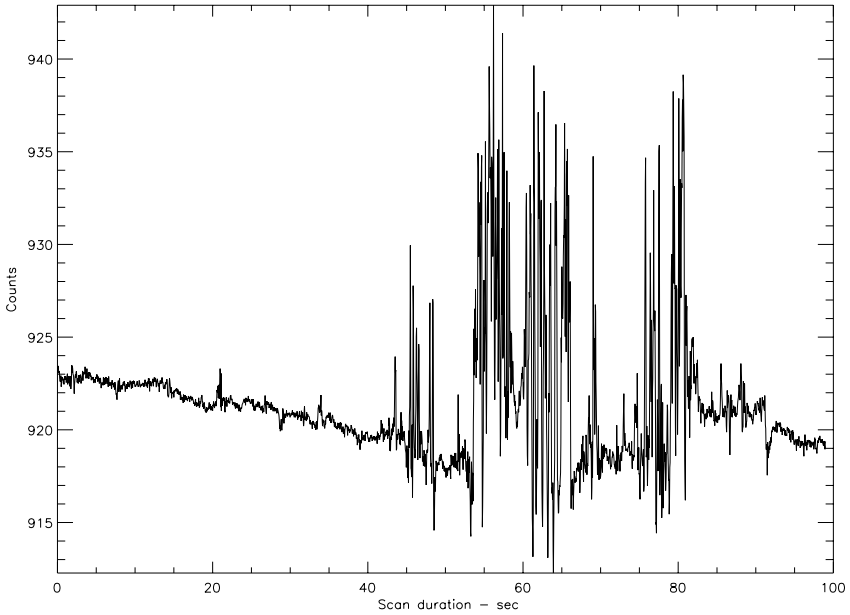

Figure 5.1: On The Fly scan performed during the pilot survey in the polar cap region covering an azimuth range [1°, 25°] at an elevation of 44.52°. X-axis represents the duration of the scan, Y-axis represents the amplitude in an arbitrary backend unit. The random spike feature in the scan shows the jiggling phenomenon.

Since the system had undergone several modifications, in order to remove the instabilities found during winter 2008-2009 pilot observations and the origin of the jiggling was still unknown, another commissioning session was launched in winter 2009-2010 with the following goals:

- to check the system stability of the entire system after the modification done to the hardware.
- to pin point the origin of the 'jiggling'.
- to perform the KNoWS pilot survey in order to prove the scientific capabilities

of the receiver.

5.1.2 Observing strategy

During winter 2009-2010 MF receiver was coupled with the total power analogue backend to map the Northern polar cap region (declination $> 72.3°$) covering an area of 1000 square degrees. The scanning strategy was based on the On The Fly (OTF) mapping technique in which the telescope is driven smoothly and rapidly across a region of sky while continuously acquiring data. In order to get a regular sampling of the MF receiver field of view along the elevation axis, the MF receiver was rotated by an angle $\alpha = 19.1°$ from its mount position[1](rest position). In Figure 5.2 (left) grey circles show the projected beams in the sky when the MF receiver at rest position while empty circles refer to the 19.1° rotated position of the beams with respect to the central beam which allows to fully sample the sky along the elevation axis while scanning in azimuth direction (see Figure 5.2, right)

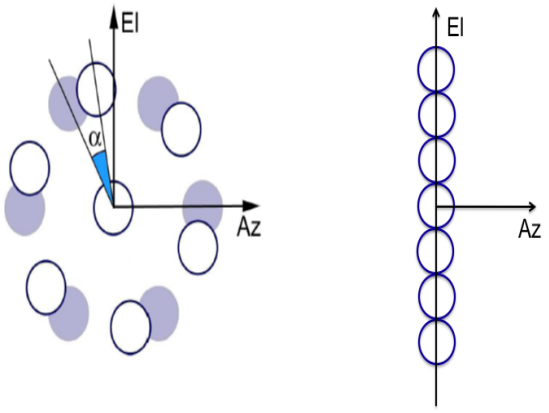

Figure 5.2: The projected beams in the sky in the AZ-El frame. Empty circles represent the rotated positions of the array ($\alpha = 19.1°$).

Each azimuth scan covers a range of [1°, 25°] and scanning is performed continuously at a constant elevation of 44.52° with a scan rate of 15°/minute (Carretti et al., 2010), and a sampling time of 40 ms. This strategy allows to span desired declination range (72.3°-90°) while the earth's rotation allows to span the full right ascension range in a zig-zag pattern in 24 hours (see Figure 5.3).

[1]The position of the MF receiver at which it was mounted. The system can be rotated using the de-rotator onboard

Fully sampled coverage of the Northern Cap is achieved by repeating this observing scheme over multiple days, each day shifting the scanning path by half a beam size. Using this strategy 4 days are required to complete the pilot survey.

5.1.3 Data quality and instabilities

The first observing session was performed in December 2009. Data quality was checked manually scan by scan. Even if the entire observing session was badly affected by poor weather, the system was found to be stable: except for the jiggling, no other instabilities previously reported were found during this session. Figure

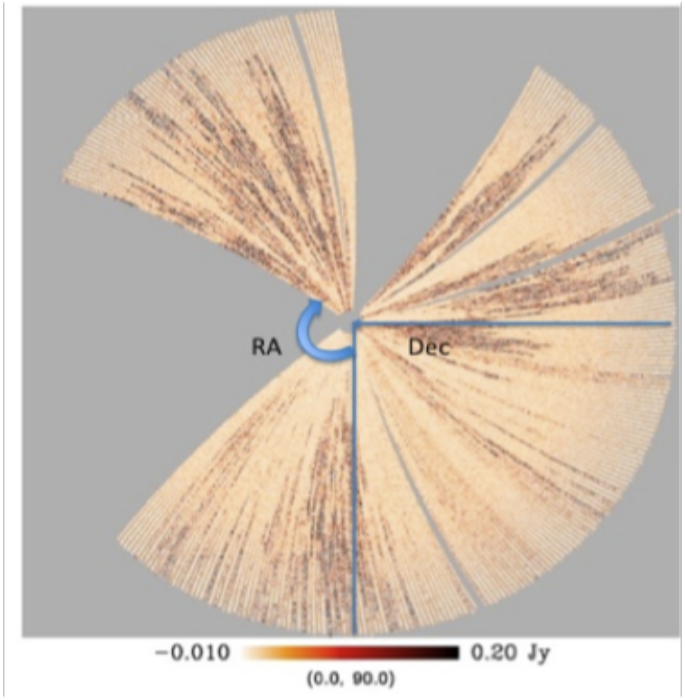

Figure 5.3: Map of the polar cap (Dec $> 72.3°$) obtained along 24 hours of scans between $1°$ and $25°$ of azimuth at a constant elevation of $44.52°$ in the frequency band 20-22 GHz. The black stripes show the jiggling effect while blank wide gaps are due to removal of scans affected by bad weather (courtesy S. Righini).

5.3 shows how badly the jiggling phenomenon affects our astronomical observations. This map was obtained along 24 sidereal hours through scans in azimuth between $1°$ and $25°$ at a constant elevation of $44.52°$. The missing areas are due to the removal of scans achieved in adverse weather conditions. Narrow gaps are due to the time spent to observe the calibrators and black-stripes are due to jiggling. It can be noticed that the data is highly affected by jiggling.

5.1.3.1 Jiggling mitigation campaign

A jiggling mitigation campaign was launched in January 2010 to understand the origin of the jiggling phenomenon. Various simultaneous tests were performed by acquiring the data looking at the zenith:

- A hot load was placed in front of Feed 2 to isolate the receiver from the sky and investigate whether the signal was generated internally.
- Local oscillator (LO) was monitored by connecting it to Feed 6 Left Circular Polarization (LCP).
- White noise (instead of the sky) was observed in Feed 3 Left Circular Polarization (LCP) chain: the signal coming from the LNA was replaced with a Gaussian noise generator.
- A Spectrum Analyzer (SA) was connected to the LNA of Feed 4 Right Circular Polarization (RCP) to search for RFI signals in the observing band.
- The coaxial cable carrying the 1^{st} LO was exchanged with another one, shorter and less sensitive to vibrations.

All these tests led us to conclude that the jiggling origin was external to the system. The supporting evidence was that the jiggling was absent in the channels blinded by the hot load, while still present in the other channels. However, since the jiggling is not related to RFI signals, it was difficult to identify its source of origin.

To ascertain if the contamination was injected in the system by an external device, all the receivers and auxiliary electronics present in the primary and secondary focus cabin were turned off; but the jiggling phenomenon was still present.

Finally it was realized that the jiggling could be originated by the interaction between the secondary focus cabin plastic cover and the wind. A real time acquisition system was set up in parallel to the ESCS acquisition system to test this hypothesis. The jiggling was reproduced by shaking the plastic cover manually. Figure 5.4a and Figure 5.4b show the radio transparent plastic cover placed on the secondary focus cabin and the jiggling reproduced by manually shaking it. After recognizing the jiggling origin, an ad hoc radio transparent polystyrene structure was installed to tighten the cover. After resolving the jiggling issue, the system was found

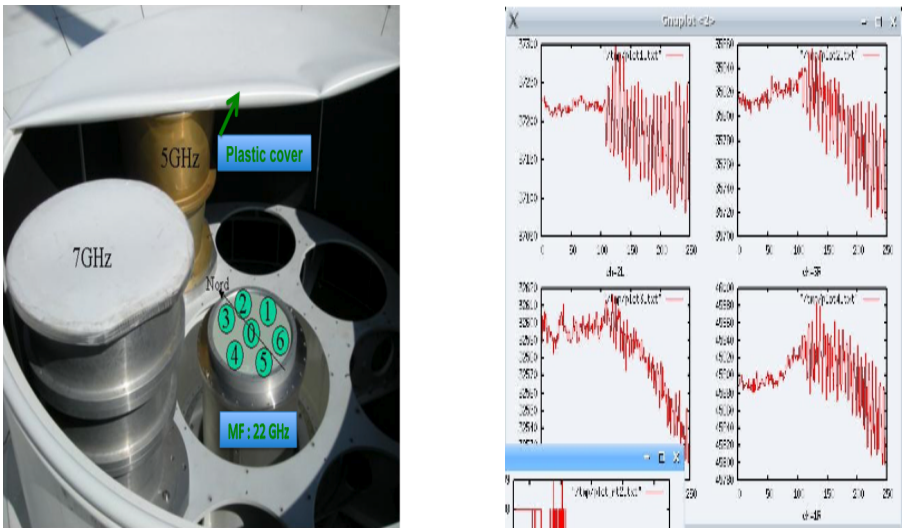

(a) Top view of the cassegrain focus of Medicina 32-m dish.

(b) Jiggling phenomenon produced by shaking the plastic cover.

Figure 5.4: Jiggling removal reproduction.

to be stable and no large scale instabilities were noticed again. Nevertheless it should be mentioned that this ad hoc solution for jiggling is temporary and a permanent solution must be found. Also important to notice is the fact that this problem with the secondary focus cabin plastic cover, never noticed before at Medicina, showed up due to the unprecedented sensitivity of the new MF receiver and the 2 GHz bandwidth total power backend.

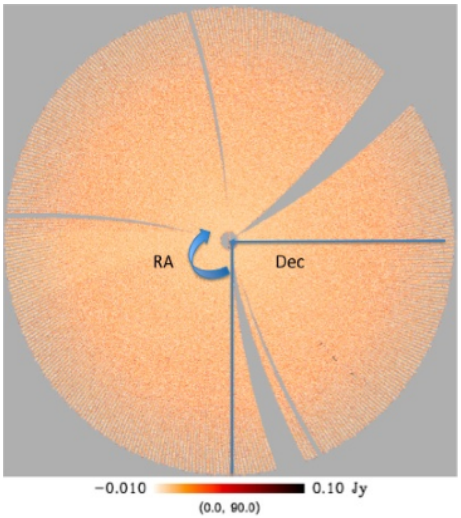

Figure 5.5: Map of the polar cap (Dec $> 72.3°$) obtained along 24 hours of scans between $1°$ and $25°$ of azimuth at a constant elevation of $44.52°$ in the frequency band 20-22 GHz (courtesy S. Righini). The map is totally free of jiggling.

5.1.4 New Observation: Calibration and data reduction

The pilot survey was then repeated (Februray-March, 2010) and the new images were found to be completely free from the jiggling phenomenon (see Figure 5.5).

5.1.4.1 Pointing accuracy and data calibration

The pointing accuracy of the MF receiver during the survey was determined by observing three calibrators 3C48, 3C286 and 3C147 (see Table 4.1) every six hours, whenever they transit at the same elevation (44.52°) of the pilot survey observations. Cross-scans were performed as for the calibration campaign (see Chapter 4), first in right ascension and then in declination directions. Table 5.1 summarizes the scan quality statistics for each calibrator.

Table 5.1: Observation summary for the calibrators observed during the pilot survey; col.(1) lists the source name; col.(2) & col.(3) give the number of good quality RA and Dec scans; col.(4) & col.(5) give the % of scans discarded due to poor weather.

Source	Good quality scans		% of discarded scans	
	RA scans	Dec scans	RA scans	Dec scans
3C48	36	36	30	30
3C147	22	18	40	50
3C286	60	60	23	23

The data reduction strategy followed to retrieve antenna parameters (Delta RA, Delta Dec, beam FWHM in both RA and Dec directions, and amplitude) is the same as described in Chapter 4. The results obtained for each calibrator are plotted in Appendix E and listed in Tables 5.2, 5.3 and 5.4 respectively. The measured beam FWHM and the offset mean values measured in RA and Dec during the pilot survey are consistent with the ones measured during the calibration campaign for the same sources (see Tables 4.4 and 4.5) and with the overall offsets presented in Table 4.2.

Table 5.2: Antenna position parameters obtained through Gaussian fitting for source 3C48; col.(1) gives the name of the antenna parameter; col.(2) & col.(3) give the mean beam FWHM and the mean offset in RA and Dec for the left circular polarization and right circular polarization.

Parameter	Feed 0 LCP Mean value (arcsec)	Feed 0 RCP Mean value (arcsec)
FWHM (RA)	97.02±1.21	97.77±1.28
FWHM (Dec)	101.03±1.77	101.00±1.77
Delta RA	10.24±0.88	10.85±0.88
Delta Dec	-6.54±0.74	-6.11±1.03

Table 5.3: Antenna position parameters obtained through Gaussian fitting for source 3C286; col.(1) gives the name of the antenna parameter; col.(2) & col.(3) give the mean beam FWHM and the mean offset in RA and Dec for the left circular polarization and right circular polarization.

Parameter	Feed 0 LCP Mean value (arcsec)	Feed 0 RCP Mean value (arcsec)
FWHM (RA)	98.81±0.55	99.21±0.57
FWHM (Dec)	99.72±0.56	99.23±0.57
Delta RA	5.46±0.65	5.95±0.70
Delta Dec	-2.75±1.36	1.91±1.36

Table 5.4: Antenna position parameters obtained through Gaussian fitting for source 3C147; col.(1) gives the name of the antenna parameter; col.(2) & col.(3) give the mean beam FWHM and the mean offset in RA and Dec for the left circular polarization and right circular polarization.

Parameter	Feed 0 LCP Mean value (arcsec)	Feed 0 RCP Mean value (arcsec)
FWHM (RA)	99.36±1.03	101.08±1.15
FWHM (Dec)	98.97±1.00	101.54±1.15
Delta RA	-3.83±1.43	-4.82±1.28
Delta Dec	4.00±0.77	4.00±0.82

The flux calibration of the pilot survey observations is based on the flux scale of Ott et al (1994). Our primary flux calibrator 3C286 has a flux of 2.56 Jy at our observing frequency (21 GHz). The atmospheric contribution was measured by performing skydip procedure (described in Chapter 4). The count to Jansky conversion factor required to calibrate the MF receiver data was directly obtained from 3C286 measurements (see Figure 5.6) following the same procedure as described in Chapter 4.

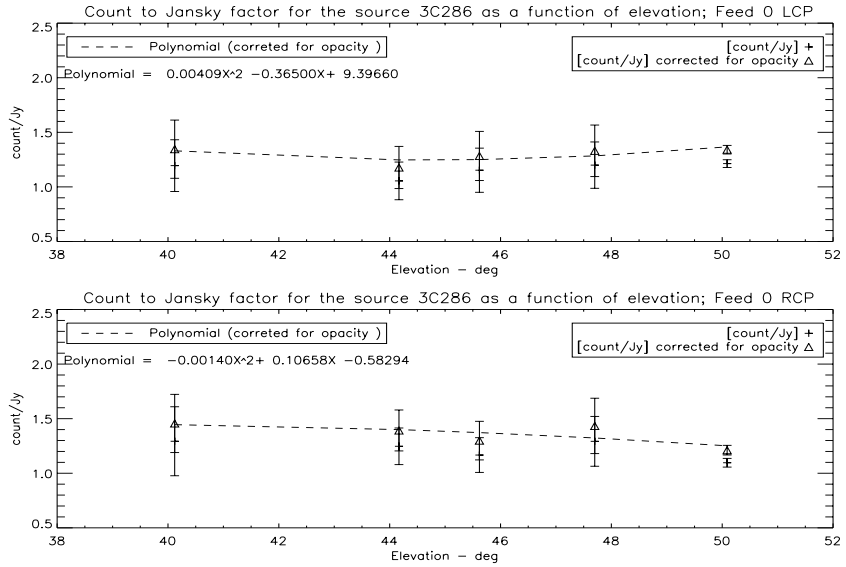

Figure 5.6: The count to Jansky factor obtained for source 3C286 as a function of elevation. Symbols + and Δ represent the count to Jansky factor before and after correcting for opacity respectively. The dashed lines correspond to the polynomial obtained after correcting for atmospheric absorption. Top: Left circular polarization; Bottom: Right circular polarization.

5.1.5 Mapping and source extraction

The final maps were produced using two independent map-making strategies optimized for compact sources, while source extraction was performed in three independent ways. A brief description of the map-making and source extraction strategies follows:

(1) In the first map-making technique (developed by R.Ricci, a member of KNoWS team), raw data was calibrated in flux using source 3C286 observed every 12 hours during the survey. To remove atmosphere, ground pickup or instrumental offsets, a running mean of the signal amplitude was computed for each 40 ms integration sample by averaging over an interval of 12 integration samples (corresponding to $\approx$ 3 FWHM of antenna beamsize). The baseline was then subtracted by removing the running mean amplitude from the local amplitude of each integration sample. This was done for each feed and polarization separately. The scans were then mapped one by one on a 4800×4800 pixel grid with $30''$ pixel size using an equal-area polar projection. Lateral feed positions with respect to the central one were derived from the MF-receiver geometry and the applied rotation

angle $\alpha = 19.1°$, while the flux calibration of the lateral feeds was performed using the antenna gain for lateral feeds (see Chapter 2).

In order to extract the sources from the surface brightness (Jy/beam) pixel map, a sensitivity map was obtained by computing the flux standard deviation in a 20×20 pixel box centered around each pixel of the surface brightness map. By matching the sensitivity map and the brightness map a list of hot pixels ($\geq 5\sigma$) was then extracted. Neighboring hot pixels were removed within a radius of 1 FWHM to single out candidate sources. Finally, to improve position and flux accuracy a 2D Gaussian model was fitted to each candidate to extract the best-fit RA/Dec positions and peak brightness.

(2) The second map-making software used is described in Carretti et al. (2010). In this strategy a high-pass filter was firstly applied to each scan to remove large scale emission. This cleans out any long-term signal variations due to system instabilities (gain fluctuations,1/f noise, etc) but makes the map insensitive to very extended sources. After that the data from all the scans were binned with a pixel size of half a FWHM to match the Nyquist sampling criteria. The HEALPix (Hierarchical Equal Area isoLatitude Pixelization) map scheme was adopted as it is particularly suited for all-sky maps or maps around polar caps (for more details, see Righini et al. 2010). The source extraction from this map was performed either using a software tool developed as a part of the Planck collaboration (for more details see Caniego M.L, et al. 2006 and Massardi et al. 2009) or using the SExtractor tool (Bertin.E. & Arnouts.S., 1996). In both cases the minimum signal to noise ratio (SNR) threshold adopted is approximately 4σ. Removal of obvious fake sources were done later, through visual inspection by members of the KNoWS team. The three independent candidate source lists were finally merged into a single list of 151 objects.

5.1.6 Survey sensitivity:

The nominal noise expected for the pilot survey can be calculated using the radiometer equation (see Chapter 1):

$$\Delta T = \frac{kT_{sys}}{\sqrt{Bt}} \tag{5.1}$$

where $k = \frac{1}{\sqrt{2}}$ (for total power), T_{sys}, is the system temperature, B is the bandwidth and t is the integration time. Considering $T_{sys} = 75$ K (see section 2.7.1), B = 2

GHz, t = 0.96 s (integration time per beam-sized pixel), antenna gain = 0.1 $\frac{K}{Jy}$ (see section 2.7.3), the expected average survey rms sensitivity is 12.1 mJy.

A quantitative representation of the sensitivity map obtained through the first map-making technique is shown in Figure 5.7 where the effective area (A_{eff}) is plotted as a function of rms noise (1σ). This corresponds to the surveyed area over which a certain sensitivity was achieved. It should be mentioned that the area above Dec $\geq 85°$ was badly polluted by RFI signals, and was discarded when producing the sensitivity map. During the survey rather poor weather conditions were encountered. As a result the noise in the map is higher than expected. The average value of the rms noise is approximately 25 mJy (see Figure 5.7).

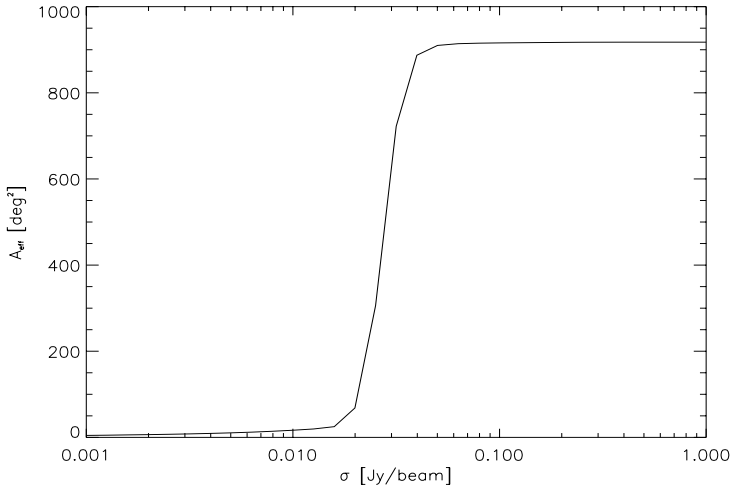

Figure 5.7: Effective area (square degrees) as a function of 1σ sensitivity (Jy/beam). Courtesy R.Ricci (Righini et al. 2011, in prep).

5.2 Follow-up observations at 30 GHz

As part of ESTRELA (Early-Stage TRaining site for European Long-wavelength Astronomy) network during my PhD thesis I have participated to the 30 GHz OCRA-F (One Centimeter Radio Array -Faraday) multi-feed commissioning in collaboration with the OCRA consortium. The OCRA-F receiver is the second receiver of the OCRA program (Browne et al., 2000) at 30 GHz and currently undergoing commissioning at the Toruń Telescope (Poland). This collaboration gave me the opportunity to carry out a first set of follow-up observations at 30 GHz

to confirm the candidate sources found in the pilot survey.

This was very useful, since the MF receiver was dismounted just after the pilot survey completion to replace the faulty channels (see Chapter 2) and as a consequence follow-up observation at 21 GHz could not be carried out immediately. The 30 GHz observations of the candidate source list were carried out using the OCRA-p receiver mounted on the 32-m Toruń telescope. This is the prototype instrument of the OCRA programme (Browne et al., 2000). OCRA-p receiver (see Figure 5.8) is a dual-beam 30 GHz radiometer based on the concept of pseudo-correlations. The basic design of the receiver is taken from the Planck Low Frequency Instrument (LFI, Mandolesi et al. 2000). The nominal sensitivity of the receiver, considering an overall system temperature of 40 K and a bandwidth of 6 GHz, is 6 mJy $s^{1/2}$. The FWHM of the antenna beam at 30 GHz is 72″.

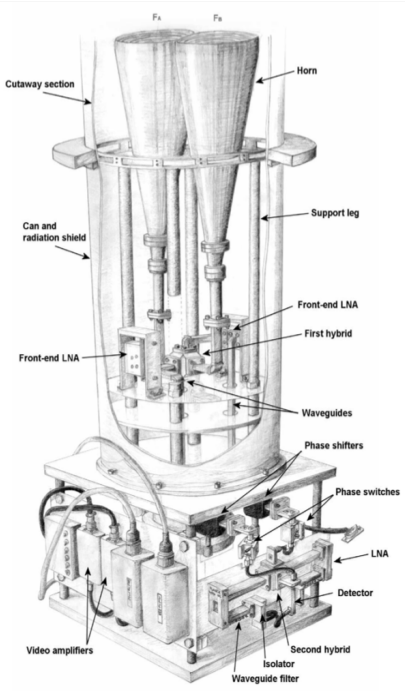

Figure 5.8: Sketch diagram of the OCRA-p receiver showing all the main components. When the receiver is mounted on the telescope, the two feed horns FA and FB have an offset in azimuth but the same elevation (courtesy S. R. Lowe).

For the follow-up observations a subsample of 103 'reliable' candidates extracted from the 151 source candidate list was selected. Such sources have a crossmatch with NVSS within a radius of 60″. An additional sources was included in the target sample even if it does not have NVSS counterpart, as it is among the brightest sources found in the pilot survey (1.6 Jy). The 30 GHz observation were carried

out on September 9^{th}, November 15^{th} and December 3^{rd}, 2010 by M.P Gawroński (Center for Astronomy NIcolaus Copernicus University, Torun, Poland).

The sources were observed using cross-scan or on-off measurements depending on the source flux (Lowe, et al. 2007, Gawroński et al., 2010). In unclear cases observations were repeated to confirm the source detection.

Planetary nebula NGC 7027 was used as primary flux density calibrator. NGC 7027 was observed 6 - 10 times for each observing session. Hafez et al. (2008) report a flux density of 5.39±0.04 Jy at 33 GHz at an epoch of 2003.0 with a secular decrease of -0.17±0.03 per cent per year (Ott et al. 1994). By extrapolating the flux density to 2010.0 a value of 5.32±0.04 Jy was obtained which was then scaled to 30 GHz using the NGC 7027 spectral index of -0.119. The 30 GHz flux density of NGC 7027 thus obtained is 5.38±0.04 Jy. Secondary flux density calibration was performed using the signal generated from a noise diode after each source observation. NGC 7027 was measured at different elevations in order to obtain elevation-dependent gain corrections. The correction for atmospheric absorption was done by calculating the opacity from the system temperature measurements at the zenith and at 30° of elevation.

The data reduction was done using the software package provided by M.W.Peel (Jodrell Bank Center for Astrophysics, University of Manchester, Manchester, UK). Data affected by poor weather conditions were discarded, as well as cross-scan data where the peak amplitude measured by the two OCRA-p beams was offset by 20 percent or more. In total 295 measurements were performed. 57 sources out of the 104 target source were detected at 30 GHz. 30 GHz flux densities of the detected sources are listed in Table 5.5 together with the 1.4 flux densities from NVSS (Condon et al., 1998) and preliminary 21 GHz flux densities obtained from the pilot survey.

Table 5.5: Flux densities of the sources confirmed at 30 GHz; col.(1) & col.(2) give source position coordinates (RA and Dec); col.(3) gives preliminary flux densities at 21 GHz obtained from the pilot survey map (Righini et al. 2011, in prep); col.(4) gives the flux densities at 1.4 GHz from NVSS (Condon et al., 1998); col.(5) gives the flux densities measured at 30 GHz.

RA (J2000) (hhmmss.sss)	Dec(J2000) (ddmmss.sss)	Flux 21 GHz (mJy)	Flux 1.4 GHz (mJy)	Flux 30 GHz (mJy)

Continued to next page

00 13 09.600	72 31 22.809	231.42	371.5	202±5
00 17 10.640	81 35 05.173	381.83	692.8	480±20
00 19 48.133	73 27 45.527	769.64	1251.8	914±15
02 03 29.747	72 33 31.981	250.66	229.9	420±22
02 07 11.276	84 11 08.848	118.74	100.0	189±14
02 09 55.746	72 29 20.037	196.41	669.9	521±11
02 17 28.838	73 49 44.738	1928.67	2271.6	2739 ±96
03 54 39.298	80 10 03.754	168.03	643.7	314±7
04 10 49.223	76 56 32.880	1128.19	5620.1	962±36
04 13 08.640	74 51 03.593	195.85	2666.2	152±11
04 21 42.855	83 58 33.757	148.47	5.2	188±16
04 23 07.288	76 23 48.113	1665.00	(*)	929±24
05 08 26.992	84 31 50.110	135.37	294.8	140±12
06 10 42.935	72 48 37.969	196.99	1041.6	220±6
06 25 55.074	82 02 14.885	316.17	681.0	458±11
06 39 21.975	73 24 43.264	726.22	903.6	1254±48
07 26 10.125	79 11 24.998	441.41	501.0	405±17
07 47 10.979	76 39 05.059	282.52	133.1	373±17
07 49 20.438	74 20 15.802	201.95	510.3	244±7
07 50 40.066	79 09 18.051	177.05	181.5	339±16
07 50 52.898	82 41 40.845	268.57	1845.1	337±26
08 08 14.398	73 15 39.606	176.77	300.7	73±14
10 10 06.998	82 49 46.990	242.90	503.7	283±13
10 44 18.812	80 54 27.416	480.95	828.3	577±30
10 58 06.697	81 14 25.613	723.37	240.3	756±27
11 01 54.000	72 25 15.591	670.40	1245.6	904±31
11 04 10.801	76 58 58.806	211.17	1960.9	180±12
11 53 09.286	80 58 20.793	400.49	1343.4	736±29
12 00 16.229	73 00 39.990	405.62	5564.7	496±12
12 23 28.887	80 39 59.991	304.64	705.1	420±9
12 33 03.334	80 54 31.152	153.95	261.3	98±13
13 21 33.122	83 16 37.202	196.24	565.4	97±9
13 23 46.537	79 42 45.884	305.65	599.4	321±16
13 53 17.464	75 32 52.128	277.62	132.6	348±7
13 57 51.865	76 43 23.101	437.05	647.2	441±23
14 48 27.600	76 01 25.776	384.60	179.2	639±28
15 06 18.534	83 19 09.609	132.59	201.4	217±25
16 32 20.913	82 32 36.693	712.73	492.5	908±40
17 24 02.107	76 53 18.010	272.87	424.0	621±30
18 00 42.661	78 28 20.409	1835.20	2223.5	2376±81

Continued to next page

[1] (*) No NVSS counterpart was found within 60″ radius.

18 23 05.754	79 39 10.800	80.48	278.7	56±5
18 36 55.922	75 07 44.392	218.54	133.9	85±7
18 42 18.673	79 46 15.586	854.22	442.3	564±19
18 54 55.610	73 51 23.450	337.45	390.5	241±8
19 27 50.519	73 58 15.767	4392.95	3950.9	4347±160
20 05 30.757	77 53 07.875	1262.83	993.7	726±14
20 09 48.833	72 30 17.825	407.63	953.6	571±13
20 17 11.616	74 41 11.539	463.59	473.7	443±21
20 22 33.976	76 11 53.095	409.08	428.9	784±29
21 13 55.620	82 05 23.245	161.25	248.7	157±19
21 33 35.202	82 39 27.719	166.38	915.1	167±17
22 05 53.883	74 36 41.990	224.26	235.9	225±17
22 36 30.001	73 22 37.196	181.27	268.2	123± 7
23 05 40.075	82 42 32.399	153.46	116.7	95±20
23 12 22.799	72 41 13.187	163.71	270.6	143±11
23 26 55.018	80 13 06.539	101.09	138.4	180±7
23 56 38.133	81 53 01.833	453.75	520.9	715±35

5.3 Follow-up observations at 21, 8 and 5 GHz

The MF receiver was remounted on the Medicina telescope in November 2010 and follow-up observations of the full 151 candidate source list were carried out at several frequencies (21, 8 and 5 GHz) in December 2010. The candidate sources were first observed at 21 GHz and 5 GHz. The confirmed sources were then followed-up at 8 GHz. The sources were observed by the KNoWS team in conventional cross-scan method, first in right ascension and then in declination. Multiple cross scans were performed for each candidate to reach the required signal to noise ratio. The observation setup parameters are listed in Table 5.6. The data reduction for this set of measurements is still ongoing. As a preliminary result 70 sources were found to be detected at 21 GHz. All of them were detected at 5 GHz and 66 sources were also detected at 8 GHz. It is worth mentioning that all the 57 sources detected at 30 GHz were detected at 21 and 5 GHz as well.

Table 5.6: System parameters for follow-up observations

Receiver code	CCC	XXP	KKC
Frequency (GHz)	5.0	8.3	21.0
Beamsize (arcmin)	7.5	4.8	1.7
Tsys (K)	26	40	70
Gain (K/Jy)	0.160	0.141	0.100
Bandwidth (MHz)	230	230	1900
Sampling interval (s)	0.12	0.12	0.12
Scan length (arcmin)	52.5	33.2	11.9
Scan+turning time duration (s)	22.5	21.8	16.9
Single scan instantaneous rms-noise (mJy)	21.9	38.2	32.8

5.4 K-band source counts

Preliminary source counts at 21 GHz have been determined using the flux densities of the sources obtained from the pilot survey maps (Righini et al. 2011, in prep) for the 70 confirmed sources. The purpose is to demonstrate the completeness limits of the survey.

The counts were logarithmically binned in flux density, starting from a flux density limit of 100 mJy. The differential counts n_i as a function of source flux density have been derived as follows:

$$n_i = \frac{1}{\Delta log(S)} \sum_{j}^{N_i} \frac{1}{A_{eff}(S_j)} \tag{5.2}$$

$$log(S_i) \leq log(S_j) < log(S_i) + \Delta log(S) \tag{5.3}$$

$$\Delta n_i = \frac{\sqrt{N_i}}{A_{eff}(S_i)\Delta log(S)} \tag{5.4}$$

where n_i in Eq. 5.2 represents the number of sources N_i in a logarithmic flux density bin i defined in Eq. 5.3. The counts are weighted source by source using the effective area A_{eff} as a function of limiting flux density S = 4×σ. Δn_i is the Poissonian error to the counts n_i weighted at the flux density S_i of the bin center.

The differential counts are shown in Figure 5.9, where they are compared to the expected counts from de Zotti et al. (2005) model. From the comparison we notice some incompleteness in our source sample at fluxes S $\leq$ 500 mJy. This incompleteness may be partly explained by the fact that 6 sources were not included in the counts determination since their fluxes, as derived from the pilot survey maps, are completely unreliable. As soon as accurate fluxes will be determined from the

21 GHz follow-up observations, a better determination of the counts and a more reliable estimation of the incompleteness effects will be possible.

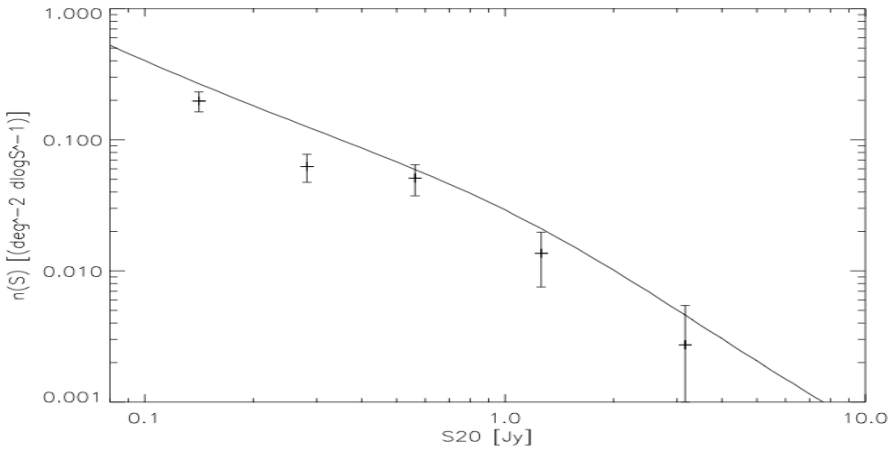

Figure 5.9: Preliminary number counts at 21 GHz (symbols with error bars) of the KNoWS Pilot survey compared with the expected model counts by de Zottti et al. (2005) model (solid line). Courtesy by R.Ricci (Righini et al. 2011, in prep).

5.5 Conclusions

This Chapter has described the final phase of the commissioning of the MF receiver during which a pilot survey at 21 GHz was carried out. The following conclusions can be drawn:

- In order to prove the scientific performance of the MF receiver, the North Celestial Polar cap region (Dec $> 72.3°$) covering an area of 1000 square degrees down to an average detection limit of a 100 mJy was mapped at 21 GHz during the commissioning. A number of 151 candidate sources were extracted from the maps.

- The fast scanning strategy, never used before at Medicina, proved to be successful and allowed to complete the survey in 4 days of suitable weather conditions.

- All major system instabilities were removed including the jiggling phenomenon. Its origin was understood by carrying out several tests, and the problem has been fixed temporarily.

- The pointing of the receiver was found to be within the rms pointing error of the telescope even at the fast scanning rates (15°/min) used for the pilot survey.

- Follow-up observations at 30 GHz of 104 reliable candidates were performed at the Toruń telescope. This allows us to confirm 57 sources.

- Subsequent follow-up observations of the full 151 candidate source list have been carried out at 21, 8 and 5 GHz at Medicina. Preliminary results indicates that 70 sources are detected at 21 GHz as well as at 5 GHz. 66 sources out of 70 were also detected at 8 GHz. All the sources detected at 30 GHz were confirmed at 21 GHz.

- Accurate 21 GHz flux densities are currently being determined for the sources confirmed in the follow-up and few more confirmations are expected (Righini et al. 2011, in prep).

- Preliminary source counts derived with raw 21 GHz flux densities show some incompleteness at S $\leq$500 mJy. This incompleteness is expected to get mitigated when the 21 GHz follow-up analysis of the sources will be finalized and final source counts will be produced.

- As soon as 5, 8, 21 GHz accurate flux densities measurements will be available, a spectral index study of the sample (including the 30 GHz measurements) will be undertaken (Ricci et al. 2011, in prep).

Chapter 6

Conclusions and future work

This thesis has described several phases of the commissioning of the newly developed K-band multi-feed receiver. The new K-band 7-horn multi-feed receiver was designed as part of the EU-funded programme (FARADAY) for the upcoming Sardinia Radio Telescope to carry out high frequency and high sensitivity continuum, spectroscopy and polarimetry observations. The receiver is based on heterodyne receiver technology and operates between 18 and 26.5 GHz with an instantaneous bandwidth of 2 GHz. The receiver shares its uniqueness with the newly built GBT 7-horn K-band multi-feed receiver worldwide. The receiver was mounted in the cassegrain focus of the Medicina 32-m dish to under go commissioning. The main focus of this thesis is on the technical aspects of the commissioning and in particular on pointing and flux calibration of the receiver. In this final chapter I summarize the main results of this thesis and also discuss briefly currently ongoing work and future perspectives.

6.1 System characterization of the MF receiver

The main results of the commissioning measurements made to characterize the MF receiver are summarize as follows:

System characterization

One of the main goals of this thesis was to characterize the receiver performance on the Medicina telescope. A range of measurements were performed (with Mark 4 backend[1]) to get the best optical alignment in order to achieve maximum power

[1] The 7×2 channels total power analogue backend was under construction at the time of the first commissioning measurements.

in the main lobe of the antenna beam and to suppress the sidelobes. An optimized pointing model was obtained for the MF receiver and antenna characteristic parameters (system temperature, beam FWHM, antenna gain, etc) were found to be consistent with laboratory measurements and simulations. The antenna gain as a function of elevation was obtained for the central feed. Lateral feeds antenna gains were measured relative to the central one. The nominal sensitivity of the MF receiver is 12 mJy $s^{1/2}$ (considering T_{sys} = 75 K and antenna gain = 0.1 K/Jy). This work has been published in Verma et al., 2009 (Internal Report, IRA 430/09).

T_{cal} estimation

Accurate values of T_{cal} are necessary for precise measurements of the system temperature. Since T_{cal} varies with frequency and bandwidth. When dealing with large bandwidth and multi-feed receivers like the MF receiver, measuring T_{cal} values with high frequency sampling rate as a function of frequency is very time consuming. For the MF receiver the T_{cal} values were measured in the laboratory over the entire 18-26.5 operational range with a sample rate of 400 MHz (20 measurements) for each feed and polarization. Then a mathematical approach was developed, in which best-fit polynomials were used to fit the bandshape as a function of frequency and interpolated T_{cal} values weighted to the bandshape were obtained for each frequency along the overall 18-26.5 GHz receiver band. Results are found to be in agreement with the T_{cal} values measured in the laboratory (400 MHz steps).

6.2 Calibration campaign

A calibration campaign was carried out to test the pointing of the receiver coupled with the new continuum backend and to develop a strategy for the flux calibration of the MF data in absence of a noise source. The pointing of the receiver was found to be in agreement with the pointing accuracy of the telescope (1/10 of the beam size) and found to be stable for elevations $\geq 40^{\circ}$. The pointing of the receiver was found to be independent of antenna speed and is accurate even for weak sources ($\approx$ 1 Jy).

Since the noise source is not yet implemented in ESCS antenna control system, a methodology was developed to obtain a count to Jy conversion factor to calibrate the MF receiver data. Finally a list of suitable pointing and flux calibrators for

Medicina 21 GHz observations were obtained. Some of them can also be used for the larger Sardinia Radio Telescope. This work has been published in Verma et al., 2011 (Internal Report, IRA 441/11).

6.3 Pilot survey

A pilot survey at 21 GHz, was carried out during the final phase of commissioning in winter 2009-2010 to confirm the scientific capabilities of the MF receiver in the framework of an international collaboration (KNoWS project). The survey was intended to image the Northern polar cap region (Dec $>$ 72.3°) covering approximately 1000 square degrees down to a detection limit of 50 mJy. My main contribution to the KNoWS projects was in participating to the observations; assessing the data quality in order to provide good quality data for the production of the final maps; in performing the survey pointing and flux calibration. The pilot survey has produced a list of 151 candidate sources down to a flux limit of $\approx$ 100 mJy. The fast scanning observing strategy (15°/min) proved to be successful with no effects on pointing accuracy.

6.4 Follow-up observation at 30 GHz

In the framework of my collaboration with the OCRA project (undertaken as member of the European 'ESTRELA' network), follow-up observations at 30 GHz at the Toruń telescope were carried out. This project was done under my responsibility. 104 'reliable' candidates extracted from the 151 source candidate list were observed at 30 GHz and 57 sources were confirmed as real. A list of the 30 GHz fluxes is included in the thesis (see Chapter 5).

6.5 Ongoing work and future prospects

Follow-up multi-frequency (5, 8 and 21 GHz) observations of the full candidate list were carried out at Medicina by members of the KNoWS team. Preliminary results show that 70 sources are confirmed at 21 and 5 GHz. 66 of them were also detected at 8 GHz. All sources detected at 30 GHz were also detected at 21 GHz. The data analysis of the 5, 8 and 21 GHz follow-up observations is ongoing. Accurate flux

densities are currently being determined (Righini et al. 2011, in prep). As soon they will be available, a spectral index study of the sample (including the 30 GHz measurements) will be undertaken (Ricci et al. 2011, in prep).

During the first phase of commissioning of the MF receiver in 2008, two channels (6 RCP and 4 LCP) of the receiver went out of order due to the failure of the low noise amplifiers. The MF receiver was dismounted in summer 2010 and these low noise amplifiers were replaced. During winter 2010-2011 a second pilot survey was carried out to map the equatorial belt (Dec [-1°, 14°]) to test the receiver performance after replacing the broken channels. Observations and data reduction are still ongoing.

Bibliography

[1] **Baars, J.W.M., et al.**, 'The Absolute Spectrum of Cas A;
An Accurate Flux Density Scale and a Set of Secondary Calibrators', *1977, A&A, 61, 99*

[2] **Balanis, C. A.**, 'ANTENNA THEORY: ANALYSIS AND DESIGN', *3rd edition; Wiley Interscience*

[3] **Becker, R.H., et al.**,'The FIRST Survey: Faint Images of the Radio Sky at Twenty Centimeters', *1995, ApJ, 450, 559*

[4] **Bertin, E., Arnouts, S. et al.**,'SExtractor: Software for source extraction', *1996, A&A Suppl. Ser., 117, 393*

[5] **Bolton, J. G., et al.**, 'The Parkes 2700-MHZ Survey - Part Fourteen - Catalogue and New Optical Identification', *2000, AuJPA, 46, 1*

[6] **Browne, I.W.A, et al.**, 'OCRA: a one-centimeter receiver array', *2000, Proc. SPIE, 4015, 299*

[7] **Campbell, B.C.**, 'Measurements in Radio Astronomy', *2002, ASP Conference Series, 278, 81C*

[31] **Carretti,E. et al.**,'Galactic foregrounds and CMB Polarization', *2010, submitted*

[9] **Cenacchi, E., et al.**, 'SRT: MF RECEIVERS', *Internal Report, IRA 384/06*

[11] **Condon, J.J.**, 'THE NRAO VLA SKY SURVEY', *1998, AJ, 115, 1693*

[11] **Condon, J.J.**, 'Continuum 1: General Aspects', *2002, ASP Conference Series, 278, 155C*

[12] **de Zotti, G. et al.**, 'Predictions for high-frequency radio surveys of extragalactic sources', *2005, A&A, 431, 893*

[14] **Emerson, D.T.**, 'Why Single-Dish?', *2002, ASP Conference Series, 278, 27E*

[14] **Emerson, D.T. and Payne, J. M., (eds.)**, 'MF SYSTEMS FOR RADIO TELESCOPE', *ASPacific Conference Series, Volume 75*

[16] **Fanti, C., et al.** , 'Low frequency variable sources 5 year monitoring program at 408 MHz', *A&AS, 45, 61*

[16] **Gawroński, M.P., et al.**, '30 GHz observations of sources in VSA fields', *A&AS, 45, 61*

[17] **Gold, B., et al.**, 'Seven-Year Wilkinson Microwave Anisotropy Probe (WMAP) Observations: Galactic Foreground Emission ', *2011, ApJS, 192, 2*

[18] **Goldsmith, P.F.**, 'Radio Telescope and Measurements at Radio Wavelengths', *2002, ASP Conference Series, 278, 45G*

[19] **Gregory, P.C., et al.**, 'The GB6 Catalog of Radio Sources', *1996, ApJS, 103, 427*

bibitemgriffi **Griffith, M.R., et al.**, 'The Parkes-MIT-NRAO (PMN) surveys. I - The 4850 MHz surveys and data reduction', *1993, AJ, 105, 1666*

[22] **Hafez, Y.A., et al.**,'Radio source calibration for the Very Small Array and other cosmic microwave background instruments at around 30 GHz', *2008, MNRAS, 388, 1775*

[22] **Hancock, P.J., et al.**,'Observations and properties of candidate high-frequency GPS radio sources in AT20G survey', *2010, MNRAS, 408, 1187*

[22] **Hancock, P.J., et al.**, *2011, submitted*

[23] **Jarosik, N., et al.**,'Seven-year Wilkinson Microwave Anisotropy Probe (WMAP) Observations: Sky Maps, Systematic Errors, and Basic Results', *2011, ApJS, 192, 14*

[24] **Jewell, P.R.**, 'Millimeter Wave Calibration Technique',*2002, ASP Conference Series, 278, 313J*

[25] **Kraus, J.D.**, 'Radio Astronomy', *McGraw Hill, 1966*

[31] **López-Caniego M., et al.**,'Comparison of filters for the detection of point sources in Planck simulations', *2006, MNRAS 370, 2047.*

[27] **Mangum, J.G.**,'A Telescope Poiting Algorithm for ALMA', *ALMA Memo 366, 2001.*

[28] **Lowe, S.R., et al.**,'30GHz flux densities of CJF sources ', *2007, A&A, 474, 1093*

[29] **Mandolesi, N., et al.**,'The Planck Low Frequency Instrument', *2000, ApL&C, 37, 151*

[30] **Massardi, M., et al.**,'The Australia Telescope 20-GHz (AT20G) Survey: the Bright Source Sample', *2008, MNRAS, 384, 775*

[31] **Massardi, M., et al.**,'Blind and non-blind source detection in WMAP 5-year maps', *2009, MNRAS 392, 742*

[32] **Massardi, M., et al.**,'The Australia Telescope 20GHz (AT20G) Survey: analysis of the extragalactic source sample', *2010, MNRAS accepted*

[33] **Murphy, T., et al.**,'The Australia Telescope 20GHz Survey: The Source Catalog', *2010, MNRAS, 402, 2403*

[34] **O'Neil, K.**, 'Single Dish Calibration Technique at Radio Wavelengths', *2002, ASP Conference Series, 278, 293O*

[35] **Norrod, R.D.**, 'The Receiver System - cm Regime', *2002, ASP Conference Series, 278, 91N*

[36] **Orfei, A., et al.**, 'A Multi-feed Receiver in the 18-26.5 GHz Band for Radio Astronomy', *2010, IEEE Antennas and Propagation Magazine, 52, 4*

[37] **Orfei, A.**,'PARABOLIC ANTENNAS', *2003,*
WILEY ENCYCLOPEDIA OF TELECOMMUNICATIONS - Parabolic Antennas

[38] **Orfei, A., et al.** 'Tcal management for the 18-26 GHz multi-feed receiver', *2008, GAI04 Memo Series, GAI04-TM-11.0*

[39] **Ott, M., et al.**,'An updated list of radio flux density calibrators', *1994, A&A, 284, 331*

[40] **Peng, B., et al.**,'Long-term monitoring of selected radio sources', *2000, A&AS, 145, 1*

[41] **Rohlfs K., Wilson.**, 'Tools of Radio Astronomy ', *Ed. 2, Springer-Verlag Berlin Heidelberg New York, 1996*

[42] **Reber, G.**,'Cosmic Static', *1944, Astrophy. J., 100, 279*

[43] **Ricci, R., et al.**,'First results from the Australia Telescope Compact Array 18-GHz pilot survey', *2004, MNRAS, 354, 305*

[44] **Righini, S., PhD thesis,**,
'The Enhanced Single-dish Control System and wide surveys of compact sources', *2010*, `http://urania.bo.astro.it/tesi/XXII/astrophysical_technologies/Righini_Simona.pdf`

[45] **Rudge A.W., Milne K, Olver A.D., Knight P.**, 'The Handbook of ANTENNA DESIGN Vol. 1', *London, Peter Peregrinus Ltd, 1982*

[46] **Ruze, J., et al.,**,'The effect of aperture errors on the antenna radiation pattern', *1952, Suppl. of Nuovo Cimento, 9, 364*

[47] **Satlar, C.J.**, 'Continuum 2: Specific Applications', *2002, ASP Conference Series, 278, 173S*

[52] **Taylor, A.C., et al.,**,'The radio source counts at 15 GHz and their implications for cm-wave CMB imaging', *2001, MNRAS, 327, L1-L4*

[49] **Ulich, B.L.**,'Millimeter wave radio telescopes: gain and pointing characteristics', *1981, International Journal of Infrared and Millimeter Waves, 2, 2*

[50] **Verma, R., et al.**,'A new K-band (18-26 GHz) 7-horn multi-feed receiver: Calibration campaign at Medicina 32 m dish', 2009, *Internal Report, IRA 430/09*

[51] **Verma, R., et al.**,'Pointing calibration campaign at 21 GHz with K-band multi-feed receiver ', 2011, *Internal Report, IRA 441/11*

[52] **Waldram, E.M., et al.,** ,'9C: a survey of radio sources at 15 GHz with the Ryle Telescope ', *2003, MNRAS, 342, 915*

[53] **Wallace, P.T.**,'Programming the Control Computer of the Anglo-Australian 3.9 meter Telescope', *1975, in Proceeding of the MIT Conference on Telescope Automation, Maureen K. Hugenin and Thomas B McCord (ed), p284*

Appendix A

This appendix reports the diagrams showing the offset distribution in RA, Dec and FWHM beamsize for different antenna speeds. Data are taken from the calibration campaign carried out on 2009, September 27^{th} & 28^{th} (see Chapter 4 for more details).

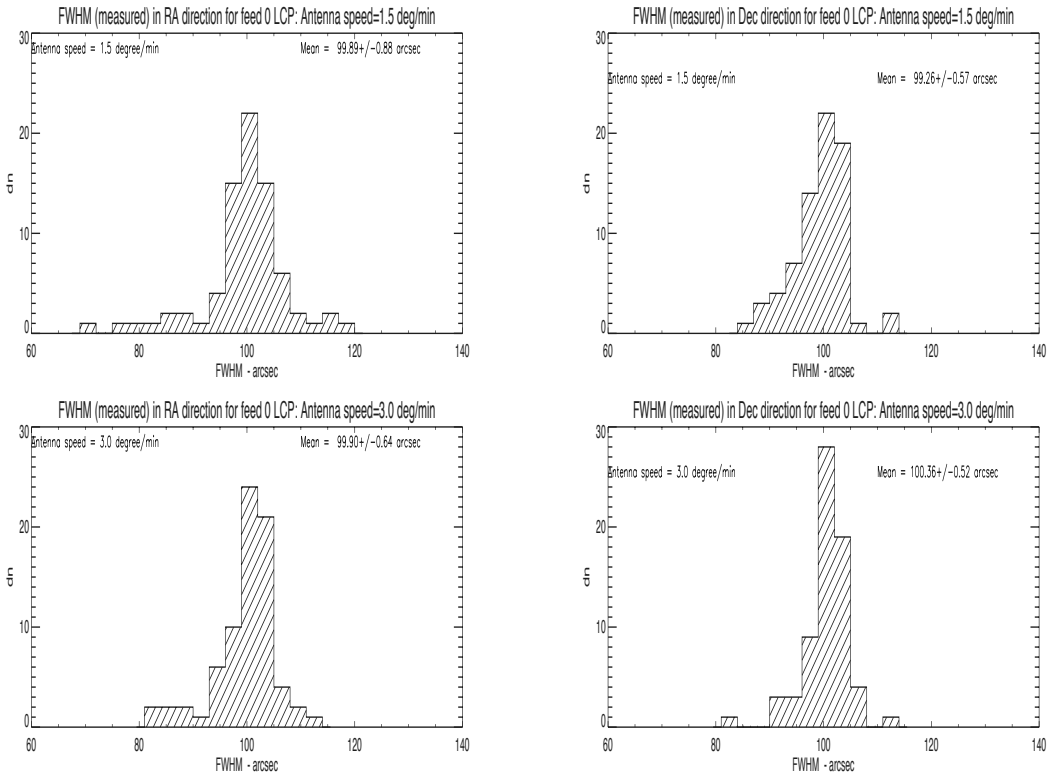

Figure 1: Histogram of the FWHM of the telescope beam (expected ≈ 100 arcsec) measured from the Gaussian fit in right ascension (left) and declination (right) directions for left circular polarization. Top: Scans performed with antenna speed of 1.5°/minute; Bottom: Scans performed with antenna speed of 3.0°/minute.

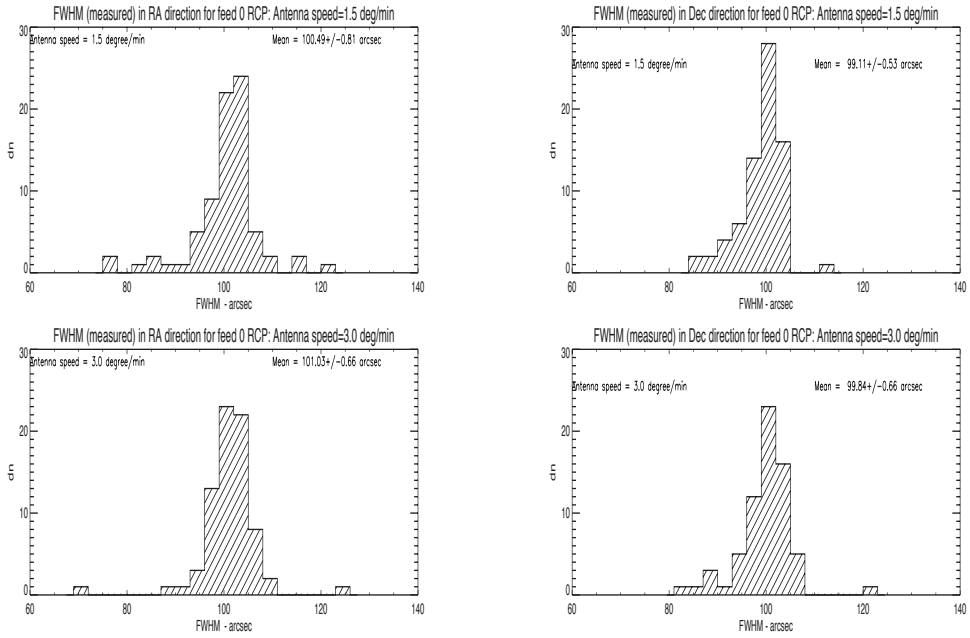

Figure 2: Histogram of the FWHM of the telescope beam (expected $\approx$ 100 arcsec) measured from the Gaussian fit in right ascension (left) and declination (right) directions for right circular polarization. Top: Scans performed with antenna speed of 1.5°/minute; Bottom: Scans performed with antenna speed of 3.0°/minute.

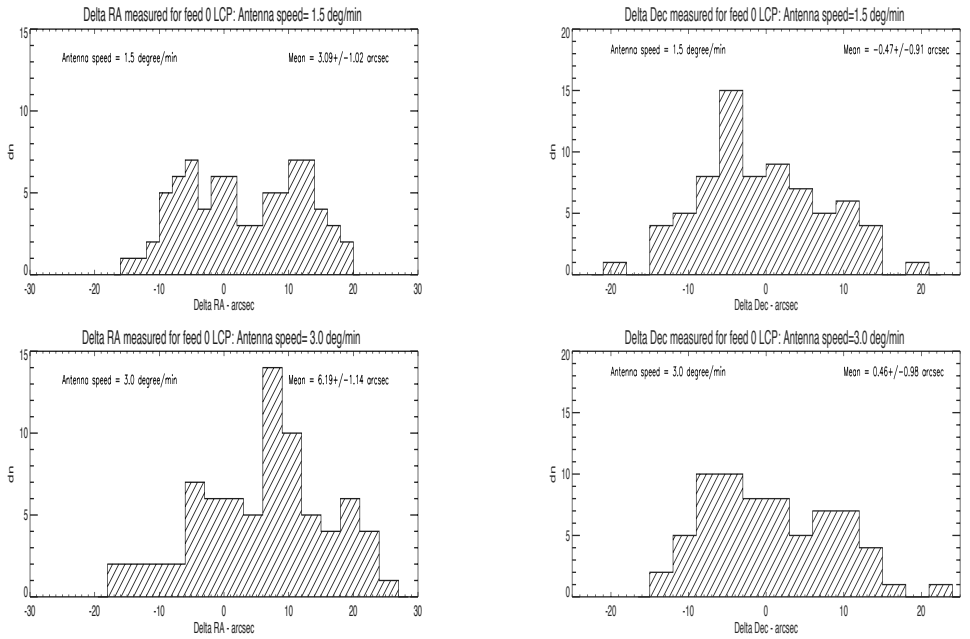

Figure 3: Histogram of the difference between source RA (left) and Dec (right) taken from the literature and the one measured from the Gaussian fit in units of arcsec for left circular polarization. Top: Scans performed with antenna speed of 1.5°/minute; Bottom: Scans performed with antenna speed of 3.0°/minute

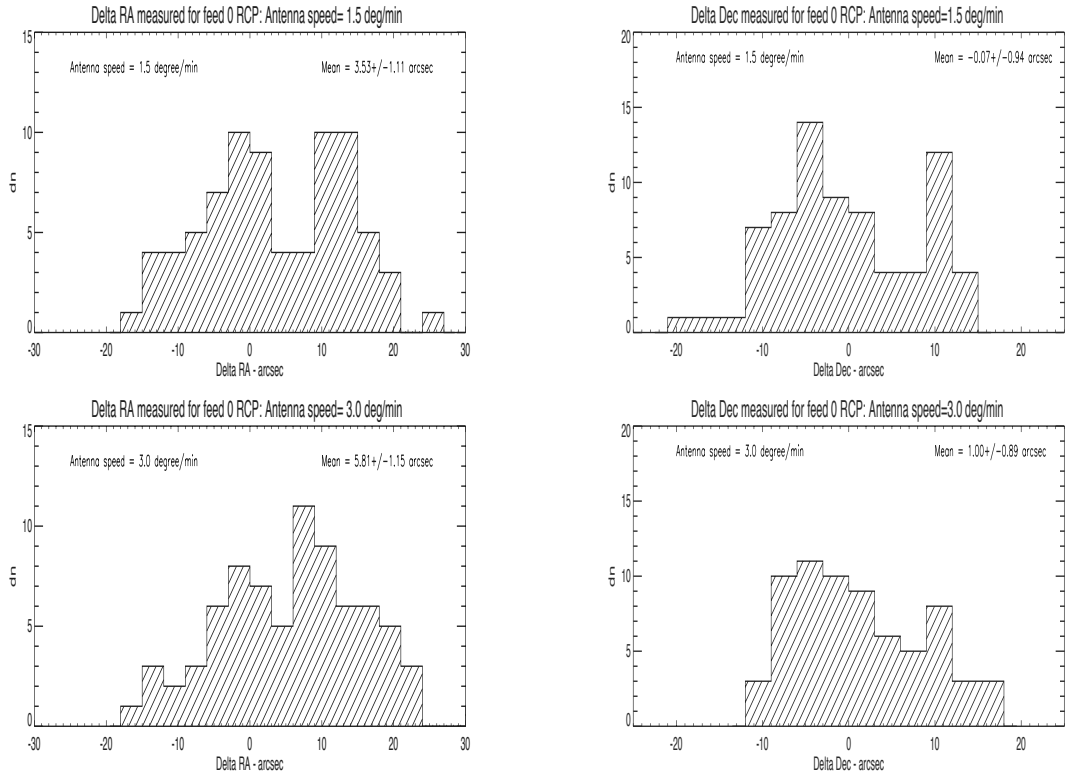

Figure 4: Histogram of the difference between source RA (left) and Dec (right) taken from the literature and the one measured from the Gaussian fit in units of arcsec for right circular polarization. Top: Scans performed with antenna speed of 1.5°/minute; Bottom: Scans performed with antenna speed of 3.0°/minute

Appendix B

In this appendix we report the diagrams showing the offset distribution in RA and Dec & FWHM beamsize for sources 3C48 and 3C286. Data are taken from the calibration campaign carried out on 2009, September 27^{th} & 28^{th} (see Chapter 4 for more details).

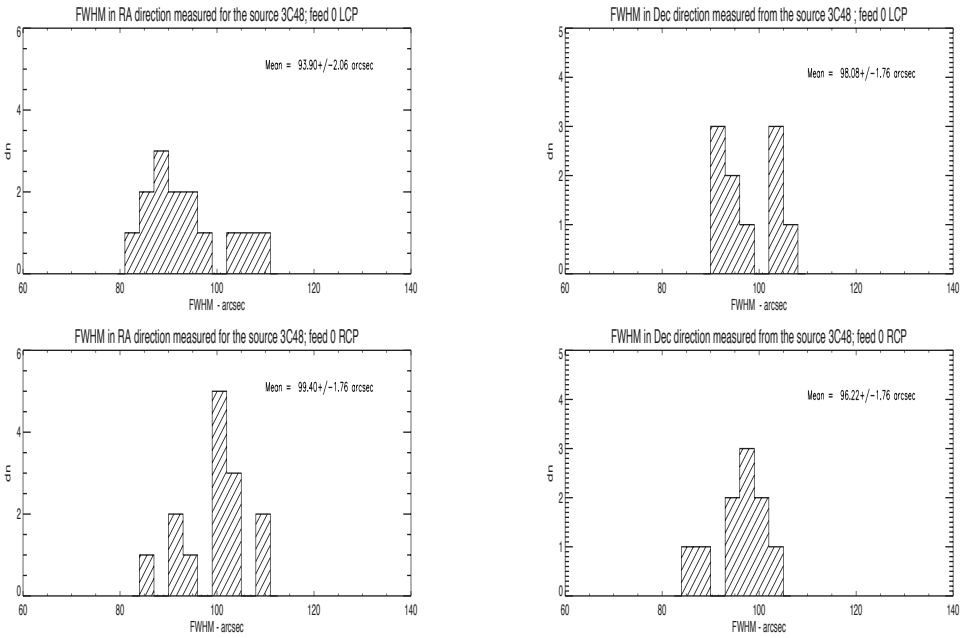

Figure 5: Source 3C48: Histogram of the FWHM of the telescope beam (expected ≈ 100 arcsec) measured from the Gaussian fit in right ascension (left) and declination (right) directions. Top: Left circular polarization; Bottom: Right circular polarization.

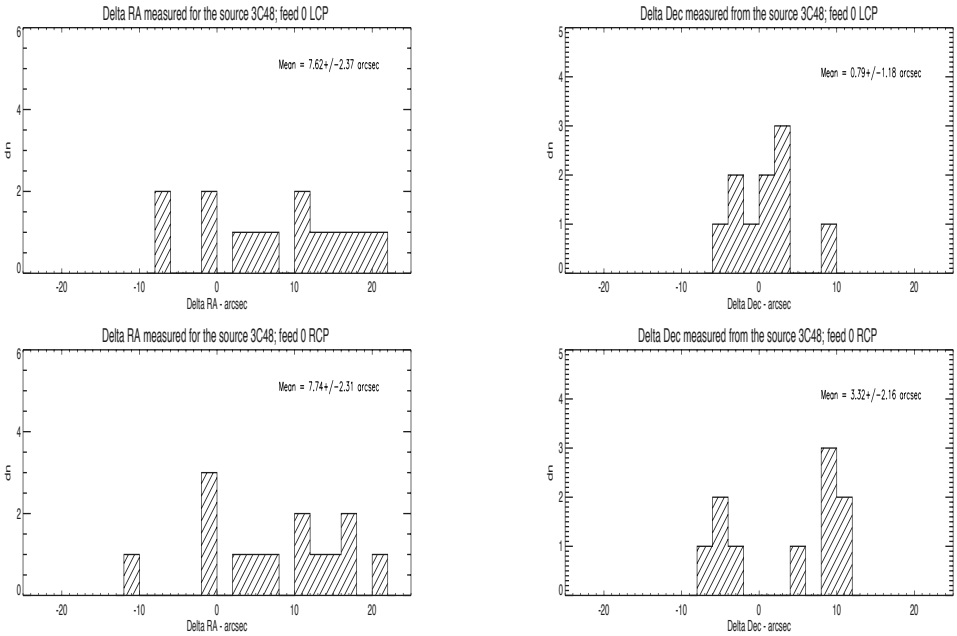

Figure 6: Source 3C48: Histogram of the difference between source RA (left) and Dec (right) taken from the literature and the one from the Gaussian fit in units of arcsec. Top: Left circular polarization; Bottom: Right circular polarization.

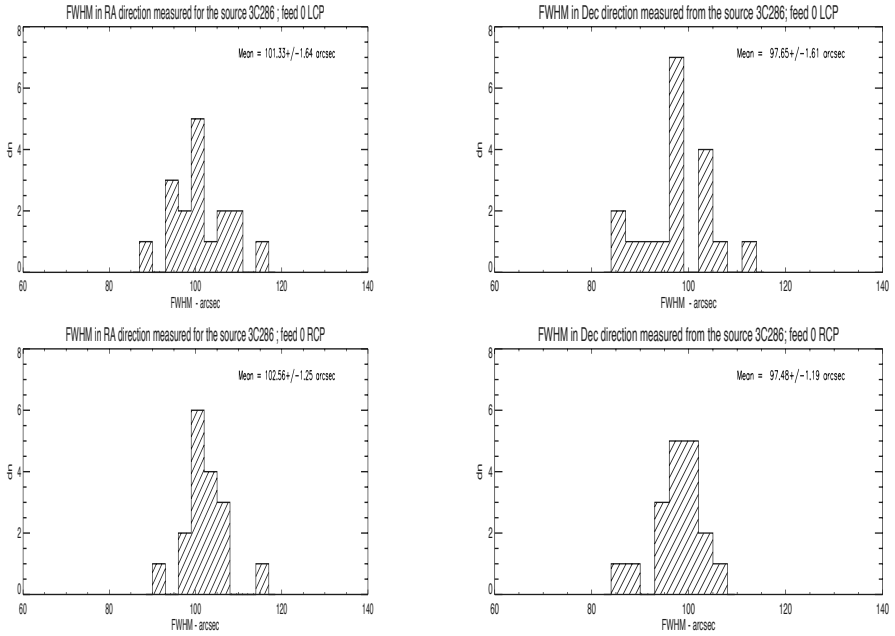

Figure 7: Source 3C286: Histogram of the FWHM of the telescope beam (expected $\approx$ 100 arcsec) measured from the Gaussian fit in right ascension (left) and declination (right) directions. Top: Left circular polarization; Bottom: Right circular polarization.

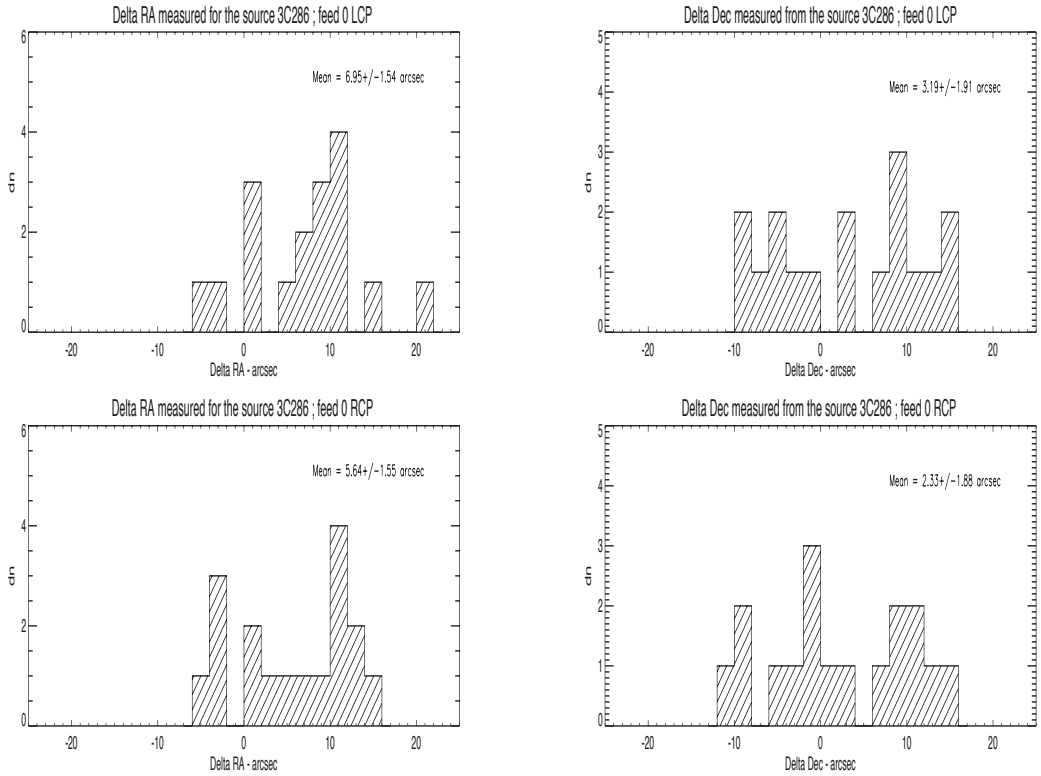

Figure 8: Source 3C286: Histogram of the difference between source RA (left) and Dec (right) taken from the literature and the one from the Gaussian fit in units of arcsec. Top: Left circular polarization; Bottom: Right circular polarization.

Appendix C

In this appendix we show the source flux density measured in units of counts as a function of elevation for each of the observed sources. Data are taken from the calibration campaign carried out on 2009, September 27^{th} & 28^{th} (for more details see Chapter 4).

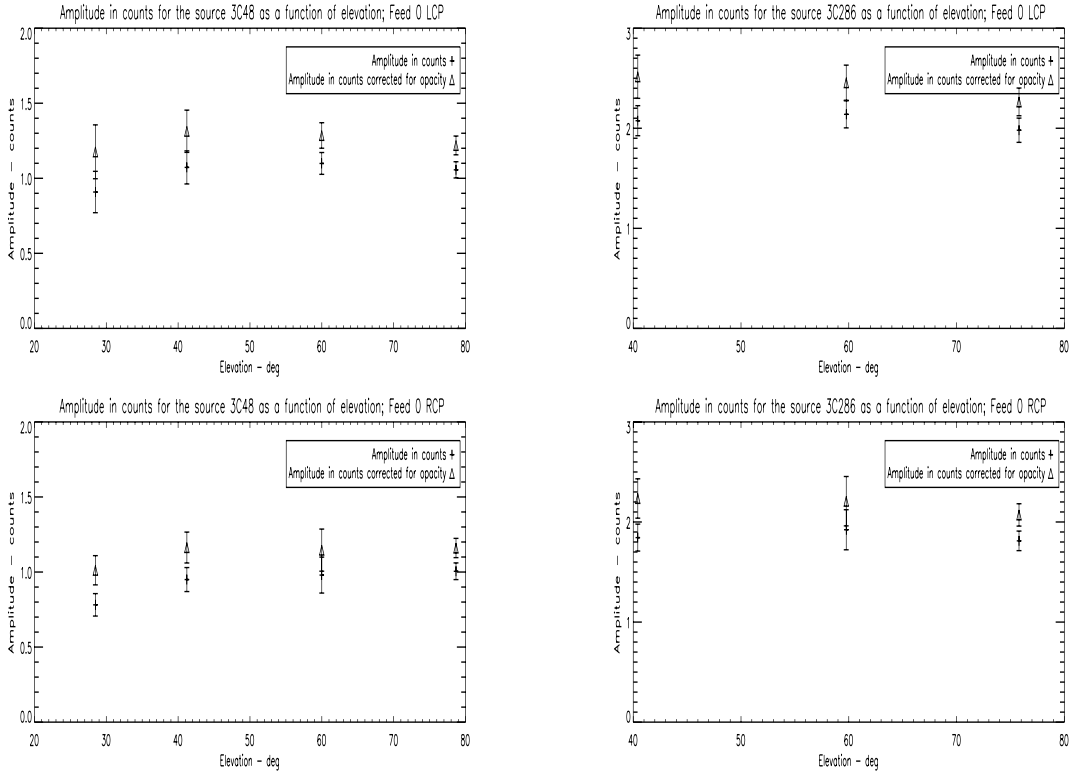

Figure 9: The flux density of source 3C48 (left) and 3C286 (right) in units of counts as a function of elevation. Symbols + and Δ represent the raw flux density and the flux density corrected for opacity respectively. Top: Left circular polarization; Bottom: Right circular polarization.

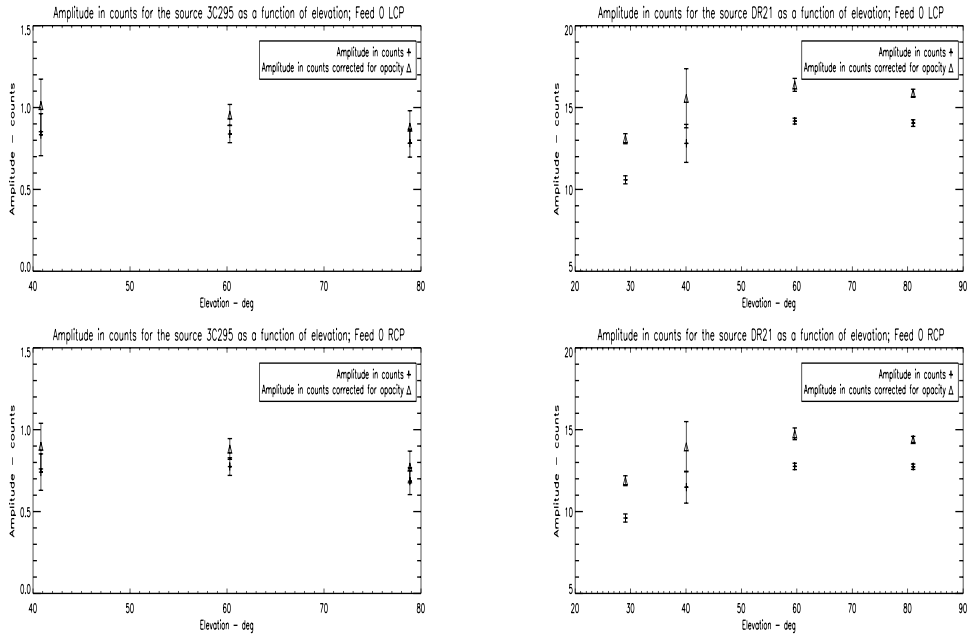

Figure 10: The flux density of source 3C295 (left) and DR21(right) in units of counts as a function of elevation. Symbols + and Δ represent the raw flux density and the flux density corrected for opacity respectively. Top: Left circular polarization; Bottom: Right circular polarization.

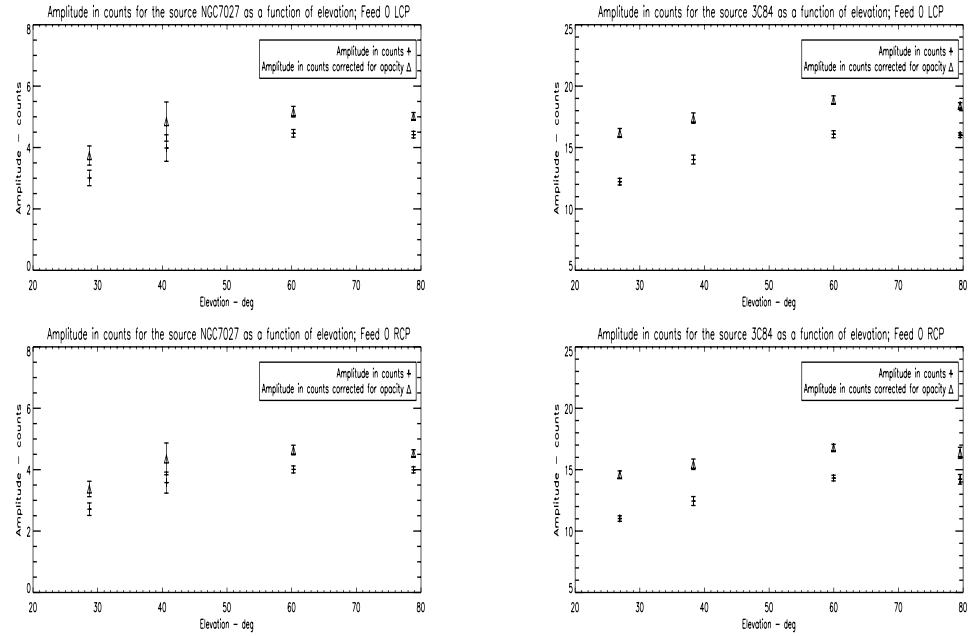

Figure 11: The flux density of source NGC7027 (left) and 3C84 (right) in units of counts as a function of elevation. Symbols + and Δ represent the raw flux density and the flux density corrected for opacity respectively. Top: Left circular polarization; Bottom: Right circular polarization.

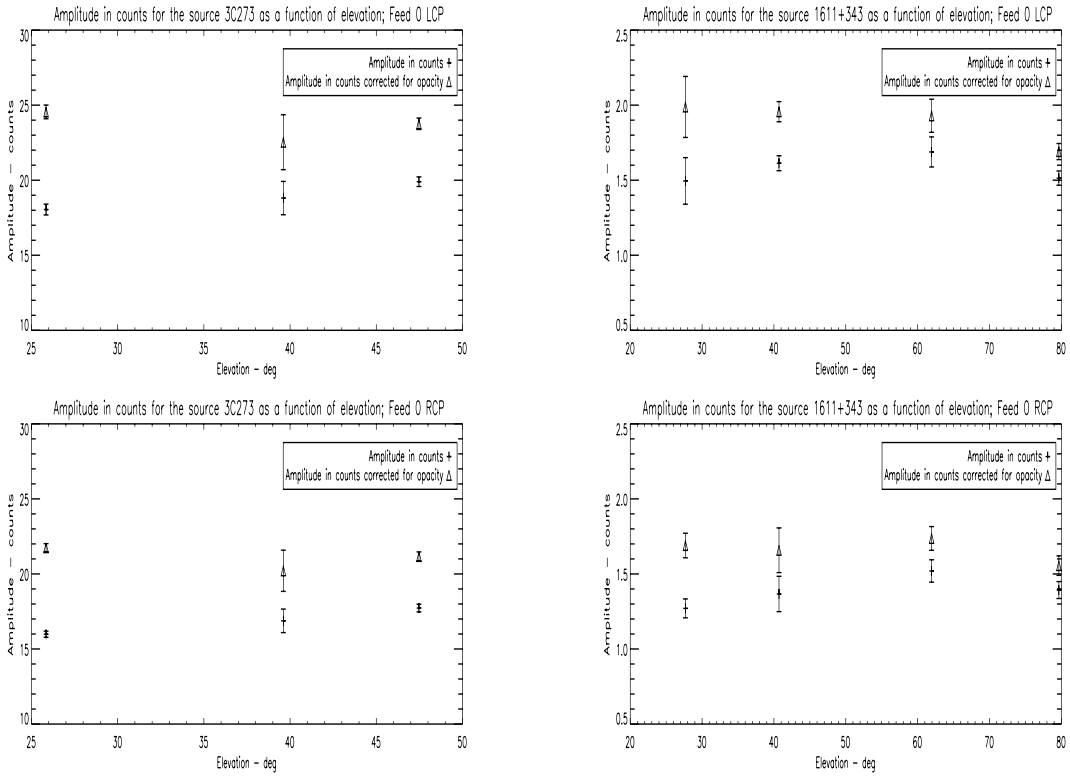

Figure 12: The flux density of source 3C273 (left) and 1611+343 (right) in units of counts as a function of elevation. Symbols + and Δ represent the raw flux density and the flux density corrected for opacity respectively. Top: Left circular polarization; Bottom: Right circular polarization.

Appendix D

In this appendix we report the count to Jansky factor as a function of elevation for each source. Data are taken from the calibration campaign carried out on 2009, September 27^{th} & 28^{th} (for more details see Chapter 4).

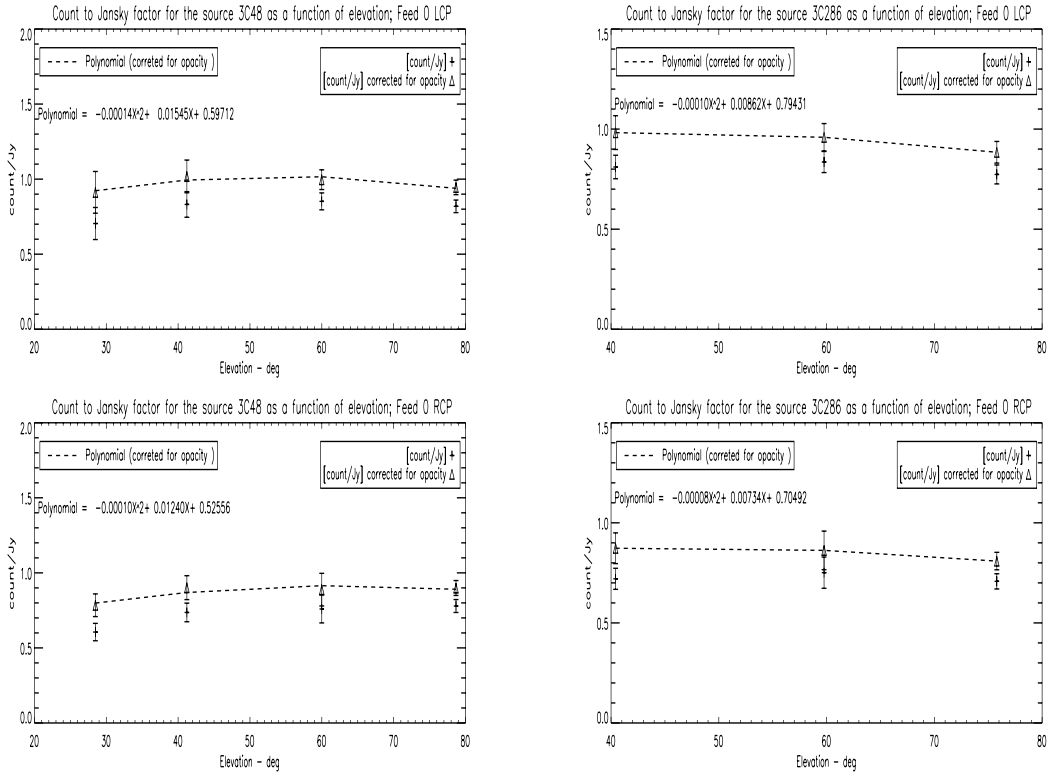

Figure 13: The count to Jansky factor obtained for source 3C48 (left) and 3C286 (right) as a function of elevation. Symbols + and Δ represent the count to Jansky factor before and after correcting for opacity respectively. The dotted lines correspond to the polynomial obtained after correcting for atmospheric absorption. Top: Left circular polarization; Bottom: Right circular polarization.

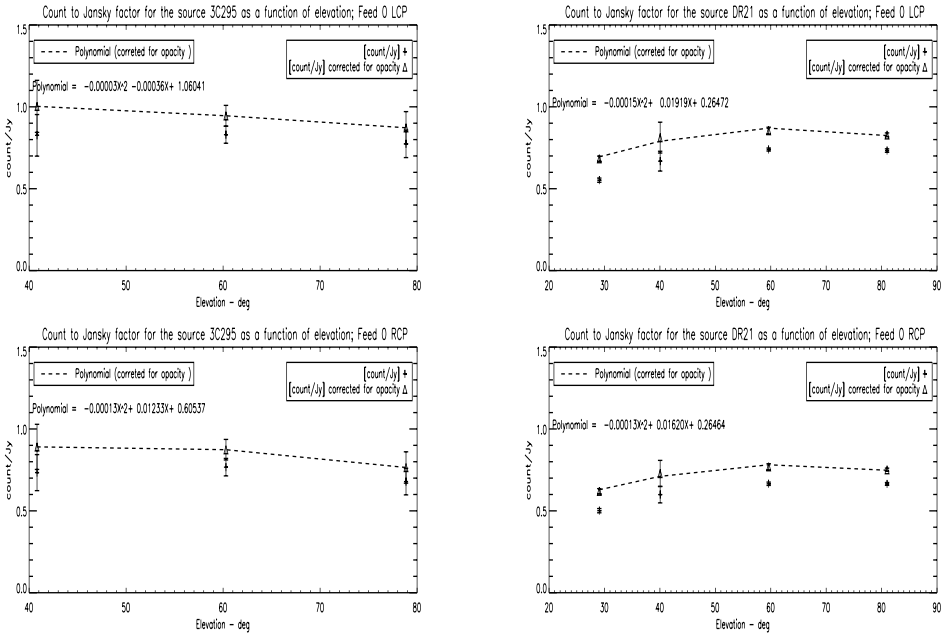

Figure 14: The count to Jansky factor obtained for source 3C295 (left) and DR21 (right) as a function of elevation. Symbols + and Δ represent the count to Jansky factor before and after correcting for opacity respectively. The dotted lines correspond to the polynomial obtained after correcting for atmospheric absorption. Top: Left circular polarization; Bottom: Right circular polarization.

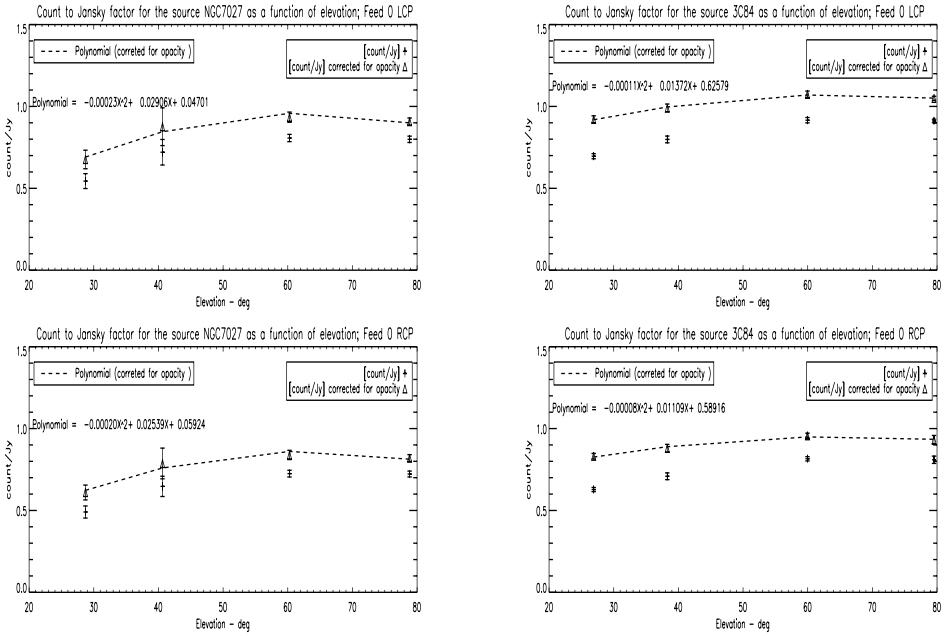

Figure 15: The count to Jansky factor obtained for source NGC7027 (left) and 3C84 (right) as a function of elevation. Symbols + and Δ represent the count to Jansky factor before and after correcting for opacity respectively. The dotted lines correspond to the polynomial obtained after correcting for atmospheric absorption. Top: Left circular polarization; Bottom: Right circular polarization.

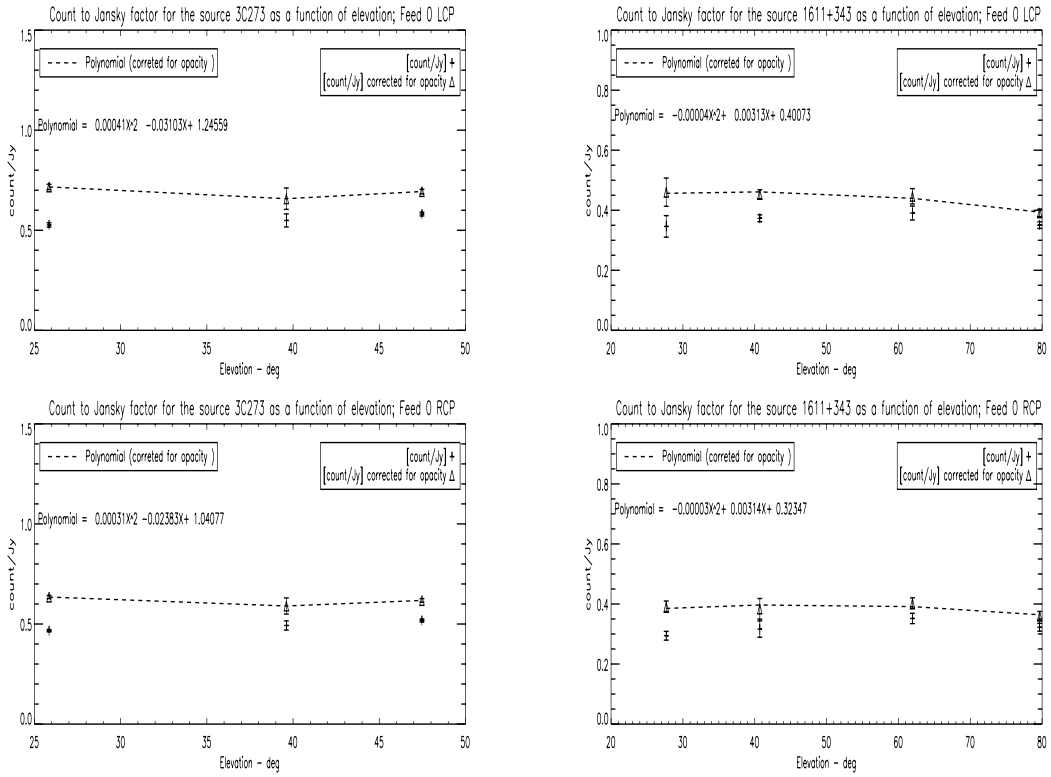

Figure 16: The count to Jansky factor obtained for source NGC7027 (left) and 3C84 (right) as a function of elevation. Symbols + and Δ represent the count to Jansky factor before and after correcting for opacity respectively. The dotted lines correspond to the polynomial obtained after correcting for atmospheric absorption. Top: Left circular polarization; Bottom: Right circular polarization.

Appendix E

This appendix reports the diagrams showing the offset distribution in RA, Dec and FWHM beamsize for sources 3C48, 3C286 and 3C147. Data are taken from the pilot survey conducted in winter 2010. (see Chapter 5 for more details).

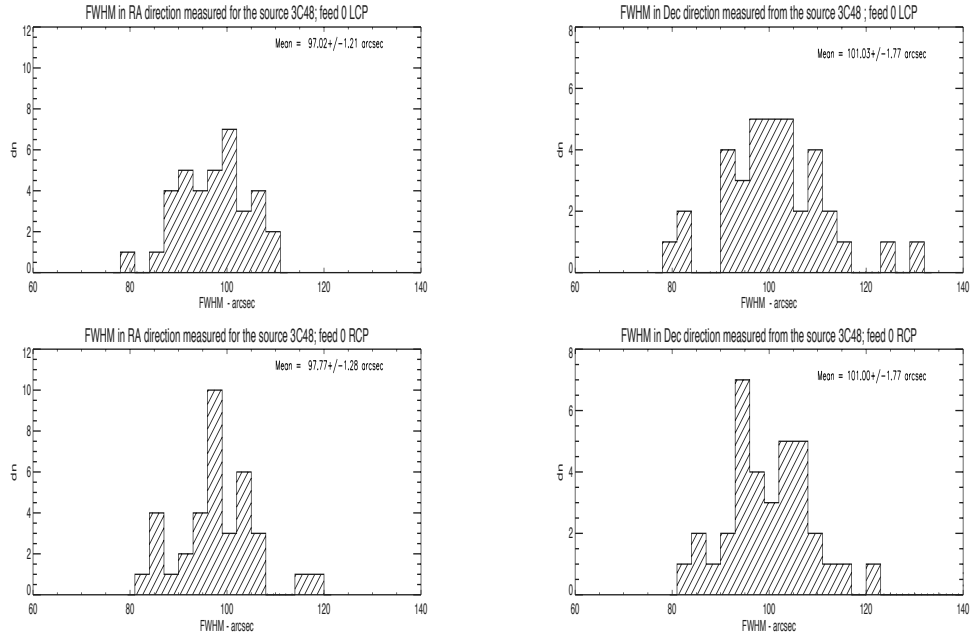

Figure 17: Source 3C48: Histogram of the FWHM of the telescope beam (expected ≈ 100 arcsec) measured from the Gaussian fit in right ascension (left) and declination (right) directions. Top: Left circular polarization; Bottom: Right circular polarization.

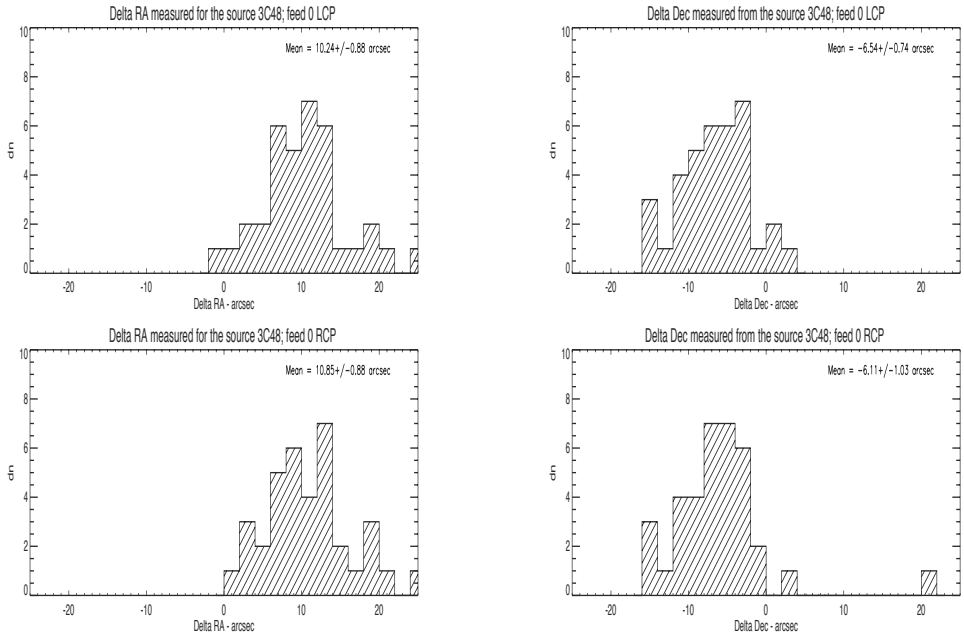

Figure 18: Source 3C48: Histogram of the difference between source RA (left) and Dec (right) taken from the literature and the one from the Gaussian fit in units of arcsec. Top: Left circular polarization; Bottom: Right circular polarization.

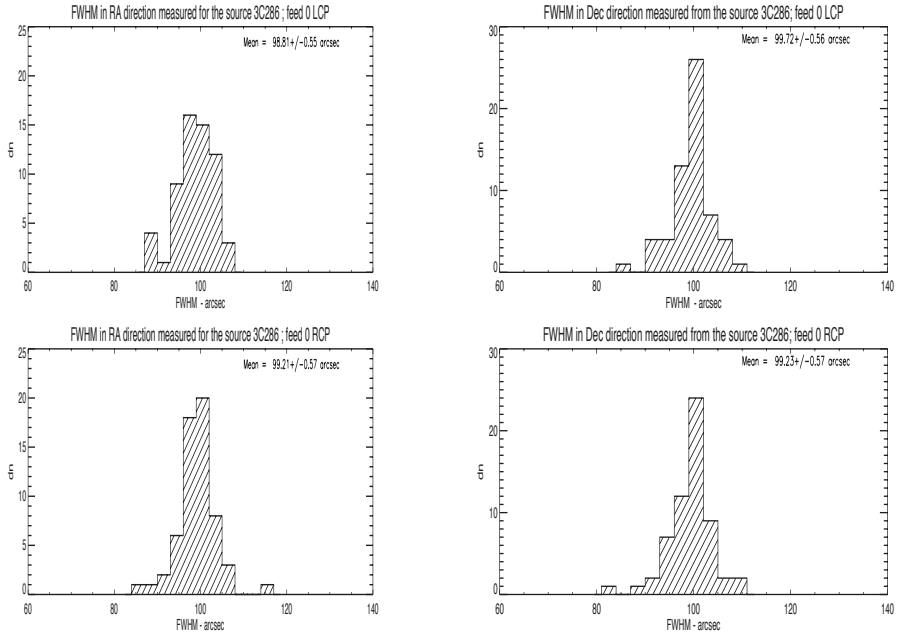

Figure 19: Source 3C286: Histogram of the FWHM of the telescope beam (expected $\approx$ 100 arcsec) measured from the Gaussian fit in right ascension (left) and declination (right) directions. Top: Left circular polarization; Bottom: Right circular polarization.

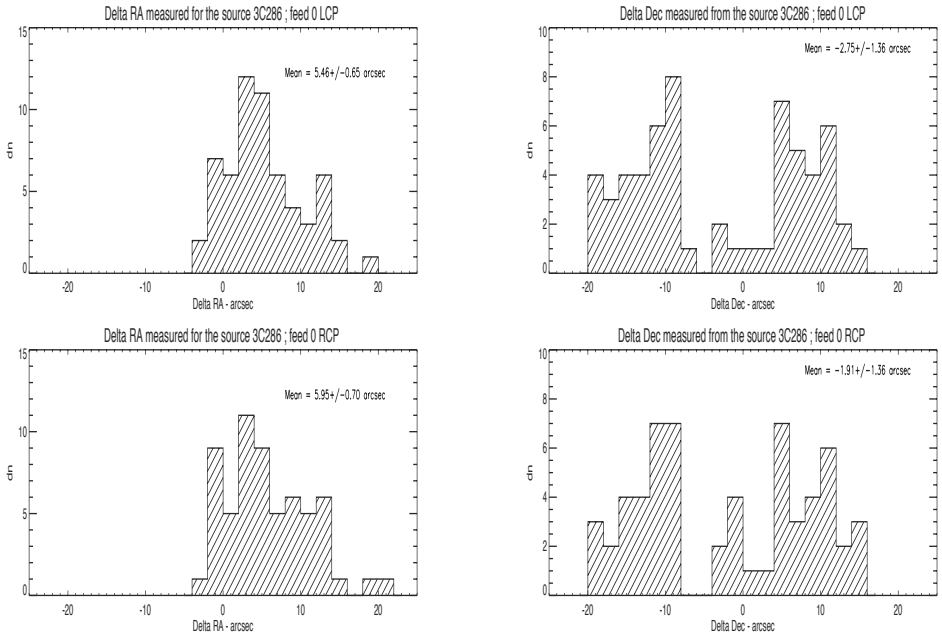

Figure 20: Source 3C286: Histogram of the difference between source RA (left) and Dec (right) taken from the literature and the one from the Gaussian fit in units of arcsec. Top: Left circular polarization; Bottom: Right circular polarization.

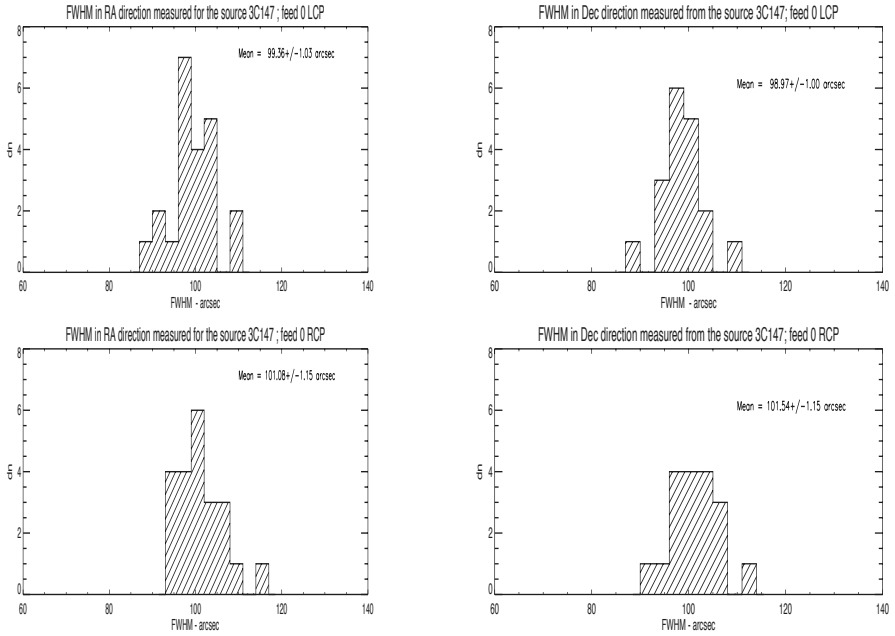

Figure 21: Source 3C147: Histogram of the FWHM of the telescope beam (expected $\approx$ 100 arcsec) measured from the Gaussian fit in right ascension (left) and declination (right) directions. Top: Left circular polarization; Bottom: Right circular polarization.

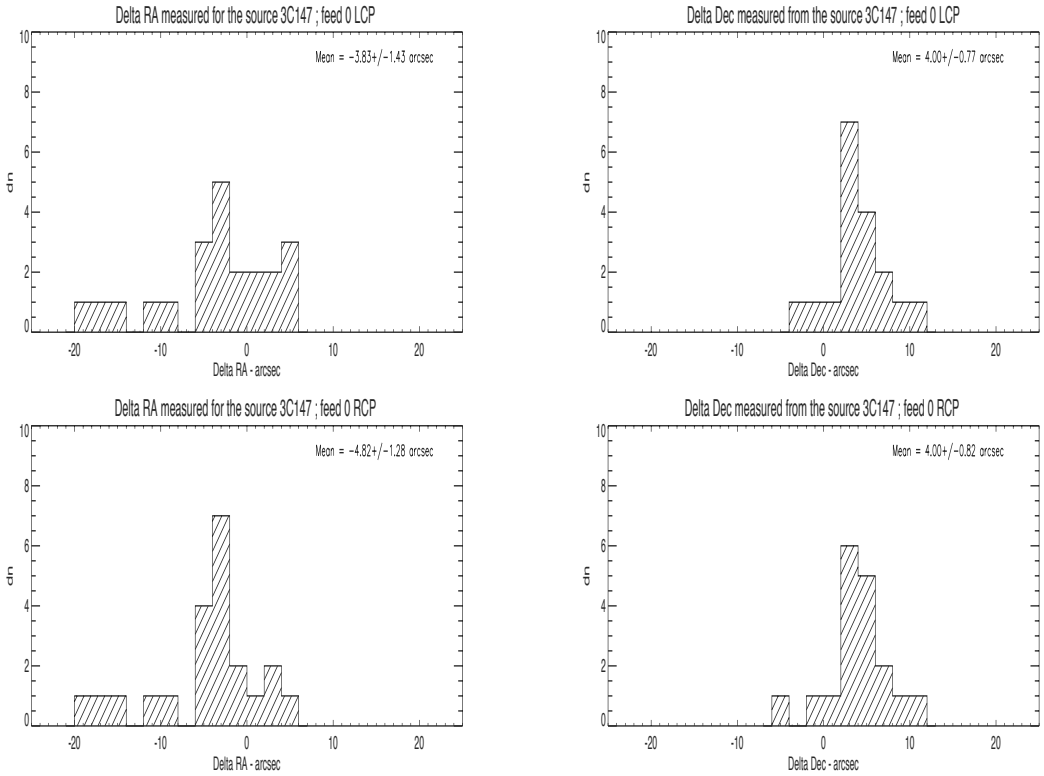

Figure 22: Source 3C147: Histogram of the difference between source RA (left) and Dec (right) taken from the literature and the one from the Gaussian fit in units of arcsec. Top: Left circular polarization; Bottom: Right circular polarization.